

**Centro de Investigación Científica y de Educación
Superior de Ensenada, Baja California**



**Doctorado en Ciencias
en Óptica con orientación en Óptica Física**

**Generation and recombination of time-frequency
entangled photon pairs**

Tesis

para cubrir parcialmente los requisitos necesarios para obtener el grado de
Doctor en Ciencias

Presenta:

Guillermo Daniel Jiménez Gómez

Ensenada, Baja California, México

2019

Tesis defendida por

Guillermo Daniel Jiménez Gómez

y aprobada por el siguiente Comité

Dr. Kevin Arthur O'Donnell

Director de tesis

Dr. Alexander V. Sergienko

Dr. Jan Peřina Jr.

Dr. Eugenio Rafael Méndez Méndez

Dra. Veneranda Guadalupe Garcés Chávez



Dr. Israel Rocha Mendoza

Coordinador del Posgrado en Óptica

Dra. Rufina Hernández Martínez

Directora de Estudios de Posgrado

Guillermo Daniel Jiménez Gómez © 2019

Queda prohibida la reproducción parcial o total de esta obra sin el permiso formal y explícito del autor y director de la tesis

Resumen de la tesis que presenta Guillermo Daniel Jiménez Gómez como requisito parcial para la obtención del grado de Doctor en Ciencias en Óptica con orientación en Óptica Física.

Generación y recombinación de parejas de fotones entrelazados en tiempo-frecuencia

Resumen aprobado por:

Dr. Kevin Arthur O'Donnell
Director de tesis

Se presenta un estudio teórico y experimental de los procesos de generación y recombinación de parejas de fotones en cristales no-lineales de segundo orden. El estado de dos fotones y el estado recombinado son derivados a partir de un operador Hamiltoniano de interacción en el régimen espontáneo considerando todos los grados de libertad relevantes. Se derivan soluciones rigurosas cuantitativas en el régimen espontáneo para la tasa de detección de parejas coincidentes, la tasa de detección de fotones individuales, la potencia del campo de parejas, y la tasa de recombinación, todas con espectros angulares y de frecuencias arbitrarios para el haz de bombeo y considera también dominios de detección arbitrarios, todas las cuales se presentan en escala absoluta. También se muestra un estudio experimental de las parejas de fotones producidos en cristales de KTP con inversiones periódicas de dominios, donde se utiliza la detección coincidente para medir la emisión de los pares degenerados y no-degenerados en una variedad de configuraciones. La dependencia de la tasa de pares coincidentes en función de uno de los ángulos de detección y la temperatura del cristal fue caracterizada utilizando bombeo de una y dos frecuencias utilizando filtros de banda angosta así como detección de gran ancho de banda espectral. Los resultados teóricos para la detección parejas son evaluados bajo condiciones realistas que representan nuestras condiciones experimentales de manera precisa y son comparadas con nuestras observaciones. Se presentan cálculos para la recombinación de parejas para un caso idealizado y para dos casos realistas los cuales son comparados con resultados experimentales publicados anteriormente.

Palabras clave: SPDC, recombinación de parejas de fotones

Abstract of the thesis presented by Guillermo Daniel Jiménez Gómez as a partial requirement to obtain the Doctor of Science degree in Optics with orientation in Physical Optics.

Generation and recombination of time-frequency entangled photon pairs

Abstract approved by:

Dr. Kevin Arthur O'Donnell
Thesis Director

A theoretical and experimental study of the processes of photon pair generation and recombination in second-order nonlinear crystals is presented. The two-photon and upconverted states produced in, respectively, downconversion and recombination are derived from an interaction Hamiltonian formulation in the spontaneous regime, accounting for all of the relevant degrees of freedom. Rigorous solutions are derived within the spontaneous regime for the rate of coincident pair detection, the rate of single photon detection, the downconverted power, and the recombination rate pump fields with arbitrary frequency and angular spectra, all of which are provided on absolute scales. An experimental study of the photon pairs produced using periodically-poled KTP crystals is also shown, where coincidence detection is used to measure the degenerate and non-degenerate emission in a wide variety of configurations. The angular and temperature dependence of the coincidences is characterized using single and two-frequency pumps, with narrowband and broadband detection. The theoretical results for pair detection are evaluated under realistic conditions that accurately represent our experimental conditions and compared with our observations. Calculations for photon pair recombination are shown for an idealized case as well as two realistic cases which are compared with previously published experiments.

Keywords: SPDC, photon-pair recombination

Dedicatory

To those who are willing to pay the price.

Agradecimientos

Agradezco a mi esposa Anaís Mancera, a mis padres Martha Gómez y Luis Jiménez, a mi director de tesis Dr. Kevin O'Donnell y a los integrantes de mi comité de tesis: Dr. Eugenio Méndez por enseñarme la óptica física, Dra. Veneranda Garces por la dirección, Dr. Jan Peřina Jr. por el tiempo dedicado, Dr. Alexander Sergienko por la inspiración y los comentarios.

También agradezco a mis profesores Dr. Jorge Mata, Dr. Jesús Maytorena, Dr. Hector Escamilla, Dr. Pedro Negrete, Dr. Alvaro Alvarez Padilla, Dr. Hector Aceves, Dr. Roberto Romo, Dr. Jorge Villavicencio, Dr. Roberto Vázquez, Dr. Ramon Carrillo, Dr. Roger Cudney, Dra. Catalina López, y Mtra. Gloria Rubi Vazquez. Agradezco especialmente a Israel Ruiz Santana y Andrés Carrasco Avendaño del taller de mecánica fina.

Agradezco al Centro de Investigación Científica y Educiación Superior de Ensenada (CICESE) por el apoyo recibido a lo largo de cerca de 10 años y al (CONACyT) por la beca nacional, sin la cual no me hubiera sido posible realizar mis estudios doctorales. No de becario: 275149.

Table of contents

	Page
Abstract in spanish	ii
Abstract in english	iii
Dedicatory	iv
Acknowledgments	v
List of figures	viii
List of tables	xii
1 Introduction	
2 Theory of entangled photon pair generation	
2.1 Quantum representation of the pump	5
2.1.1 Frequency and angular amplitude spectrum of the pump	6
2.2 The interaction Hamiltonian and electric field operators	7
2.3 Temporal evolution and spatial integrations	9
2.3.1 The longitudinal Quasi Phase-Matching function	10
2.4 The quantum state of down-converted light and the two-photon amplitude	11
2.5 Calculation of the rates	12
2.5.1 Photon pair rates	12
2.5.2 Gaussian beam and the focused beam correction	14
2.5.3 Narrowband and wide-beam limits	15
2.5.4 Singles rate and down-converted power	17
2.6 Vacuum amplitude and state normalization	18
3 Theory of time-frequency entangled photon pair recombination	
3.1 The role of dispersion in photon pair recombination	22
3.2 The incident two-photon state	23
3.3 Temporal evolution and commutation relations	24
3.4 Quantum state of up-converted light	25
3.5 Coherence functions and the up-converted photon rate	28
3.5.1 Self-coherence function, up-converted photon rate, and the normalized coherence function	28
3.5.2 Mutual coherence of the pump and up-converted light	29
3.5.3 Single-frequency pump limit	31
3.5.4 Wide-beam pump limit	33
3.5.5 Time-delayed up-converted rate	34
4 Measurements and calculations of the entangled photon pairs generated in periodically-poled KTP crystals	
4.1 Experimental arrangements	37

Table of contents (continued)

4.1.1	Pump laser systems	37
4.1.2	Frequency stability monitoring system	38
4.1.3	PPKTP crystals and temperature control	39
4.1.4	Pair collection optical system	40
4.1.5	Coincidence discrimination, real-time monitoring, and automated data collection	42
4.2	Crystal temperature dependence of the pair rate	43
4.2.1	Detection geometry and integration domain effects: Degenerate SPDC	44
4.2.2	Tuning curves and correction terms	46
4.2.3	Temperature dependence using two-frequency pump	50
4.2.4	Non-degenerate SPDC	53
4.3	Angular dependence of the pair rate	55
4.3.1	Narrowband detection	55
4.3.2	Effects of the longitudinal QPM function in the angular dependence of the degenerate photon pair emission	56
4.3.3	Observations of the angular dependence of the pair rate with a two-frequency pump	61
4.3.4	Broadband detection	64
5	Calculations of the recombination of the entangled photon pairs	
5.1	Ideal optical systems	69
5.1.1	Linear transfer functions	69
5.1.2	Delayed recombination	71
5.1.3	Recombination rate dependence on temperature and pump wavelength	72
5.2	Realistic optical systems	73
5.2.1	Linear transfer functions	74
5.2.2	Delayed recombination: comparison with experiments	77
6	Conclusions	
	Bibliography	86
	Appendix: Invariance of the down-converted rates under exchange of the signal and idler variables	90

List of figures

Figure	Page
1 Dispersion-compensated imaging system (CIS) with unit magnification that couples the infrared photon pairs produced in the non-linear crystal NLC1 into an identically-prepared crystal NLC2.	23
2 Experimental diagram.	37
3 Measured rate of pair detection R_π as a function of crystal temperature T with central observation angles $\theta_s = \theta_i = 2.16^\circ$ using a crystal of type A. . .	44
4 Calculated rate of pair detection R_π as a function of crystal temperature T with central observation angles $\theta_s = \theta_i = 2.16^\circ$	45
5 Tuning curve and experimental data for the crystal temperature T as a function of signal wavelength λ_s for the external observation angles $\theta'_s = 2.16^\circ\text{C}$ and $\theta'_s = 2.74^\circ\text{C}$	46
6 Tuning curve and experimental data for the external signal angle θ'_s as a function of crystal temperature T for degenerate emission with $\lambda_s = \lambda_i = 812\text{ nm}$, and the non-degenerate emission with $\lambda_s = 722\text{ nm}$ and $\lambda_i = 927\text{ nm}$ for crystals of type A.	47
7 Measured rate of pair detection R_π as a function of crystal temperature T for $\theta_s = \theta_i = 2.165^\circ$ and filter pair A using a crystal of type B with signal and idler detection angles of $\Delta\theta = 0.086^\circ$	49
8 Measured reduced longitudinal quasi-phase mismatch $\Delta k_z L/2$ as a function of crystal temperature T for frequency degenerate down-conversion, $\omega_s = \omega_i = \omega_p/2$, with the detection geometry $\theta_s = \theta_i = 2.165^\circ$. A quadratic fit to the data is also shown, along with the curves calculated using our correction term \hat{k} (Jimenez <i>et al.</i> , 2017) and theory calculated using no correction	50
9 (a) Measured rate of pair detection R_π and (b) rates of single photon detection for the signal and idler detectors, as a function of crystal temperature T for $\theta_s = \theta_i = 2.16^\circ$ and filter pair A with a two-frequency pump spectrum with a line separation of approximately 0.082 nm and $\Delta\theta = 0.086^\circ$ detection apertures.	51
10 Measured rate of pair detection R_π as a function of crystal temperature T for $\theta_s = \theta_i = 2.165^\circ$ and filter pair A. Results are shown for a single frequency pump at 406.118 nm, for pump lines at 406.09 and 406.16 nm, and for pump lines at 406.07 and 406.16 nm.	52
11 Measured rate of pair detection R_π as a function of crystal temperature T for a crystal of type A with (a) $\theta_s = 2.32^\circ$ using filter pair B with $\Delta\theta = 0.086^\circ$ detection apertures and (b) $\theta_s = 2.76^\circ$ using filter pair C with $\Delta\theta = 0.15^\circ$ detection apertures.	53

List of figures (continued)

Figure	Page	
12	Normalized rate of pair detection R_π as a function of crystal temperature T as calculated for (b) $\theta_s = 2.32^\circ$ using the pair detection bandwidth of filter pair B and detection apertures of $\Delta\theta = 0.086^\circ$ and (c) $\theta_s = 2.76^\circ$ using the pair detection bandwidth of filter pair C and detection apertures of $\Delta\theta = 0.086^\circ$	54
13	Measured rate of pair detection R_π as a function of the signal central detection angle θ_s using a crystal of type A (a) filter pair A at $T = 53.2^\circ\text{C}$ with $\Delta\theta = 0.086^\circ$ detection angles, (b) filter pair B at $T = 56.0^\circ\text{C}$ with $\Delta\theta = 0.086^\circ$ detection angles, and (c) filter pair C at $T = 97^\circ\text{C}$ with $\Delta\theta = 0.15^\circ$ detection angles.	57
14	Measured rate of pair detection R_π as a function of the signal central detection angle ϕ_s using a crystal of type A with (a) filter pair A at $T = 53.2^\circ\text{C}$ with $\Delta\theta = 0.086^\circ$ detection angles, (b) filter pair B at $T = 56.0^\circ\text{C}$ with $\Delta\theta = 0.086^\circ$ detection angles, and (c) filter pair C at $T = 97^\circ\text{C}$ with $\Delta\theta = 0.15^\circ$ detection angles.	57
15	Calculated pair rate R_π as a function of the signal central detection angle θ_s using observation angles of $\Delta\theta_s = 0.086^\circ$ with the pair detection bandwidth of filter pairs (a) A at $T = 53.0^\circ\text{C}$, (b) B at $T = 56.2^\circ\text{C}$, and (c) C at $T = 97.0^\circ\text{C}$	58
16	Calculated pair rate R_π as a function of the signal central detection angle ϕ_s using observation angles of $\Delta\theta_s = 0.086^\circ$ with the pair detection bandwidth of filter pairs (a) A at $T = 53.0^\circ\text{C}$, (b) B at $T = 56.2^\circ\text{C}$, and (c) C at $T = 97.0^\circ\text{C}$	58
17	Measured rate of pair detection R_π as a function of the signal central detection angle θ_s using a crystal of type B at $T = 132.2^\circ\text{C}$ with $\Delta\theta = 0.086^\circ$ detection angles using laser system LS1.	60
18	Measured rate of pair detection R_π and rate of signal photon detection R_s as a function of the signal central detection angle θ_s using a crystal of type B at $T = 134.7^\circ\text{C}$ with $\Delta\theta = 0.086^\circ$ detection angles using laser system LS1.	60
19	Calculation of the pair rate R_π with conditions comparable to Fig. 18. The value of the normalized longitudinal QPM is shown along with reference horizontal line . The idler detector is located at $\theta_i = 2.165^\circ$, and $T = 133.5^\circ\text{C}$	61
20	Measured rate of pair detection R_π as a function of the signal detection angle θ_s with two simultaneous pump lines at 406.09 and 406.30 nm, with $\theta_i = 2.16^\circ$ and detector aperture diameters $\Delta\theta_s = 0.086^\circ$ and $\Delta\theta_i = 0.57^\circ$	62

List of figures (continued)

Figure	Page
21 Calculation of the pair rate R_π as a function of the signal detection angle θ_s with conditions as in Fig. 20 for (a) $T = 53.0^\circ\text{C}$ and (b) $T = 55.0^\circ\text{C}$	63
22 Measured pair rate R_π as a function of the signal detection angle θ_s with crystal temperatures T of (a) 53.0°C , (b) 58.0°C , and (c) 63.0°C with signal and idler integration angles of $\Delta\theta = 0.086^\circ$	64
23 Calculation of the pair rate R_π as a function of the signal detection angle θ_s for detection conditions as in Fig. 22 at (a) $T = 53.0^\circ\text{C}$ and (b) $T = 55.0^\circ\text{C}$	66
24 Normalized angular transfer function as a function of external angle θ_p for idealized photon pair recombination assuming 5mm lithium niobate crystals and an external cutoff angle $\tilde{\theta}_c$ of 1.5° , 2.3° , and 4.0°	69
25 Normalized point-spread functions $h(r)$ as a function of radial coordinate, obtained from Fourier-Bessel transform of the results of Fig. 24.	70
26 Normalized recombination rate as a function of time delay τ in the ideal case assuming 5 mm long lithium niobate crystals and an external cutoff angle $\tilde{\theta}_c$ of 1.5° , 2.3° , and 4.0°	71
27 Normalized recombination rate as a function of the temperature of the down-conversion and up-conversion crystals T in the ideal case assuming 5 mm long lithium niobate crystals and an external cutoff angle $\tilde{\theta}_c$ of 1.5° , 2.3° , and 4.0°	72
28 Normalized recombination rate as a function of the pump wavelength λ_p in the ideal case assuming 5 mm long lithium niobate crystals and an external cutoff angle $\tilde{\theta}_c$ of 1.5° , 2.3° , and 4.0°	73
29 Real and imaginary parts of the angular transfer function calculated assuming 5 mm lithium niobate crystals with realistic dispersion parameters and an external cutoff angle $\tilde{\theta}_c$ of 1.5° , and 2.3°	75
30 Real part, imaginary part and modulus of the angular transfer function calculated assuming 5 mm lithium niobate crystals with realistic dispersion parameters and an external cutoff angle $\tilde{\theta}_c$ of 4.0°	76
31 Phase of the angular transfer function calculated for the amplitudes of Fig. 29 with external cutoff angles of $\tilde{\theta}_c$ of 1.5° , and 2.3°	76
32 Phase of the angular transfer function calculated for the amplitude of Fig. 30 with external cutoff angle of $\tilde{\theta}_c$ of 4.0°	77
33 Normalized recombination rate as a function of time delay τ with realistic dispersion parameters of four-prism compensated, two-path configurations assuming 5 mm long lithium niobate crystals and an external cutoff angle $\tilde{\theta}_c$ of 2.3°	79

List of figures (continued)

Figure	Page
34 Phase of the delayed transfer efficiency as a function of the time delay τ corresponding to the cases shown in Fig 33.	80
35 Normalized recombination rate as a function of the time delay τ with dispersion parameters as in Fig. 3(a) in Ref. O'Donnell (2011) and an external cutoff angle $\tilde{\theta}_c$ of 4.0°	80
36 Phase of the delayed transfer efficiency as a function of the time delay τ corresponding to the case shown in Fig 35.	81
37 Normalized recombination rate as a function of the time delay τ with realistic dispersion parameters of three non-compensated, two-path configurations assuming 5 mm lithium niobate crystals and an external cutoff angle of $\tilde{\theta}_c$ of 2.3°	82
38 Normalized recombination rate as a function of the time delay τ with realistic dispersion parameters of three non-compensated, two-path configurations assuming 5 mm lithium niobate crystals and an external cutoff angle of $\tilde{\theta}_c$ of 2.3°	82

List of tables

Table	Page
1	Signal ($\epsilon = s$) and idler ($\epsilon = i$) filters used for detection of three narrowband SPDC interactions. 41

Chapter 1. Introduction

The study of the emission produced in the process of spontaneous parametric down-conversion (SPDC) in nonlinear optical materials and its applications has been of interest over more than 50 years (Louisell *et al.*, 1961; Harris *et al.*, 1967). This emission is produced in a crystal having a second-order non-linearity, where photons from a pump laser spontaneously split into pairs of photons of lower frequency. The two members of a pair form an entangled quantum system, with each pair having the same total energy as the pump photon that created it. The members of the photon pair, called signal and idler, carry nonclassical correlations widely known as quantum entanglement, which has inspired a wide range of research directed toward both fundamental studies as well as applications (Zel'Dovich and Klyshko, 1969; Hong and Mandel, 1985; Ghosh and Mandel, 1987; Hong *et al.*, 1987; Strekalov *et al.*, 1995; Hamar *et al.*, 2010). In general the photon pairs may be entangled in all of their degrees of freedom including polarizations, wavelengths, and emission angles.

Although this phenomenon has attracted considerable interest, particularly since the observation of the simultaneity of the pairs (Burnham and Weinberg, 1970), it is perhaps surprising that fundamental theoretical and experimental aspects such as the realistic multimodal description of the interacting fields and the issue of quantitative scale have received relatively little attention (Byer and Harris, 1968). Another aspect of interest which is seldom addressed in studies of photon pairs is the accurate theoretical description of realistic experimental situations accounting for important characteristics such as pump beam geometry, integration angles, and detection bandwidth. Indeed, the description of many well-known quantum optical experiments has been formalized only within the framework of overtly simplified single-mode theories. The strongest exception to this remains the groundbreaking work by Klyshko (Klyshko, 1988), with its rigorous and general development and its treatment of dimensionality and scale.

More recently, the novel effects that arise in experiments using two nonlinear crystals have attracted particular interest. If the two crystals are coherently pumped, it has been shown that introducing the idler photons of the SPDC from one crystal into another induces coherence between the signal photons of the two crystals (Wang *et al.*, 1991; Zou *et al.*, 1991). Further, overlapping the SPDC cones produced by two

crystals has been found to produce interference fringes in the detected photon pair rates, whose phase depends on the pump phase difference between the two crystals (Ou *et al.*, 1989, 1990; Burlakov *et al.*, 1997). Here, we study theoretically a different situation in which similar effects appear. We also consider a case with two nonlinear crystals, although only the first one is pumped to produce the photon pairs. The pump beam is then removed and, after dispersion compensation, the SPDC emission cone is focused in the second crystal. There, an entangled photon pair can recombine into a single photon that, from energy conservation, has the same frequency spectrum as the pump photon that produced the pair. These effects have been studied experimentally (Dayan *et al.*, 2005; Peer *et al.*, 2005; O'Donnell and U'Ren, 2009; O'Donnell, 2011; O'Donnell and Garces, 2015) using periodically poled crystals, which is our interest here, as well as using nonlinear waveguides (Lukens *et al.*, 2013, 2014; Odele *et al.*, 2015); however, the theoretical description of such studies have not considered the general case in which the multimodal quantum nature of all interacting fields is fully accounted for.

This situation is widespread in quantum optics, and has arisen partly out of a necessity to produce an understanding of existing results by workers in the field, but also due to an apparent divide between experimentalists and theorists, as recognized by Luks and Perinova in their seminal treatise “Quantum aspects of light propagation” (Luks and Perinová, 2009):

Ingenious, but simple solutions are preferred to intricacies of the quantized field theory with the hope that experimenters realize the simple proposals with appropriate means.

In this work, we present the results of a research program that intended to approach these topics from a perspective that appears diametrically opposed to the more-common approach, one where every attempt has been made to accurately represent the relevant aspects of the experimental situation. The primary motivation for producing such a description of the photon-pair generation process in our theoretical work has been to apply these methods to the phenomenon of recombination, which necessitates a multimodal treatment of all fields and manifests the shortcomings of existing formulations.

The theoretical methods used to describe the two-photon amplitude produced in

SPDC are presented in Chapter 2. From this fundamental result, we calculate the two-photon amplitude of the unconverted light and use it to derive expressions for the coincident photon pair rate, the photon emission rate, and the down-converted power under more general conditions that are usually considered including arbitrary forms of the frequency spectra and transverse amplitude profile for weakly focused pumps, along with exact solutions for the important case of focused Gaussian beams. In Chapter 3, we apply our method to calculate the up-converted amplitude which is produced by recombination of entangled photon pairs in an identical crystal as is used to generate them. The experimental arrangement for photon pair detection shown in Chapter 4 presents a simple, yet flexible detection method that allows measurement of the broadband and narrowband-filtered non-collinear photon pairs. In Chapter 5, a set of calculations corresponding to the recombination of photon pairs is presented and discussed. These calculations include an idealized case and two realistic cases. The conclusions and closing comments are found in Chapter 6, and a discussion of a fundamental symmetry in the two-photon state is demonstrated in the Appendix.

Chapter 2. Theory of entangled photon pair generation

The spatio-temporal properties of the two-photon amplitude that is generated in the process of SPDC have been described (Rubin *et al.*, 1994; Joobeur *et al.*, 1994, 1996), and the calculated relative photon pair rates have been compared favorably with experimental observations (Hamar *et al.*, 2010; Jimenez *et al.*, 2017). Recently, we have briefly presented a formal quantum optical theory of this phenomenon where all interacting fields, including the pump, are considered to be multi-modal quantum optical fields (Jimenez *et al.*, 2019). In this chapter, we present in detail this quantitative theory of SPDC, and will describe the relationship between the theoretical formulation and experimentally available parameters such as limiting apertures and frequency filters in photon-pair detection experiments. Our development requires few simplifying assumptions, applies to the cases of bulk and periodically-poled materials, and is used to calculate pair rates assuming realistic detection conditions.

We consider the pump field as a coherent state of general spatial distribution and spectrum, and also study the limiting cases of narrow-band and wide-beam fields. These limits are taken in a manner that differs from the usual approach (Blow *et al.*, 1990; Hamar *et al.*, 2010), but which respects the normalization of the state and is dimensionally correct. We use first-order perturbation theory in the interaction picture to calculate the state of down-converted light, and discuss the topic of state normalization and its formal implications. As will be shown in Chapter 4, considering the pump as a quantum field in the theoretical description of photon pair recombination permits the formal calculation of the coherence function between the pump and recombined field.

An extension of the continuum approach proposed by Blow and Loudon (Blow *et al.*, 1990) is employed to describe spatially multimodal fields with continuous spectra in wave-vector space. This approach is suited naturally to the study of quantum optical fields in open systems; it has been employed here over the more common volume quantization approach as the results are all independent of the quantization volume and our approach avoids an unnecessary procedure to produce the continuum limit. From a canonical quantization procedure (Huttner and Barnett, 1992), it has been shown that the ladder operators that appear in the electric field operators and Hamiltonian within dispersive media act to create and annihilate the photons as well as the

polarization waves that are generated in the material. This quantum field theoretical description is then said to be written in terms of these so-called ‘dressed photons’ (Luks and Perinová, 2009).

2.1 Quantum representation of the pump

The pump is defined as a multi-modal coherent state which is the solution to the eigenvalue equation (Blow *et al.*, 1990)

$$\hat{a}(\mathbf{k}_p) |\{\psi_p\}\rangle = \sqrt{N_p} \psi_p(\mathbf{k}_p) e^{i\Phi_p} |\{\psi_p\}\rangle, \quad (1)$$

for all \mathbf{k}_p , where $\mathbf{k}_p = \frac{n_p \omega_p}{c} \mathbf{e}_p$ is the frequency-dependent wave-vector of the pump within the nonlinear medium with internal angles $\theta_p \geq 0$ and $-\pi < \phi_p \leq \pi$, c is the speed of light in the vacuum, $\mathbf{e}_p = \mathbf{k}_p / |\mathbf{k}_p|$ is a unitary vector, $n_p = n(\omega_p)$ is the refractive index at the pump frequency, $\psi_p(\mathbf{k}_p)$ is the pump amplitude in \mathbf{k} -space, Φ_p is an arbitrary pump phase, and

$$N_p = \int d\mathbf{k}_p \langle \{\psi_p\} | \hat{a}^\dagger(\mathbf{k}_p) \hat{a}(\mathbf{k}_p) | \{\psi_p\} \rangle \quad (2)$$

is the mean number of pump photons in a characteristic time Δt which, for continuous wave experiments, is considered long compared with the optical wavelength. Equations 1 and 2, along with the normalization condition $\langle \{\psi_p\} | \{\psi_p\} \rangle = 1$, imply that the pump amplitude $\psi_p(\mathbf{k})$ itself is normalized according to

$$\int d\mathbf{k}_p |\psi_p(\mathbf{k}_p)|^2 = 1. \quad (3)$$

We note that $\hat{a}(\mathbf{k}_p) |\{\psi_p\}\rangle$, the probability amplitude of the photon number in our coherent field, is then continuously distributed over an open subset of \mathbf{k} -space, and that the form of the state is dependent on Δt . Likewise, $|\psi_p(\mathbf{k}_p)|^2$ is the probability density function which describes the angular distribution and spectrum of a pump photon. The total pump photon rate is then given by $R_p = N_p / \Delta t$, and the photon rate over an arbitrary detection domain \mathcal{D}_p is simply $R_p \int_{\mathcal{D}_p} d\mathbf{k}_p |\psi_p(\mathbf{k}_p)|^2$. The detection domain \mathcal{D}_p is defined as the set of wave-vectors which are coupled to an idealized detector. In the

simple case of observations performed with a single-bandpass frequency filter and a limiting aperture, it may be written in set-constructor notation as

$$\mathcal{D}_p = \left\{ \mathbf{k}_p \mid \omega_{\min} < \omega_p(\mathbf{k}_p) < \omega_{\max} \text{ and } (\theta_p(\mathbf{k}_p), \phi_p(\mathbf{k}_p)) \in \Omega_p \right\}, \quad (4)$$

where ω_{\min} and ω_{\max} are the cutoff frequencies of the bandpass and Ω_p is the solid angle that is coupled into the detector. Where necessary, one can introduce the effects of imperfect coupling and detection efficiency as a multiplicative factor to $|\psi_p(\mathbf{k}_p)|^2$.

2.1.1 Frequency and angular amplitude spectrum of the pump

It will be convenient to write the amplitude $\psi_p(\mathbf{k}_p)$ in terms of the frequency and angular variables as

$$\psi_p(\mathbf{k}_p) = \frac{\mathcal{A}(\omega_p)}{\sqrt{\eta_p} k_p} \mathcal{F}(\theta_p, \phi_p | \omega_p), \quad (5)$$

where $k_p = |\mathbf{k}_p(\omega_p, \theta_p, \phi_p)|$, $\eta_p = \eta(\omega_p)$ is the reciprocal of the group velocity at frequency ω_p , and the functions $\mathcal{A}(\omega_p)$ and $\mathcal{F}(\theta_p, \phi_p | \omega_p)$ define, respectively, the frequency and angular distribution of the pump amplitude. The differential in Eq. 3 is expanded exactly with

$$d\mathbf{k}_p = d\omega_p d\theta_p d\phi_p k_p \eta_p \sin \theta_p, \quad (6)$$

so that Eq. 3 is then satisfied by requiring that

$$\int d\omega_p |\mathcal{A}(\omega_p)|^2 = 1 \quad (7)$$

as well as the condition that, for all ω_p ,

$$\iint d\theta_p d\phi_p \sin \theta_p |\mathcal{F}(\theta_p, \phi_p | \omega_p)|^2 = 1. \quad (8)$$

If the coherent field is attenuated strongly, to the point where the probability amplitude for finding more than one photon in time Δt can be neglected, the state may

be written as (Glauber, 1963a)

$$|\{\psi_p\}\rangle = \left[M_p \hat{I} + \gamma \sqrt{N_p} \int d\mathbf{k}_p \psi_p(\mathbf{k}_p) e^{i\Phi_p} \hat{a}^\dagger(\mathbf{k}_p) \right] |\text{vac}\rangle, \quad (9)$$

where γ is the probability amplitude attenuation factor, with $|\gamma| \ll 1$, and $M_p = \sqrt{1 - \gamma^2 N_p}$ is a normalization factor. This expression for the single-photon field represents a coherent superposition of a vacuum state and a single photon state, where the vacuum carries most of the probability amplitude, and will prove useful in the calculation of certain coherence properties in Chapter 3.

2.2 The interaction Hamiltonian and electric field operators

The three-photon processes that take place in second-order nonlinear optical crystals are governed by the interaction Hamiltonian (Mandel and Wolf, 1995)

$$\hat{H}_{\text{int}}(t) = 2\epsilon_0 \int_V d\mathbf{r} d(z) \hat{E}_p^{(+)}(\mathbf{r}, t) \hat{E}_s^{(-)}(\mathbf{r}, t) \hat{E}_i^{(-)}(\mathbf{r}, t) + \text{H.c.}, \quad (10)$$

where the term that is explicitly written is that which produces down-conversion, ϵ_0 is the permittivity of the vacuum, $d(z) = d_{\text{eff}} e^{i\mathbf{k}_g \cdot \mathbf{r}}$ for first order periodic poling, V is the crystal volume, and H.c. denotes the Hermitian conjugate. In our case, we consider that the poling wave-vector \mathbf{k}_g is parallel to the z axis which conforms to the experimental situation and slightly simplifies some aspects of the calculation; however, it is entirely possible to consider the more general case of arbitrary orientations for the poling wave-vector, as well as the bulk crystal case by taking $\mathbf{k}_g = 0$. The spatial integration is to be performed over the interaction volume, which is determined by L , the crystal length along the z propagation axis, and is considered here to be unbounded in the transverse dimensions. These conditions are applicable for the common case where the size of the pump is significantly smaller than the transverse crystal dimensions.

We consider the three-dimensional representation for the time-dependent quantum

electric field operator within the dielectric (Blow *et al.*, 1990; Luks and Perinová, 2009)

$$\hat{E}_\epsilon^{(+)}(\mathbf{r}, t) = i \int d\mathbf{k}_\epsilon \sqrt{\frac{\hbar \omega_\epsilon}{16\pi^3 \epsilon_0 c n_\epsilon \eta_\epsilon}} \hat{a}(\mathbf{k}_\epsilon) e^{-i(\omega_\epsilon t - \mathbf{k}_\epsilon \cdot \mathbf{r})}, \quad (11)$$

where \hbar is the reduced Planck constant, ϵ may denote the pump ($\epsilon = p$), signal ($\epsilon = s$) and idler ($\epsilon = i$) fields, $\hat{a}(\mathbf{k}_\epsilon)$ is the photon annihilation operator for the plane wave mode with wave-vector \mathbf{k}_ϵ , and $\hat{E}_\epsilon^{(-)}(\mathbf{r}, t) = [\hat{E}_\epsilon^{(+)}(\mathbf{r}, t)]^\dagger$. With this, the Hamiltonian may be written as

$$\begin{aligned} \hat{H}_I(t) = & -2id_{\text{eff}}\epsilon_0 \left(\frac{\hbar}{16\pi^3 \epsilon_0 c} \right)^{3/2} \int_{-L/2}^{L/2} dz \int dx \int dy \\ & \times \int d\mathbf{k}_p \int d\mathbf{k}_s \int d\mathbf{k}_i \sqrt{\frac{\omega_p \omega_s \omega_i}{n_p n_s n_i \eta_p \eta_s \eta_i}} \\ & \times \hat{a}(\mathbf{k}_p) \hat{a}^\dagger(\mathbf{k}_s) \hat{a}^\dagger(\mathbf{k}_i) e^{-i(\omega_p - \omega_s - \omega_i)t} e^{i\Delta\mathbf{k} \cdot \mathbf{r}} + \text{H.c.}, \end{aligned} \quad (12)$$

where

$$\Delta\mathbf{k} = \mathbf{k}_p - \mathbf{k}_s - \mathbf{k}_i - \mathbf{k}_g \quad (13)$$

is the wave-vector mismatch. In practice it has been found that (Emanuelli and Arie, 2003), when using periodically-poled potassium titanyl phosphate (PPKTP), an additional wave-vector $\tilde{\mathbf{k}}$, whose value is dependent on crystal temperature and the signal/idler wavelengths, and which is collinear with \mathbf{k}_p and \mathbf{k}_g , must be subtracted from the right hand side of Eq. 13 to accurately describe the observed experimental behavior; the origin of this correction term is not well understood at this time, and has not been found to be necessary in experiments using other periodically-poled nonlinear crystals, such as lithium niobate, in similar experiments. The operator $\hat{H}_I(t)$, as an observable that determines the dynamics of the three-photon interaction, is an object of interest in the study of the SPDC process.

2.3 Temporal evolution and spatial integrations

In the following, we restrict our analysis to calculating the steady state solution produced by fields that are assumed to be stationary, so that the number density is time-independent and the characteristic time Δt may be considered long. The unitary time evolution operator $e^{-i\hat{H}_I(t-t_0)/\hbar}$, with $t \geq t_0$, acts continuously on the input state $|\text{in}\rangle = |\psi_p\rangle_p |\text{vac}\rangle_{s,i}$ from time t_0 to create the response at time t . If the initial time t_0 is far in the past, the output state is given by

$$|\text{out}(t)\rangle = \lim_{t_0 \rightarrow -\infty} \int_{t_0}^t dt' e^{-i\hat{H}_I(t-t_0)/\hbar} |\text{in}\rangle, \quad (14)$$

and the stationary state is then simply $|\text{out}\rangle = \lim_{t \rightarrow \infty} |\text{out}(t)\rangle$. It is important to note that the infinite limits of the temporal integration are to be interpreted as a useful approximation and not as a formal argument. Strictly, for a pure state description to hold, the integration domain may not be larger than a coherence time of the pump field; for our purposes, however, this is not a significant limitation as the formal integration time only need-be significantly larger than the optical period of the pump for the system to reach the steady state. A generalization of this method to time-dependent fields is of interest, and should clarify the interpretation of the limits of integration and characteristic time Δt

When the spontaneous limit applies, we may approximate Eq. 14 using only the first order term in perturbation theory as (Ou *et al.*, 1989; Holstein and Ashkin, 1992; Rubin *et al.*, 1994)

$$|\text{out}\rangle = \left\{ \hat{I} - \frac{i}{\hbar} \int_{-\infty}^{\infty} dt H_I(t) \right\} |\{\psi_p\}\rangle_p |\text{vac}\rangle_{s,i}, \quad (15)$$

where $|\text{vac}\rangle_{s,i}$ is the direct product state where the two-photon modes with signal and idler wave-vectors \mathbf{k}_s and \mathbf{k}_i are simultaneously vacuum. After substituting the Hamiltonian of Eq. 12 into Eq. 14 and applying Eq. 1, we may factor out the pump state immediately and reach

$$|\text{out}\rangle = |\{\psi_p\}\rangle |\psi_{\text{SPDC}}\rangle, \quad (16)$$

where

$$\begin{aligned}
|\psi_{\text{SPDC}}\rangle &= \left\{ \hat{I} - 2\sqrt{\frac{N_p d_{\text{eff}}^2 \hbar}{(16\pi^3)^3 \epsilon_0 c^3}} \int_{-\infty}^{\infty} dt \int_{-L/2}^{L/2} dz \int dx \int dy \right. \\
&\times \int d\mathbf{k}_p \int d\mathbf{k}_s \int d\mathbf{k}_i \sqrt{\frac{\omega_p \omega_s \omega_i}{n_p n_s n_i \eta_p \eta_s \eta_i}} e^{i\Delta\mathbf{k} \cdot \mathbf{r}} e^{-i(\omega_p - \omega_s - \omega_i)t} \\
&\times \left. \frac{\psi_p(\mathbf{k}_p)}{\cos \theta_p^o} e^{i\Phi_p} \hat{a}^\dagger(\mathbf{k}_s) \hat{a}^\dagger(\mathbf{k}_i) \right\} |\text{vac}\rangle_{s,i}
\end{aligned} \tag{17}$$

is the downconverted state. The temporal integration is performed and yields $2\pi\delta(\omega_p - \omega_s - \omega_i)$, while the xy spatial integrations yield $(2\pi)^2\delta(\Delta k_x)\delta(\Delta k_y)$, where $\Delta k_\alpha = \Delta\mathbf{k} \cdot \mathbf{e}_\alpha$ for $\alpha \in \{x, y, z\}$. In most situations, it is customary to neglect the identity operator \hat{I} from Eq. 17, yet we shall keep it for completeness.

2.3.1 The longitudinal Quasi Phase-Matching function

The down-converted state may then be written as

$$\begin{aligned}
|\psi_{\text{SPDC}}\rangle &= \left\{ \hat{I} - \sqrt{\frac{N_p d_{\text{eff}}^2 L^2 \hbar}{16\pi^3 \epsilon_0 c^3}} \int d\mathbf{k}_p \int d\mathbf{k}_s \int d\mathbf{k}_i \right. \\
&\times \sqrt{\frac{\omega_p \omega_s \omega_i}{n_p n_s n_i \eta_p \eta_s \eta_i}} \delta(\omega_p - \omega_s - \omega_i) \delta(\Delta k_x) \delta(\Delta k_y) \\
&\times \left. \psi_p(\mathbf{k}_p) s(\Delta k_z) e^{i\Phi_p} \hat{a}^\dagger(\mathbf{k}_s) \hat{a}^\dagger(\mathbf{k}_i) \right\} |\text{vac}\rangle_{s,i},
\end{aligned} \tag{18}$$

where we have ignored the z dependence of the pump amplitude, as it is adequate in the case of a weakly focused pump, to find

$$\begin{aligned}
s(\Delta k_z) &= \frac{1}{L} \int_{-L/2}^{L/2} dz e^{i\Delta k_z z} \\
&= \text{sinc}\left(\frac{\Delta k_z L}{2}\right),
\end{aligned} \tag{19}$$

which is known as the longitudinal quasi-phasematching (QPM) function.

2.4 The quantum state of down-converted light and the two-photon amplitude

The $d\mathbf{k}_p$ differential is now expanded as in Eq. 6. With this, the frequency integration is trivial and sets

$$\omega_p = \omega_s + \omega_i, \quad (20)$$

which is the energy conservation condition. The pump angular integrations are performed using the identity that,

$$\iint d\theta_p d\phi_p \sin \theta_p f(\theta_p, \phi_p) \delta(\Delta \mathbf{k}_x) \delta(\Delta \mathbf{k}_y) = \frac{f(\theta_p^o, \phi_p^o)}{k_p^2 \cos \theta_p^o}, \quad (21)$$

where the angles θ_p^o and ϕ_p^o are the solutions to $\Delta \mathbf{k}_\perp = \mathbf{0}$, which are

$$\tan \phi_p^o = \frac{k_s \sin \theta_s \sin \phi_s + k_i \sin \theta_i \sin \phi_i}{k_s \sin \theta_s \cos \phi_s + k_i \sin \theta_i \cos \phi_i} \quad (22)$$

$$\sin \theta_p^o = \frac{k_s \sin \theta_s \cos \phi_s + k_i \sin \theta_i \cos \phi_i}{k_p \cos \phi_p^o}. \quad (23)$$

The conditions defined by Eqs. 20- 23 allow us to write the pump wave-vector as a function of the signal and idler variables in the form

$$\mathbf{k}_p = \mathbf{k}(\omega_s + \omega_i, \theta_p^o, \phi_p^o) = \mathbf{k}_p^+ \quad (24)$$

Having performed the integrations, the down-converted state from Eq. 18 is now

$$|\psi_{\text{SPDC}}\rangle = \left\{ \hat{I} - \int d\mathbf{k}_s \int d\mathbf{k}_i \psi(\mathbf{k}_s, \mathbf{k}_i) \hat{a}^\dagger(\mathbf{k}_s) \hat{a}^\dagger(\mathbf{k}_i) \right\} |\text{vac}\rangle_{s,i}, \quad (25)$$

where we have introduced the two-photon amplitude, which is given by

$$\psi(\mathbf{k}_s, \mathbf{k}_i) = \sqrt{\frac{N_p d_{\text{eff}}^2 L^2 \hbar (\omega_s + \omega_i) \omega_s \omega_i \eta_p^+}{16 \pi^3 \epsilon_0 c^3 n_p^+ n_s n_i \eta_s \eta_i}} \psi_p(\mathbf{k}_p^+) s(\Delta k_z) e^{i\phi_p} \quad (26)$$

where $n_p^+ = n(\omega_s + \omega_i)$, and $\eta_p^+ = \eta(\omega_s + \omega_i)$.

For the quasi-phasematched interactions that we will focus on in this work, all fields are linearly polarized along the same crystal axis, and we may ignore the polarization vector in the electric field operators of Eq. 11. For the case of SPDC produced in bulk materials, Eqs. 25 and 26 still apply as long as the relevant effective nonlinear coefficient is considered and the simplification $\mathbf{k}_g = \mathbf{0}$ is made. In this case, $s(\Delta k_z)$ is referred to as the longitudinal phasematching function. We will later consider a correction to this solution which accounts for focusing in the pump field.

2.5 Calculation of the rates

In this section, we will derive expressions for the rate of pair detection from our two-photon state. These will proceed from the general case into the particular, by taking limits that approximately correspond to important experimental situations, *viz.* the narrowband and wide-beam pump limit, and will culminate with a simple expression for the rate of single photon detection and the corresponding of the down-converted power in this final limit.

2.5.1 Photon pair rates

The time-averaged number density, in signal-idler wave-vector space, for the photon pairs in the quantum state $|\psi_{\text{SPDC}}\rangle$ of Eq. 25 is given by the fourth order coherence function (Glauber, 1963b; Joobeur *et al.*, 1994; Rubin *et al.*, 1994)

$$\begin{aligned}
 G_{si}^{(2)}(\mathbf{k}_s, \mathbf{k}_i) &= \langle \psi_{\text{SPDC}} | \hat{a}^\dagger(\mathbf{k}_s) \hat{a}^\dagger(\mathbf{k}_i) \hat{a}(\mathbf{k}_s) \hat{a}(\mathbf{k}_i) | \psi_{\text{SPDC}} \rangle \\
 &= \langle \text{vac} | \left[\hat{I} - \int d\mathbf{k}_s'' \int d\mathbf{k}_i'' \psi^*(\mathbf{k}_s'', \mathbf{k}_i'') \hat{a}(\mathbf{k}_s'') \hat{a}(\mathbf{k}_i'') \right] \\
 &\quad \times \hat{a}^\dagger(\mathbf{k}_s) \hat{a}^\dagger(\mathbf{k}_i) \hat{a}(\mathbf{k}_s) \hat{a}(\mathbf{k}_i) \\
 &\quad \times \left[\hat{I} - \int d\mathbf{k}_s' \int d\mathbf{k}_i' \psi(\mathbf{k}_s', \mathbf{k}_i') \hat{a}^\dagger(\mathbf{k}_s') \hat{a}^\dagger(\mathbf{k}_i') \right] | \text{vac} \rangle \\
 &= |\psi(\mathbf{k}_s, \mathbf{k}_i)|^2
 \end{aligned} \tag{27}$$

where we have used the commutation relation (Blow *et al.*, 1990; Huttner and Barnett, 1992)

$$[\hat{a}(\mathbf{k}), \hat{a}^\dagger(\mathbf{k}')] = \delta(\mathbf{k} - \mathbf{k}'), \quad (28)$$

along with the ground state property $\langle \text{vac} | \hat{a}^\dagger(\mathbf{k}) \hat{a}(\mathbf{k}) | \text{vac} \rangle = 0$. For stationary fields, the mean photon pair rate R_π over a pair detection domain \mathcal{D}_π can then be calculated as (Jimenez *et al.*, 2019)

$$\begin{aligned} R_\pi &= \frac{1}{\Delta t} \int_{\mathcal{D}_\pi} d\mathbf{k}_s \int_{\mathcal{D}_\pi} d\mathbf{k}_i |\psi(\mathbf{k}_s, \mathbf{k}_i)|^2 \\ &= \beta c^2 R_p \int_{\mathcal{D}_\pi} d\mathbf{k}_s \int_{\mathcal{D}_\pi} d\mathbf{k}_i \frac{\hbar \omega_p \omega_s \omega_i}{n_p n_s n_i \eta_s \eta_i} \\ &\quad \times \frac{|\mathcal{A}(\omega_p)|^2}{k_p^{+2} \cos^2 \theta_p^0} |\mathcal{F}(\theta_p^0, \phi_p^0 | \omega_p)|^2 |s(\Delta k_z)|^2, \end{aligned} \quad (29)$$

where $\beta = \frac{d_{\text{eff}}^2 L^2}{16 \pi^3 \epsilon_0 c^5}$, and where the pair detection domain \mathcal{D}_π is defined by the detection apertures and filters of the pair of detectors. We note that, although it is commonplace to refer to the photons that reach one of the detectors as ‘signal’ and the photons that reach the other as ‘idler’, in the correctly formulated theory the signal and idler monikers are entirely interchangeable in all cases, including the case of non-degenerate photon pairs. Although this notion may seem contradictory at first, this simply means that, in every circumstance, half of the photons detected through an arbitrary aperture are signal and the other half are idler. This has the obvious consequence that $\psi(\mathbf{k}_s, \mathbf{k}_i) = \psi(\mathbf{k}_i, \mathbf{k}_s)$, as may be verified from Eq. 26. Another consequence of this signal-idler symmetry is that the pair-detection domain is the union of the two single-photon detection domains, which appears perhaps unintuitive, and implies that the detection domain can be divided into four parts (one with each of the possible combinations of the two detection domains, usually only there are only two of these that contribute to the observation, namely those in which the signal and idler photons are emitted into opposite sides, yet there are conditions where the two other terms will contribute *cf.* (O’Donnell and Garces, 2015)).

To reconcile our formulation with the usual interpretation, where one detector is labeled ‘signal’ with detection domain \mathcal{D}_s and the other is labeled ‘idler’ with detection domain \mathcal{D}_i , we assume the intersection $\mathcal{D}_s \cap \mathcal{D}_i$ is empty. This allows us to write the rate

of coincident detection in the experimentally relevant form

$$R_\pi = \frac{2}{\Delta t} \int_{\mathcal{D}_s} d\mathbf{k}_s \int_{\mathcal{D}_i} d\mathbf{k}_i |\psi(\mathbf{k}_s, \mathbf{k}_i)|^2 \quad (30)$$

and, for completeness, the mean number of photon pairs generated in time Δt is given by $N_\pi = R_\pi \Delta t$. It is this last form of Eq. 30 that we use in the rest of the section to derive the coincidence rate in some cases of interest. In producing Eq. 30 from Eq. 29 we have recognized that the two terms of form $\int_{\mathcal{D}_e} \int_{\mathcal{D}_e} |\psi(\mathbf{k}_s, \mathbf{k}_i)|^2$, which contribute to the pair rate near the optical axis in the general case, do not contribute to the coincidence detection rate as measured using single photon detectors with non overlapping detection domains. Although the generated pair rate of Eq. 29 and the detected coincidence rate for non-overlapping detectors of Eq. 30 may be different in the general case, the difference is only significant for near-axial observations (to within a divergence angle of the pump beam). Moreover, these quantities become exactly equal in the limit of an axial plane wave pump since all of the signal and idler photons are emitted into opposite ends of the optical axis under this condition. In simple terms, the main difference between Eq. 29 and 30 is that the latter will not consider a pair if both members went through the same detector aperture, and as such is better suited for the off-axis direct coincidence detection experiments that will be presented in Chapter 4.

2.5.2 Gaussian beam and the focused beam correction

In the derivation of Eqs. 25 and 26, the implicit assumption is made that the pump amplitude profile is constant along the propagation direction, which is a useful approximation but one that remains unphysical nonetheless. We shall now consider the effects introduced in the two-photon amplitude due to focusing of the pump by assuming a Gaussian beam form of the pump and keeping the explicit z spatial dependence of the angular distribution. Then, the angular distribution of the pump amplitude is given by

$$\mathcal{F}(\theta_p, \phi_p | \omega_p, z) = \frac{w_0 k_p}{\sqrt{2\pi}} e^{-\frac{w_0^2 k_p^2 \sin^2 \theta_p}{4}} e^{-\frac{ik_p z \sin^2 \theta_p}{2}}, \quad (31)$$

which is in accordance with Eq. 8 to first order in θ_p . The frequency distribution is also considered Gaussian with an amplitude distribution given by

$$\mathcal{A}(\omega_p) = \frac{1}{\sqrt{\sigma_p}(2\pi)^{1/4}} e^{-\frac{(\omega_p - \omega_p^0)^2}{4\sigma_p^2}}, \quad (32)$$

which satisfies Eq. 7, and where σ_p is the width of the pump spectrum, here defined as the standard deviation of $|\mathcal{A}(\omega_p)|^2$.

Note that the exponential with the imaginary argument in Eq. 31 is a linear function of z , and this term will contribute to the longitudinal integration in Eq. 18. Now the longitudinal QPM function is given by

$$\begin{aligned} \frac{1}{L} \int_{L/2}^{L/2} dz e^{i\Delta k_z z} e^{-i\frac{k_p \sin^2 \theta_p}{2} z} &= \text{sinc} \left\{ \left(\Delta k_z - \frac{k_p \sin^2 \theta_p}{2} \right) \frac{L}{2} \right\} \\ &= s \left(\Delta k_z - \frac{k_p \sin^2 \theta_p}{2} \right), \end{aligned} \quad (33)$$

where we have written the result in terms of the same longitudinal QPM function s used for the weakly focused case. The correction due to pump focusing then amounts only to a change in the argument of the longitudinal QPM function. In Eq. 26, the argument of the s function will be evaluated at $\mathbf{k}_p^+ \theta_p^0$ and ϕ_p^0 , and this implies that the conditions required for perfect QPM in the plane-wave case are not changed by this correction, as perfect QPM implies that $\theta_p^0 = 0$. This focusing correction had been obtained previously within the semi-classical approach (U'Ren *et al.*, 2003).

2.5.3 Narrowband and wide-beam limits

The description at the quantum-state level of a narrow-band or wide-beam field for the pump of the SPDC process presents a theoretical difficulty, given that a complete description of the down-converted field requires a manifestly three dimensional (per photon) multimodal approach. Within our formulation, the limiting cases of narrow-band and wide-beam pump can be considered by use of the expression for the pair

rate from Eq. 30. In the narrow-band pump limit we have that

$$\lim_{\sigma_p \rightarrow 0} |\mathcal{A}(\omega_p)|^2 = \delta(\omega_p - \omega_p^0). \quad (34)$$

The idler frequency integration in Eq. 30 may then be performed and R_π becomes

$$\begin{aligned} R_\pi &= 2\beta c^2 R_p \hbar \omega_p^0 \int_{\mathcal{D}_s} d\mathbf{k}_s \iint_{\Delta\Omega_i} d\theta_i d\phi_i \frac{\omega_s \omega_i}{n_p n_s n_i \eta_s} \\ &\times \frac{k_i^2 \sin \theta_s}{k_p^{+2} \cos^2 \theta_p^0} \left| \mathcal{F}(\theta_p^0, \phi_p^0 | \omega_p^0) \right|^2 |s(\Delta k_z)|^2 T_i(\omega_i), \end{aligned} \quad (35)$$

where $\omega_i = \omega_p^0 - \omega_s$, $\Delta\Omega_i$ is the solid angle implicit in the detection domain \mathcal{D}_i , and $T_i(\omega_i)$ is the filter transmission function for the idler photon. Since experiments are often performed with narrow-band pump conditions, Eq. 35 is commonly useful. This portion of our derivation differs from previous formulations (Blow *et al.*, 1990), which take the pump amplitude frequency distribution as $\mathcal{A}(\omega_p) \propto \delta(\omega_p - \omega_p^0)$. Such approach is attractive, but ultimately flawed, as these singular states are not normalizable; we assume it is the intensity spectrum that is singular so that these limiting results follow from analysis of finite probability amplitudes. As for the benefits of our methods, the formal divergences in the calculation of the photon pair number operator expectation of the form $\int d\omega_p \delta(\omega_p - \omega_p^0) \delta(\omega_p - \omega_p^0)$ for fields of finite power do not appear here, and the dimensional analysis along with the interpretation of the quantitative scale is simplified.

Further, in the wide-pump limit we have that

$$\begin{aligned} \lim_{\omega_0 \rightarrow \infty} |\mathcal{F}(\theta_p^0, \phi_p^0 | \omega_p^0)|^2 &= \delta(k_{s,x} + k_{i,x}) \delta(k_{s,y} + k_{i,y}) \\ &= \delta(k_p^+ \sin \theta_p^0 \cos \phi_p^0) \delta(k_p^+ \sin \theta_p^0 \sin \phi_p^0), \end{aligned} \quad (36)$$

where we have used the condition $\Delta\mathbf{k} = \mathbf{0}$ that was used to establish Eqs. 22-23 to write the arguments of the delta functions in terms of signal and idler variables. We then perform the idler angular integrations using the identity

$$\iint_{\Delta\Omega_i} d\theta_i d\phi_i \sin \theta_i f(\theta_i, \phi_i) \delta(k_x) \delta(k_y) = \frac{f(\theta_i^0, \phi_i^0)}{k_i^2 \cos \theta_i^0} D_i(\theta_i^0, \phi_i^0) \quad (37)$$

where $D_i(\theta_i, \phi_i)$ is a binary discrimination function, which is here considered unity if

$(\theta_i, \phi_i) \in \Delta\Omega_i$ and zero otherwise, that accounts for the effect of the observation aperture on the idler photon. Equation 37 follows from iterated application of $\delta(ax) = \delta(x)/|a|$. We then reach

$$R_\pi = 2\beta R_p \hbar \omega_p^0 \int d\omega_s \frac{\omega_s^3 \omega_i n_s}{n_p n_i} T_s(\omega_s) T_i(\omega_i) \times \iint_{\Delta\Omega_s} d\theta_s d\phi_s \frac{\sin \theta_s}{\cos \theta_i} |s(\Delta k_z)|^2 D_i(\theta_i, \phi_i), \quad (38)$$

where $\Delta\Omega_s$ is the solid angle implicit in the detection domain \mathcal{D}_s , and θ_i is now to be found from the coplanar condition $n_i \omega_i \sin \theta_i = n_s \omega_s \sin \theta_s$. This condition requires the signal and idler emission angles to be on strictly opposite sides of the optical axis, so that they are coplanar with the pump; the pair rate and detected coincidence rate are equal in this special case. We emphasize that Eqs. 29, 30, 35 and 38 predict the *absolute* rates for given experimental conditions in dimensionally correct form.

2.5.4 Singles rate and down-converted power

We now consider the signal photon rate R_s passing through a circular aperture of angular radius $\tilde{\theta}_c$, without bandwidth filtering and without any restrictions whatsoever on the idler mode. For the limiting case of a narrowband, plane wave pump along the optic axis, this follows from Eq. 38 with $D_i(\theta_i, \phi_i) = 1$ and $T_i(\omega_i) = 1$. Integrating trivially over ϕ_s , from $-\pi/2$ to $\pi/2$ to respect the assumption of non-overlapping signal and idler domains, we obtain

$$R_s = 2\pi\beta R_p \hbar \omega_p^0 \int d\omega_s \frac{\omega_s^3 \omega_i n_s}{n_p n_i} \int_0^{\Theta_s} d\theta_s \frac{\sin \theta_s}{\cos \theta_i} |s(\Delta k_z)|^2, \quad (39)$$

where $\Theta_s = \arcsin[\sin \tilde{\theta}_c / n_s]$. By changing the integration variables of Eqs. 38 and 39 from ω_s to $\omega_i = \omega_p^0 - \omega_s$, and from θ_s to its phasematched idler angle θ_i , expressions are obtained that are *identical* in form, but with signal and idler variables interchanged. This is a consequence of the symmetry that exists between signal and idler portions of the state and is a fundamental physical characteristic of the SPDC state. In the Appendix, we show explicitly how these transformed expressions with exchanged signal-idler variables can be produced, and we comment on some other important con-

sequences of this symmetry. A simple direct consequence is that $R_i = R_s$, which must be the case from physical symmetry, and the total photon rate follows as $R = R_s + R_i = 2R_s$. In the more general case, the signal rate may be calculated from Eq. 29 by taking $\mathcal{D}_\pi = \mathcal{D}_s$ for the domain of the $d\mathbf{k}_s$ integration and integrating over all wave-vector space for the $d\mathbf{k}_i$ integration, so that

$$R_s = \frac{1}{\Delta t} \int_{\mathcal{D}_s} d\mathbf{k}_s \int d\mathbf{k}_i |\psi(\mathbf{k}_s, \mathbf{k}_i)|^2 \quad (40)$$

The power of the signal light P_s follows from Eq. 39 after multiplying by Δt and using the differential relationship $dP_s = \hbar\omega_s dN_s$ as

$$P_s = 2\pi\beta P_p \int d\omega_s \frac{\hbar\omega_s^4 \omega_i n_s}{n_p n_i} \int_0^{\theta_s} d\theta_s \frac{\sin \theta_s}{\cos \theta_i} |s(\Delta k_z)|^2, \quad (41)$$

where $P_p = N_p \hbar\omega_p^0$. The integrand of Eq. 41 differs by a factor of $(4 \cos \theta_i)^{-1}$ upon comparison with a previous result (Byer and Harris, 1968); however, we note that our $(\cos \theta_i)^{-1}$ factor is essential in obtaining the correct functional symmetry discussed in relation to Eq. 39. Finally, the total SPDC power in the aperture is given by $P = P_s + P_i = 2P_s$.

2.6 Vacuum amplitude and state normalization

The state $|\psi_{\text{SPDC}}\rangle$ that is calculated from first order perturbation theory is not properly normalized. This is the case because, within this approximation, the time evolution operator is no longer unitary, and thus probability is not conserved. Surprisingly, the effect that this has on the product state $|\text{out}\rangle = |\{\psi_p\}\rangle |\psi_{\text{SPDC}}\rangle$ is manifested as an *increase* in the rate of the pump after the nonlinear interaction. This spurious increase may be removed from the result by renormalizing the state of Eq. 25 as

$$\begin{aligned} |\psi_{\text{SPDC}}\rangle &= \left\{ M_{Si} - \int d\mathbf{k}_s \int d\mathbf{k}_i \psi(\mathbf{k}_s, \mathbf{k}_i) \hat{a}^\dagger(\mathbf{k}_s) \hat{a}^\dagger(\mathbf{k}_i) \right\} |\text{vac}\rangle_{s,i} \\ &= M_{Si} |\text{vac}\rangle_{s,i} - |s, i\rangle_{s,i} \end{aligned} \quad (42)$$

where $|s, i\rangle$ is the two-photon term, and

$$\begin{aligned} M_{si} &= \sqrt{1 - N_\pi} \\ &= \sqrt{1 - R_\pi \Delta t} \end{aligned} \quad (43)$$

is the signal-idler vacuum amplitude. Equation 43 allows us to determine an upper bound for the maximal characteristic time, so that $\Delta t \leq 1/R_\pi$. It is interesting to note that normalizing the result only predicts that the coherent-state pump is *undepleted* by the nonlinear interaction, which is a consequence of the fact that the coherent state is an eigenstate of the annihilation operator.

We will now show that, for the less idealized case of a single-photon pump, appropriate renormalization implies pump depletion at a rate of one pump photon lost for each photon pair produced. For simplicity, the attenuated pump state of Eq. 9 is now written as

$$|\{\psi_p\}\rangle = M_p |\text{vac}\rangle_p + |p\rangle_p, \quad (44)$$

where

$$|p\rangle = \gamma \sqrt{N_p} \int d\mathbf{k}_p \psi_p(\mathbf{k}_p) e^{i\Phi_p} \hat{a}^\dagger(\mathbf{k}_p) |\text{vac}\rangle_p \quad (45)$$

is the single photon term. Considering Eqs. 42 and 44, the output state is now

$$|\text{out}\rangle = M_p |\text{vac}\rangle_{p,s,i} + |p\rangle_p |\text{vac}\rangle_{si} - \gamma |\text{vac}\rangle_p |s, i\rangle \quad (46)$$

where $|\text{vac}\rangle_{p,s,i} = |\text{vac}\rangle_p |\text{vac}\rangle_{s,i}$ is a direct product of pump, signal, and idler vacuum states. It is easy to show that

$$\int d\mathbf{k}_p \langle p|p\rangle = \gamma^2 N_p \quad (47)$$

and

$$\int d\mathbf{k}_s \int d\mathbf{k}_i \langle s, i|s, i\rangle = N_\pi, \quad (48)$$

with which we see that the normalized form of Eq. 46 is given by

$$|\text{out}\rangle = M_p |\text{vac}\rangle_{p,s,i} + M'_{si} |p\rangle_p |\text{vac}\rangle_{si} - \gamma |\text{vac}\rangle_p |s, i\rangle, \quad (49)$$

where

$$M'_{si} = \sqrt{1 - \mathcal{R}_\pi}, \quad (50)$$

and $\mathcal{R}_\pi = R_\pi/R_p$ is the pair conversion efficiency. With this, the pump rate is now $R_p - R_\pi$, while the pair rate remains as R_π ; if we interpret both each pump photon and each generated biphoton as a single quantum wave-packets (Shih, 2016), then this formulation is conservative with respect to the number of independent bosonic quanta. An interesting aspect to note of this result is that, in this weak pump limit, we do not find an upper bound to the characteristic time Δt , as was the case in the case of a coherent pump. We can also use Eqs. 49 and 50 to consider the particular case of a single-photon pump that has a negligible contribution of the vacuum amplitude by taking $M_p \approx 0$, which implies $N_p \approx 1$, and which represents down-conversion created by heralded pump photons.

In the following chapter, we shall present an application of this theory to describe the process of entangled photon pair recombination and, later in this work, we will present calculations produced from our results and will compare them with experimental observations. However, the generality of the method, and the various important limits that are discussed, may allow for it to be applied to a broad range of interesting phenomena involving entangled photon pairs, such as the Hong-Ou-Mandel interferometer. Although existing theories have been used successfully to theoretically address several important observations involving the SPDC state, the issue of quantitative scale had remained a seldom addressed topic in the field (Byer and Harris, 1968; Shoji *et al.*, 1997), and a formal derivation of the results from modern quantum optical theory had not been presented.

Among the possibilities for future work in this area, the calculation of higher orders in the Dyson series with similar generality remains a most important issue, and could find direct application in experiments using pulsed lasers.

Chapter 3. Theory of time-frequency entangled photon pair recombination

In the quantum optical process of photon pair up-conversion, the recombination of a time-frequency entangled photon pair implies the creation of a single photon in a mode that was initially in the vacuum state. In this chapter, we present a quantum optical theory of the recombination of entangled photon pairs in the regime where recombination events produced by members of different pairs may be neglected. We use this theory to calculate the quantum state of up-converted light generated in a nonlinear crystal of properties identical to that in which the photon pairs were generated. The output of this process will be shown to interfere coherently, in the second-order amplitude sense, with the original pump that generated the down-conversion.

This analysis is focused on the first-order coherence properties of the up-converted field. The incident two-photon state is considered to be, up to a frequency-dependent phase factor, that which was created in the down-conversion crystal, and the linear optical system that is used to approximate this condition is discussed. In contrast to coincidence detection experiments, the phase which the two-photon state acquires as a consequence of material dispersion plays an important role here; this is because efficient recombination requires that the combinations of signal-idler optical paths are not only spatially overlapped, but also time-synchronized over the bandwidth of the incident down-converted pairs within the recombination crystal.

The up-conversion process, as we shall see, is the time-reversed analogue to SPDC and some of the methods used here are similar in nature to those that have been used in Chapter 2; this derivation, however, is presented in full detail as it requires some unique considerations. We shall employ some of the results and equations from Chapter 2, although we will redefine, for clarity, $\Delta\mathbf{k} \rightarrow \Delta\mathbf{k}^d$ as the wave-vector mismatch in the down-conversion crystal, and we introduce the analogous quantity for the up-conversion crystal as $\Delta\mathbf{k}^u$. Throughout the analysis, it is assumed that the refractive indices of the down-conversion and recombination crystals are identical, which requires identical crystal temperatures. In practice, the small differences in the bulk properties of the two crystals used to produce the down-conversion and recombination may require that the temperatures be very slightly different to maximize the output rate.

3.1 The role of dispersion in photon pair recombination

The linear-optical aspect of the propagation of the photon pairs produces in general a transformation of the two-photon state of Eq. 42 that accounts for both the spatial and temporal effects that are produced by the optical system that is used to manipulate the two-photon amplitude. Nevertheless, using a suitably prepared optical system, it is possible to produce a close approximation of the state that is generated in the down-conversion crystal within a second crystal of identical linear optical properties. To preserve the form of the two-photon input state that will be formed in the second crystal, it is necessary to carefully consider and compensate for the temporal dispersion that the members of a photon pair will experience in their propagation over the full bandwidth that we wish to recombine, as has been pointed out in the literature (Dayan *et al.*, 2005; Peer *et al.*, 2005; Gunther, Aimee Kirsten, 2018).

The reason dispersion analysis is important in recombination, despite the fact that the experiments may be performed in the CW regime, is a consequence of the form of the two-photon state of Eq. 25. Such a state represents a continuous linear superposition of signal and idler modes, which implies that each photon pair is created in a broadband *coherent* superposition of mode pairs and propagates with a broad range of frequency pairs and combinations of emission-angles. Thus, all of the possible ways a pair of signal and idler photons may propagate into the recombination crystal are associated with a probability amplitude that contributes coherently to the outcome. The frequency superposition creates the time-energy entanglement that is observed as a strict correlation in the creation time for the signal and idler members of a photon pair; desynchronization translates to phase differences in the different components of the two-photon amplitude which leads to negligible recombination rates due to destructive interference in the up-converted amplitude. An important factor to consider is the dispersion produced by the propagation within the nonlinear crystals themselves; for example, the portion of two-photon amplitude generated at the entrance face of the crystal propagates through more of the material than the portion generated in the center.

3.2 The incident two-photon state

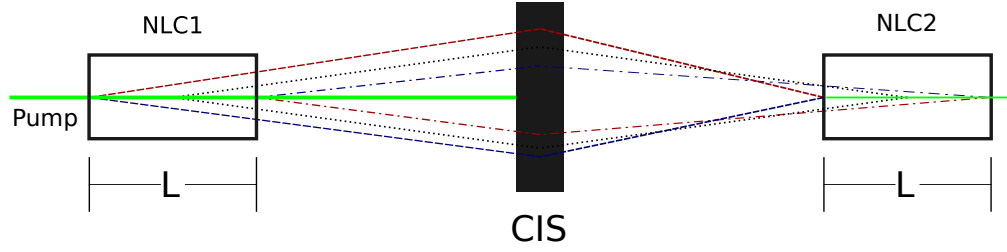


Figure 1. Dispersion-compensated imaging system (CIS) with unit magnification that couples the infrared photon pairs produced in the non-linear crystal NLC1 into an identically-prepared crystal NLC2. The system also removes the pump light.

Figure 1 is a depiction of a dispersion-compensated, unit-magnification optical imaging system (CIS) that may be used to image the interaction volume of the downconversion crystal (NLC1) into the recombination crystal (NLC2). In such a system, any paraxial optical path of a signal photon can be propagated from an arbitrary point in the down-conversion crystal to the corresponding focal point in the up-conversion crystal while traversing a length L of the crystal material, to first order in θ_s . This property of the unit magnification system plays a crucial for recombination; so long as both crystals are made of the same material and have the same length, the temporal dispersion of the photon pairs produced throughout the crystal volume is constant from the point of generation to recombination, and an efficient interaction can be achieved. Compensation of the group delay dispersion, frequently the most important term to consider, is most commonly achieved with methods such as are used to produce ultrashort laser pulses (Died and Rudolph, 2006).

With the previous considerations, we may take the initial state $|\text{in}\rangle$ within the NLC2 crystal as

$$|\text{in}\rangle = \left[\hat{I} - \int_{\mathcal{D}} d\mathbf{k}_s \int_{\mathcal{D}} d\mathbf{k}_i \psi(\mathbf{k}_s, \mathbf{k}_i) e^{i[\varphi(\mathbf{k}_s) + \varphi(\mathbf{k}_i)]} \hat{a}^\dagger(\mathbf{k}_s) \hat{a}^\dagger(\mathbf{k}_i) \right] |\text{vac}\rangle, \quad (51)$$

where \hat{I} is the identity operator. The state of Eq. 51 is the direct product of the state $|\text{vac}\rangle_p$ with a normalized two-photon state similar to that of Eq. 42, which includes the phase terms $\varphi(\mathbf{k}_s)$ and $\varphi(\mathbf{k}_i)$ that represent, respectively, the wave-vector-dependent phase acquired by the signal and idler photons in their propagation from a source point in the down-conversion crystal to the focal point in the recombination crystal, and we have that the integration domain for the signal and idler variables is limited in both

cases to the same set of wave-vectors \mathcal{D} . The two-photon amplitude $\psi(\mathbf{k}_s, \mathbf{k}_i)$ is given by Eq. 26.

3.3 Temporal evolution and commutation relations

To first order in perturbation theory, the quantum state of up-converted light is given by

$$|\text{out}\rangle = \left[\hat{I} - \frac{i}{\hbar} \int_{-\infty}^{\infty} dt \hat{H}_{\text{int}}(t) \right] |\text{in}\rangle, \quad (52)$$

where $\hat{H}_{\text{int}}(t)$ is the interaction Hamiltonian of Eq. 10. The relevant term of the Hamiltonian is that which was written as a Hermitian conjugate in Eq. 10, since the term associated with down-conversion produces the state with zero norm after evaluating its action on our input state. Substituting the Hamiltonian of Eq. 10 and the input state of Eq. 51 we reach the following intermediate result

$$\begin{aligned} |\text{out}\rangle = & \left[\hat{I} - \int d\mathbf{k}_s \int d\mathbf{k}_i \psi(\mathbf{k}_s, \mathbf{k}_i) e^{i[\varphi(\mathbf{k}_s) + \varphi(\mathbf{k}_i)]} \hat{a}^\dagger(\mathbf{k}_s) \hat{a}^\dagger(\mathbf{k}_i) \right. \\ & + \sqrt{\frac{4d_{\text{eff}}^2 \hbar}{(16\pi^3)^3 \epsilon_0 c^3}} \int_{-\infty}^{\infty} dt \int_V d\mathbf{r} \int d\mathbf{k}_p \int d\mathbf{k}_s \int d\mathbf{k}_i \int d\mathbf{k}'_s \int d\mathbf{k}'_i \\ & \times \sqrt{\frac{\omega_p \omega_s \omega_i}{n_p n_s n_i \eta_p \eta_s \eta_i}} \psi(\mathbf{k}'_s, \mathbf{k}'_i) e^{i[\varphi(\mathbf{k}'_s) + \varphi(\mathbf{k}'_i)]} e^{i(\omega_p - \omega_s - \omega_i)t} e^{-i\Delta\mathbf{k}^u \cdot \mathbf{r}} \\ & \times \hat{a}^\dagger(\mathbf{k}_p) \hat{a}(\mathbf{k}_s) \hat{a}^\dagger(\mathbf{k}'_s) \hat{a}(\mathbf{k}_i) \hat{a}^\dagger(\mathbf{k}'_i) \Big] |\text{vac}\rangle, \end{aligned} \quad (53)$$

where $\Delta\mathbf{k}^u = \mathbf{k}_p - \mathbf{k}_s - \mathbf{k}_i - \mathbf{k}_g$ is the wave-vector mismatch in the up-conversion crystal and V is the crystal volume. The three terms in the square brackets of Eq. 53 are, respectively, the vacuum term, the two-photon term, and the recombination term which we will now simplify. The temporal integration in the recombination term can be performed immediately with

$$\int_{-\infty}^{\infty} dt e^{i(\omega_p - \omega_s - \omega_i)t} = 2\pi\delta(\omega_p - \omega_s - \omega_i), \quad (54)$$

while the spatial integration is performed assuming lateral crystal dimensions are much larger than the signal and idler spatial domains, which yields

$$\int_{-\infty}^{\infty} dx \int_{-\infty}^{\infty} dy \int_{-L/2}^{L/2} dz e^{-i\Delta \mathbf{k}^u \cdot \mathbf{r}} = (2\pi)^2 L \delta(\Delta k_x^u) \delta(\Delta k_y^u) s^*(\Delta k_z^u), \quad (55)$$

where $s(\Delta k_z)$ is defined by Eq. 19. We rewrite the commutation relation of Eq. 28 as $\hat{a}(\mathbf{k}_s) \hat{a}^\dagger(\mathbf{k}'_s) = \delta(\mathbf{k}_s - \mathbf{k}'_s) + \hat{a}^\dagger(\mathbf{k}'_s) \hat{a}(\mathbf{k}_s)$ which, after being substituted into Eq. 53 along with an identical expression for the idler variables, allows performing the integrations on the primed variables by virtue of the delta functions that are introduced. The term of form $\hat{a}^\dagger(\mathbf{k}'_s) \hat{a}(\mathbf{k}_s)$ (and the corresponding idler term) that is introduced by using the commutation relation produces a null contribution to the output state, thus being inconsequential in this case.

3.4 Quantum state of up-converted light

After removing the two-photon term from Eq. 53, which is of no further interest for our purposes, the state $|\text{out}\rangle$ represents solely the state of up-converted light and is now denoted by $|\psi_u\rangle$. This state may be written as

$$\begin{aligned} |\psi_u\rangle = & \left\{ \hat{I} - \frac{\sqrt{N_p} d_{\text{eff}}^2 L^2 \hbar}{16 \pi^3 \epsilon_0 c^3} \int d\mathbf{k}_p \int_{\mathcal{D}_{si}} d\mathbf{k}_s \int_{\mathcal{D}_{si}} d\mathbf{k}_i \left[\frac{\omega_s \omega_i}{n_s n_i \eta_s \eta_i} \right] \right. \\ & \times \left[\frac{\omega_p (\omega_s + \omega_i) \eta_p^+}{n_p^+ n_p \eta_p} \right]^{\frac{1}{2}} \frac{\psi_p(\mathbf{k}_p^+)}{\cos \theta_p^0} s(\Delta k_z^d) s^*(\Delta k_z^u) \delta(\Delta k_x^u) \delta(\Delta k_y^u) \\ & \times \delta(\omega_p - \omega_s - \omega_i) e^{i[\varphi(\mathbf{k}_s) + \varphi(\mathbf{k}_i)]} e^{i\Phi_p} \hat{a}^\dagger(\mathbf{k}_p) \Big\} |\text{vac}\rangle, \end{aligned} \quad (56)$$

where $\Delta \mathcal{D}_{si}$ is the wave-vector domain which is transmitted by the optical system that couples the two crystals. The idler differential in Eq. 56 is now expanded using $d\mathbf{k}_i = d\omega_i d\theta_i d\phi_i k_i^2 \eta_i \sin \theta_i$, which allows us to perform the ω_i integration trivially with the frequency delta function, setting $\omega_i = \omega_p - \omega_s$. The (θ_i, ϕ_i) integrations may then be performed using an identity analogous to Eq. 21, but where we are now required to account for the limits of the integration domain, that for an arbitrary function $f(\theta_i, \phi_i)$,

$$\iint_{\Delta \Omega_{si}} d\theta_i d\phi_i \sin \theta_i f(\theta_i, \phi_i) \delta(\Delta k_x^u) \delta(\Delta k_y^u) = \frac{f(\theta_i^0, \phi_i^0)}{k_i^2 \cos \theta_i^0} D_i(\theta_i^0, \phi_i^0), \quad (57)$$

where $\Delta\Omega_{si}$ is the solid angle implicit in \mathcal{D}_{si} . Here, $D_i(\theta_i^o, \phi_i^o)$ is a discrimination function that is unity if $(\theta_i^o, \phi_i^o) \in \Delta\Omega_{si}$, and zero otherwise, which accounts for the potential aperture occlusion of the idler photon. The angles (θ_i^o, ϕ_i^o) are those that zero the delta function arguments in Eq. 57; it is thus readily shown that they follow from

$$\tan \phi_i^o = \frac{k_p \sin \theta_p \sin \phi_p - k_s \sin \theta_s \sin \phi_s}{k_p \sin \theta_p \cos \phi_p - k_s \sin \theta_s \cos \phi_s}, \quad (58)$$

$$\sin \theta_i^o = \frac{k_p \sin \theta_p \cos \phi_p - k_s \sin \theta_s \cos \phi_s}{k_i \cos \phi_i^o}. \quad (59)$$

After integrating Eq. 56 over θ_i and ϕ_i in this way, the recombined pair state takes the form

$$|\psi_u\rangle = \left[\hat{I} - \sqrt{N_p} \int d\mathbf{k}_p \mathcal{E}(\mathbf{k}_p) \psi_p(\mathbf{k}_p) e^{i\Phi_p} \hat{a}^\dagger(\mathbf{k}_p) \right] |\text{vac}\rangle, \quad (60)$$

with $\mathcal{E}(\mathbf{k}_p)$ given by

$$\begin{aligned} \mathcal{E}(\mathbf{k}_p) = & \beta c^2 \frac{\hbar \omega_p}{n_p \cos \theta_p} \int_{\mathcal{D}_s} d\mathbf{k}_s \left[\frac{\omega_s \omega_i}{n_s n_i \eta_s} \right] \\ & \times \frac{D_i(\theta_i^o, \phi_i^o)}{\cos \theta_i^o} |s(\Delta k_z)|^2 e^{i[\varphi(\mathbf{k}_s) + \varphi(\mathbf{k}_i)]}, \end{aligned} \quad (61)$$

where $\beta = \frac{d_{\text{eff}}^2 L^2}{16\pi^3 \epsilon_0 c^5}$, $\mathbf{k}_i = \mathbf{k}_p - \mathbf{k}_s$ is the idler wave-vector with frequency ω_i and angles (θ_i^o, ϕ_i^o) , and where Eqs. 23-22 and Eqs. 58-59 have been used to establish that $\mathbf{k}_p = \mathbf{k}_p^+$, and thus $\Delta \mathbf{k}^u = \Delta \mathbf{k}^d \equiv \Delta \mathbf{k}$.

Equations 60 and 61 may be considered the main results of this chapter, as they can be used to derive all of the information that is experimentally available using the up-converted field of light. The up-converted state of Eq. 60 is the coherent superposition of a vacuum state and a single photon state, which resembles the form of the attenuated pump state presented in Eq. 9. The function $\mathcal{E}(\mathbf{k}_p)$ is then an attenuation factor, which we refer to as the dimensionless amplitude transfer function, which is found to be dependent on the properties of both the nonlinear crystals, as well as the system which couples the photon pairs from the down-conversion crystal into the recombination crystal. Note that both the magnitude and the relative phase of the amplitude transfer function among the \mathbf{k} -space domain of the pump amplitude $\psi_p(\mathbf{k}_p)$ are of interest in Eq. 60. The form of our amplitude transfer function $\mathcal{E}(\mathbf{k}_p)$ of Eq. 61 resembles the rate of pair detection R_π of Eq. 38 yet, despite having nearly identical functional

forms, there is a subtle difference between them which stems from the physical meaning of the $\Delta\Omega_s$ and $\Delta\Omega_i$ domains of detection, considered to be non-overlapping, and the $\Delta\Omega_{si}$ domain of transmission which is the same for signal and idler photons and thus overlaps. This difference manifests in the photon pairs for which both the signal and idler wave-vectors lie on the same side of the optical axis, which do not contribute to pair detection when the detectors used are not photon-number resolving, but contribute to the up-conversion process and have been observed to cause interference effects in experiments (O'Donnell and Garces, 2015).

It is remarkable that the complete down-conversion-up-conversion process may be described in terms of the transfer function $\mathcal{E}(\mathbf{k}_p)$, which is linear in the pump amplitude. This simple description can be readily adapted to reflect more advanced experimental conditions beyond the elementary situation here considered. For example, introducing a time delay between the members of a signal-idler pair requires only that we account for the phase acquired by the delayed photon in its propagation; as we shall see, this allows us to theoretically explore the coherence properties of the down-converted field at the femtosecond-scale. Similarly, optical aberrations and imperfect dispersion cancellation can be considered, as well as other experimentally-significant features such as the effects of the limiting aperture for the photon-pair coupling system. In the rest of this chapter, we shall first describe the fundamental coherence properties of the up-converted field, and will later evaluate the amplitude transfer function for some currently-relevant configurations. Additionally, we will consider that the phase term $\varphi(\mathbf{k}_\epsilon)$ is only a function of the frequency $\omega_\epsilon = c|\mathbf{k}|/n_\epsilon$ and not of the angles $(\theta_\epsilon, \phi_\epsilon)$ (for $\epsilon \in \{s, i\}$), so that it will be called a chirp term and will be denoted as $\varphi(\omega_\epsilon)$.

3.5 Coherence functions and the up-converted photon rate

The up-converted state of Eq. 60 provides us with a complete description for the up-converted modes of the quantized electromagnetic field at the output of the recombination crystal. All of the experimentally-available characteristics of this field may be computed as the expectation of the relevant field-theory operators in the state $|\psi_u\rangle$ (Glauber, 1963b). We will now employ this result to determine the self-coherence function of the up-converted state $|\psi_u\rangle$ and the mutual coherence function of this state with an attenuated version of the pump $|\psi_p\rangle$. These calculations will provide important insights into the properties of the up-converted state, such as the fringe visibility that may be experimentally observed by interference of the up-converted and pump fields, as well as the up-converted photon rate.

3.5.1 Self-coherence function, up-converted photon rate, and the normalized coherence function

The association of the two-field coherence function with the first-order coherence properties of the field modes used here is well established (Glauber, 1963b), and has been employed for continuum fields in studies of down-conversion (Joobeur *et al.*, 1994). For a stationary state $|\psi_\alpha\rangle$, we define the second-order self-coherence function as

$$G_\alpha^{(1)}(\mathbf{k}, \mathbf{k}'|\tau) = \langle \psi_\alpha | \hat{a}^\dagger(\mathbf{k}) \hat{a}(\mathbf{k}') | \psi_\alpha \rangle e^{-i\omega'\tau}, \quad (62)$$

where the plane wave mode with wave-vector \mathbf{k}' has a time delay τ relative to the mode with wave-vector \mathbf{k} , and $\omega' = c|\mathbf{k}'|/n_\alpha$. Evaluating Eq. 62 for the up-converted state of Eq. 60 yields

$$G_u^{(1)}(\mathbf{k}, \mathbf{k}'|\tau) = N_p \mathcal{E}^*(\mathbf{k}) \psi_p^*(\mathbf{k}) e^{-i\Phi_p} \mathcal{E}(\mathbf{k}') \psi_p(\mathbf{k}') e^{i\Phi_p} e^{-i\omega'\tau}. \quad (63)$$

When evaluated at $\mathbf{k} = \mathbf{k}'$, and $\tau = 0$, Eq. 63 is simply the up-converted photon number density in wave-vector space; the wave-vector integral in Eq. 63 over a finite domain is then the expectation for the up-converted photon number. Finally, dividing

this photon number number by the time Δt yields the up-converted rate

$$\begin{aligned} R_u &= \frac{1}{\Delta t} \int d\mathbf{k}_p G_u^{(1)}(\mathbf{k}_p, \mathbf{k}_p|0) \\ &= R_p \int d\mathbf{k}_p |\mathcal{E}(\mathbf{k}_p) \psi_p(\mathbf{k}_p) e^{i\Phi_p}|^2, \end{aligned} \quad (64)$$

and the up-conversion efficiency is then $\mathcal{R}_u = R_u/R_p$. In the limiting case where $\mathcal{E}(\mathbf{k}_p) \approx \mathcal{E}(\mathbf{k}_p^o)$ may be considered constant within the domain of the pump amplitude ψ_p , the up-conversion efficiency is reduced to $\mathcal{H}_u = |\mathcal{E}(\mathbf{k}_p^o)|^2$. The values of $G_u^{(1)}(\mathbf{k}, \mathbf{k}'|\tau)$ having nonzero τ and distinct wavevectors are also of importance; these determine the general spatiotemporal coherence properties of the state which can be detected interferometrically through superposition of different portions of the up-converted field.

As it is most convenient to discuss coherence in normalized terms, we shall introduce the normalized self-coherence function, which is defined as (Joobeur *et al.*, 1996).

$$g_u^{(1)}(\mathbf{k}, \mathbf{k}'|\tau) = \frac{G_u^{(1)}(\mathbf{k}, \mathbf{k}'|\tau)}{\sqrt{G_u^{(1)}(\mathbf{k}, \mathbf{k}|0) G_u^{(1)}(\mathbf{k}', \mathbf{k}'|\tau)}}. \quad (65)$$

Using Eqs. 63 and 65, it is trivial to verify that $|g_u^{(1)}(\mathbf{k}, \mathbf{k}|\tau)| = 1$, which implies that the up-converted field has perfect spatial and spectral first-order self-coherence, so that different wave-vector components of the up-converted state can interfere with unit visibility when superposed.

3.5.2 Mutual coherence of the pump and up-converted light

We now consider the product state $|\psi_{p \otimes u}\rangle = |\{\psi_p\}\rangle |\psi_u\rangle$, where we assume the Hilbert subspaces of the pump and up-converted states are non-overlapping. Due to the extremely large difference in the pump and up-converted photon rates, the visibility of the interference in direct superposition of these fields would be vanishingly small. To observe significant effects in the interference between the pump and up-converted field, it is necessary to attenuate the pump state to a level that is similar to that of the up-converted state. Thus, we consider the up-converted state of Eq. 60 along with the pump state of Eq. 9, with $\gamma \sim \mathcal{E}(\mathbf{k}_p)$ for \mathbf{k}_p in the domain of $\psi_p(\mathbf{k}_p)$, and

write the product state as

$$|\psi_{p\otimes u}\rangle = \{\hat{I} + \hat{\rho}^\dagger + \hat{u}^\dagger\} |\text{vac}\rangle_p |\text{vac}\rangle_u, \quad (66)$$

where $\hat{\rho}^\dagger$ is the second term in Eq. 9, \hat{u}^\dagger is the second term in Eq. 60, and we have ignored the nearly unitary normalization constant M_p along with a small term proportional to $\hat{u}^\dagger \hat{\rho}^\dagger$ corresponding to one photon in each mode. We define the mutual coherence function for the product state as

$$\begin{aligned} G_{pu}^{(1)}(\mathbf{k}_p, \mathbf{k}_u|\tau) &= \langle \psi_{p\otimes u} | \hat{a}^\dagger(\mathbf{k}_p) \hat{a}(\mathbf{k}_u) | \psi_{p\otimes u} \rangle e^{-i\omega_u \tau} \\ &= e^{i\pi} \gamma^* \psi_p^*(\mathbf{k}_p) \mathcal{E}(\mathbf{k}_u) \psi_p(\mathbf{k}_u) e^{-i\omega_u \tau}. \end{aligned} \quad (67)$$

where τ is the a relative time delay. The normalized mutual coherence function is then defined as

$$g_{pu}^{(1)}(\mathbf{k}_p, \mathbf{k}_u|\tau) = \frac{G_{pu}^{(1)}(\mathbf{k}_p, \mathbf{k}_u|\tau)}{\sqrt{G_p^{(1)}(\mathbf{k}_p, \mathbf{k}_p|0) G_u^{(1)}(\mathbf{k}_u, \mathbf{k}_u|\tau)}}, \quad (68)$$

from which it is simple to show that, in the small-efficiency limit (viz. where $\gamma^2 \ll 1$)

$$|g_{pu}^{(1)}(\mathbf{k}_p, \mathbf{k}_u|\tau)| = 1 \quad (69)$$

which implies that perfect visibility can be obtained in the interference of the up-converted and attenuated pump states.

Our analysis here neglects the effects of losses, which are experimentally inevitable; however, it has been established that the two-photon part of the down-converted state retains a pure state description even when losses are introduced into the Hamiltonian (Helt *et al.*, 2015; Helt and Steel, 2015). With the up-converted state consequently being the pure state, it is thus expected that the pump/up-conversion interference fringes will be temporally stable, as has been experimentally demonstrated (Jimenez *et al.*, 2019). It is clear that, whenever the incident down-converted field may be described adequately by a photon pair state of the form of Eq. 51, the up-converted light will accept a single-photon description such as is given by 60.

With this, we have demonstrated that the up-conversion of entangled photon-pairs is an entirely quantum optical phenomenon that represents a detectable consequence of the spatio-temporal entanglement of the photon pairs in the SPDC state, and which allows the recombined photon to remain fully coherent with the original pump.

3.5.3 Single-frequency pump limit

We will now discuss in detail the up-converted rate for the limiting case of a single-frequency pump. The up-converted rate of Eq. 64, along with the dimensionless transfer function $\mathcal{E}(\mathbf{k}_p)$, are written in terms of the frequency and angular variables ω_p , θ_p , and ϕ_p by expanding the pump wave-vector differential using

$$d\mathbf{k}_p = d\omega_p d\theta_p d\phi_p k_p^2 \eta_p \sin \theta_p, \quad (70)$$

and substituting Eq. 5 for the pump amplitude $\psi_p(\mathbf{k}_p)$. Then, we take the narrowband limit $|\mathcal{A}(\omega_p)|^2 \rightarrow \delta(\omega_p - \omega_p^o)$ and perform the ω_p integration, with the result that

$$R_u = R_p \iint d\theta_p d\phi_p \sin \theta_p \left| \mathcal{E}_{\omega_p^o}(\theta_p, \phi_p) \mathcal{F}(\theta_p, \phi_p | \omega_p^o) e^{i\Phi_p} \right|^2, \quad (71)$$

where, now with $\omega_i = \omega_p^o - \omega_s$,

$$\begin{aligned} \mathcal{E}_{\omega_p^o}(\theta_p, \phi_p) &= \beta \frac{\hbar \omega_p^o}{n_p \cos \theta_p} \int d\omega_s \frac{n_s \omega_s^3 \omega_i}{n_i} e^{i[\varphi(\omega_s) + \varphi(\omega_i)]} \\ &\times \iint_{\Delta\Omega_{si}} d\theta_s d\phi_s \frac{\sin \theta_s}{\cos \theta_i^o} D_i(\theta_i^o, \phi_i^o) |s(\Delta k_z)|^2. \end{aligned} \quad (72)$$

From the form of Eq. 71, and through its comparison with Eq. 8, we identify $\mathcal{E}_{\omega_p^o}(\theta_p, \phi_p)$ as the angular modal transfer function for a single-frequency pump. This is the transfer function relevant to the recent CW up-conversion experiments (O'Donnell and U'Ren, 2009; O'Donnell, 2011; Jimenez *et al.*, 2019) and may be regarded as a simplification of $\mathcal{E}(\mathbf{k}_p)$ from Eq. 61. We emphasize that, in this formulation, the single-frequency limit is taken in accordance with the normalization condition of Eq. 7 in the calculation of the rates, as opposed to the more usual, though non-normalizable, consideration of taking the amplitude itself as approaching a delta function, i.e. $\mathcal{A}(\omega_p) \rightarrow \delta(\omega_p - \omega_p^o)$, which results in spurious terms of the form $\delta^2(\omega_p - \omega_p^o)$ that have been a source of error

in the dimensions of existing formulations and can not be defined within distribution theory. In the important case when, after exiting the first crystal, the SPDC is limited by a circular aperture to a cone of angular radius $\tilde{\theta}_c$, Eq. 72 simplifies to

$$\mathcal{E}_{\omega_p^o}(\theta_p, \phi_p) = \beta \frac{\hbar \omega_p^o}{n_p \cos \theta_p} \int_{\Delta \omega_s} d\omega_s S(\omega_s) e^{i[\varphi(\omega_s) + \varphi(\omega_i)]}, \quad (73)$$

where the integration is taken over the relevant positive frequency bandwidth,

$$S(\omega_s) = \frac{n_s \omega_s^3 \omega_i}{n_i} \int_0^{\Theta_s} d\theta_s \int_0^{2\pi} d\phi_s \frac{\sin \theta_s}{\cos \theta_i^o} D_i(\theta_i^o) |s(\Delta k_z)|^2, \quad (74)$$

and $\Theta_s = \arcsin[\sin \tilde{\theta}_c / n_s]$ is the angular limit within the crystal. Here, $D_i(\theta_i^o) = D_i(\theta_i^o, \phi_i^o)$ represents the circular limiting aperture in idler variables which is now independent of ϕ_s . In particular, $D_i(\theta_i^o)$ is zero if $\theta_i^o > \Theta_i \equiv \arcsin[\sin \tilde{\theta}_c / n_i]$, and unity otherwise. It is also notable that the pump angles (θ_p, ϕ_p) are not seen in $S(\omega_s)$ in Eq. 74, but they enter implicitly through (θ_i^o, ϕ_i^o) from Eqs. 58-59.

For a circular limiting aperture, the angular transfer function is independent of ϕ_p , so we may write simply $\mathcal{E}(\theta_p) = \mathcal{E}(\theta_p, \phi_p)$. In order to easily introduce the effects of dispersion, it can be useful to transform the integration variable in Equation 73 from ω_s to $\Delta\omega = \omega_s - \omega_d$, so that

$$\mathcal{E}_{\omega_p^o}(\theta_p) = \beta \frac{\hbar \omega_p^o}{n_p \cos \theta_p} \int d\Delta\omega S(\omega_d + \Delta\omega) e^{i[\varphi(\omega_s + \Delta\omega) + \varphi(\omega_i - \Delta\omega)]} \quad (75)$$

Using arguments similar to those of the Appendix, it is possible to show that the positive and negative portions of the $\Delta\omega$ integration domain represent an exactly equal number of photons; this property can be useful when performing numerical and analytical computations, as the discriminator function $D_i(\theta_i)$ may be neglected within the $S(\omega_d + \Delta\omega)$ for $\Delta\omega < 0$.

3.5.4 Wide-beam pump limit

Finally, we consider the further limit of a pump beam that is quite wide at the crystal and propagates along the optical axis. This limit is properly taken in Eq. 71 as $|\mathcal{F}(\theta_p, \phi_p|\omega_p^o)|^2 \rightarrow k_p^2 \delta(k_p \sin \theta_p \cos \phi_p) \delta(k_p \sin \theta_p \sin \phi_p)$, and for the case of perfect dispersion compensation yields

$$R_u = R_p |\mathcal{E}_{\omega_p^o}^{\text{WP}} e^{i\Phi_p}|^2, \quad (76)$$

where

$$\begin{aligned} \mathcal{E}_{\omega_p^o}^{\text{WP}} &= \beta \frac{\hbar \omega_p^o}{n_p} \int d\omega_s \frac{n_s \omega_s^3 \omega_i}{n_i} \\ &\times \iint_{\Delta\Omega_{si}} d\theta_s d\phi_s \frac{\sin \theta_s}{\cos \theta_i^o} \mathcal{D}_i(\theta_i^o) |s(\Delta k_z)|^2. \end{aligned} \quad (77)$$

In Eq. 77, the idler angles are to be evaluated at $\theta_p=0$, which follow from Eqs. 58-59 as $(\theta_i^o, \phi_i^o) = (\arcsin[\frac{n_s \omega_s}{n_i \omega_i} \sin \theta_s], \phi_s - \pi)$. Further, it is also clear that $\mathcal{E}_{\omega_p^o}^{\text{WP}} = \mathcal{E}_{\omega_p^o}(\theta_p, \phi_p)|_{\theta_p=0} = \mathcal{E}(\mathbf{k}_p^o)$, where \mathbf{k}_p^o is the axial wave-vector with frequency ω_p^o .

At this point, upon comparing the up-converted rate of Eq. 76 and the signal rate of Eq. 39 we see that they are both formulated using similar integrals, and both depend in a linear manner on the pump photon rate R_p , yet we can also see two key differences. The first of those differences is that the upconverted rate R_u depends on the square of the integrals that determine the efficiency, and the second is the presence of the idler photon angular discriminator function $\mathcal{D}_i(\theta_i^o)$ in Eq. 77. Two consequences of this observation are that the total emitted pair rate over a circularly symmetric aperture may be calculated as $R_\pi = \mathcal{E}_{\omega_p^o}^{\text{WP}}$, and that, under the experimental conditions here discussed, the efficiencies of the down-conversion and up-conversion processes are identical. This similarity, however, must not be interpreted as meaning that coincidence pair detection and up-conversion provides identical insights of the down-converted field; a critical difference between these two processes is that the up-conversion process is, in general, sensitive to the phase (including the chirp) present in the two-photon state, and can thus be used to directly probe the complex-valued two-photon amplitude.

3.5.5 Time-delayed up-converted rate

The simplifications afforded by taking the limit of a wide-beam pump opens the path to a calculation method that is perfectly suited for evaluation of time-delayed up-conversion experiments, where the spatial dependence of the up-converted state can be ignored. The up-converted photon rate observed with a signal-idler time-delay of τ is calculated in a manner analogue to Eq. 64 as

$$\begin{aligned} R_u(\tau) &= \frac{1}{\Delta t} \int d\mathbf{k}_p G_u^{(1)}(\mathbf{k}_p, \mathbf{k}_p | \tau) \\ &= R_p |\mathcal{E}_o(\tau)|^2, \end{aligned} \quad (78)$$

which follows from Eq. 71 and where we have used the amplitude transfer efficiency $\mathcal{E}_{\omega_p^o}^{\text{WP}}$ has been renamed to $\mathcal{E}_o(\tau)$ and is now given by

$$\mathcal{E}_o(\tau) = \beta \frac{\hbar \omega_p^o}{n_p} \int_0^\infty d\omega_s S(\omega_s) e^{i\omega_s \tau} e^{i[\varphi(\omega_s) + \varphi(\omega_i)]}, \quad (79)$$

where it is understood that $S(\omega_s)$ is to be evaluated with $\theta_p = 0$ in Eq. (74). Thus $\mathcal{E}_o(\tau)$ can be nearly the Fourier transform of $S(\omega_s)$, depending on the significance of the chirp phase terms. Although the notion of arbitrarily delaying all signal photons compared to their respective idlers may strictly appear possible only within *Gedanken-experiments*, within the wide-pump limit this situation is indeed equivalent to the experimentally-available situation where one half of the emission cone is delayed with respect to the other; this is due to two reasons: first of all, because of the symmetry that exists between the signal and idler variables, which is discussed in the Appendix, and moreover because of the geometrical consequence of the wide-pump limit on the emission angles, which guarantees that the two-photon amplitude will be non-zero only for combinations of signal and idler variables which are on opposite sides of the optical axis and that they all contribute to the same axial up-converted amplitude.

Time-delayed photon pair recombination experiments can attain ultra-sharp temporal resolution, which is essentially limited only by the dispersion-compensated bandwidth that is able to recombine in the second crystal, and in principle can be close the optical period of the pump (Harris and Sensarn, 2007). Attaining larger up-conversion efficiencies remains a challenging issue, one which may require the development of

improved methods for dispersion compensation to increase the effective up-conversion bandwidth.

To close this chapter we emphasize that, within this work, every possible effort has been made to keep the theoretical approach to photon pair recombination as general as possible and represents a complete description of the entangled photon pair up-conversion process in the spontaneous regime. Evaluations of these expressions may be applied to study the dependence of the recombination rates on parameters such as pump wavelength and bandwidth, crystal temperature, and phase aberrations of the optical system. More fundamentally, the process of entangled photon pair recombination may be used to probe the phase and temporal properties of the two-photon amplitude itself, providing information well beyond the capabilities of common techniques such as coincident pair detection.

Chapter 4. Measurements and calculations of the entangled photon pairs generated in periodically-poled KTP crystals

In this chapter, we present an experimental study of the degenerate and non-degenerate, non-collinear down-converted light produced by SPDC in periodically-poled KTP nonlinear crystals. A comparison of the observations with calculations from the theory is also presented for the observations relating to the angular and crystal temperature dependence of the detected photon pair rate. Two optical pump systems were implemented and crystals with two different design periodicities were used and characterized.

The entangled photon pairs were detected through coincidence detection using a pair of single-photon detectors. The dependence of correlated emission on crystal temperature is examined in detail through both narrowband and broadband observations. The dependence of the rate of coincident photon pairs as a function of detection angle and filter frequency is also studied experimentally under a broad range of conditions. The system has shown to be capable of detecting frequency degenerate and non-degenerate photon pairs with a large dynamic range for pair rates, ranging from under 1 pair per second to over one hundred thousand pairs per second. In addition, we also present a set of measurements using the down-converted light which relate to the characterization of the transverse homogeneity of our periodically-poled KTP crystals which are used to generate the emission. The experimental arrangement built for this work includes the optical system for the production and detection of the entangled photon pairs, as well as the electronic and logical systems for the control, monitoring, and data logging of our experiments. In addition to the experimental arrangement, the observations also rely on practices and procedures that follow from theoretical considerations, and an attempt is made to comment upon these aspects where it is relevant.

4.1 Experimental arrangements

The experimental setup is shown in Fig. 2, where it is possible to pump the PPKTP crystal with either of two narrow-band laser systems, LS1 and LS2, with relative ease.

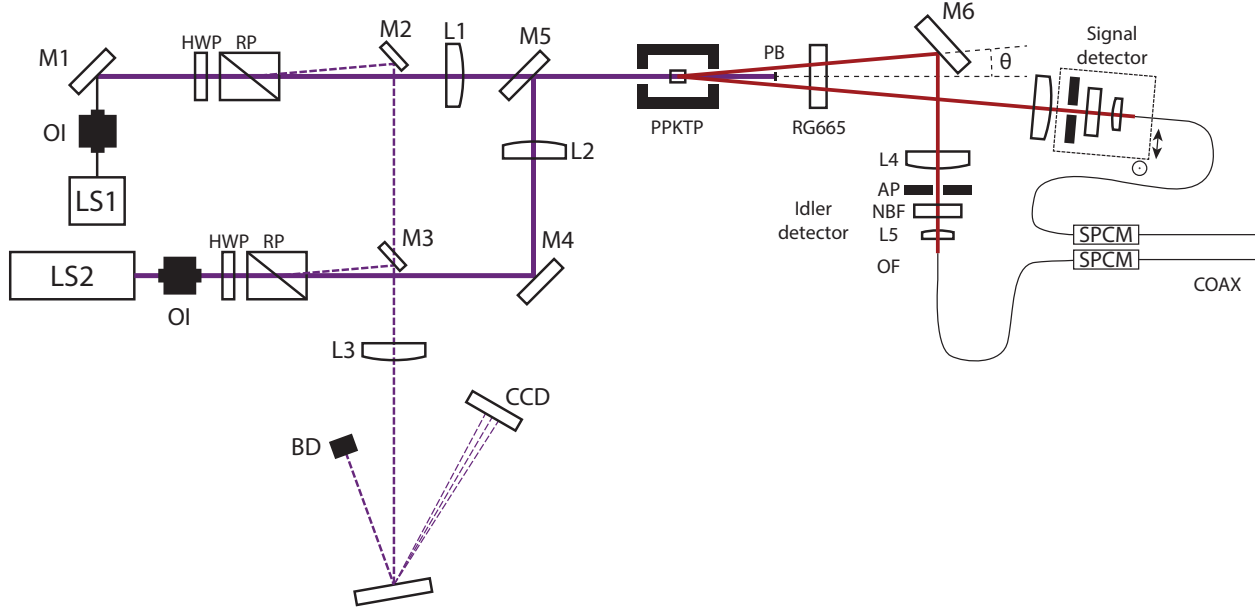


Figure 2. Experimental diagram. The pump beam from either the LS1 or LS2 laser systems is focused by the L1 or L2 lens, respectively, to form a waist in a PPKTP crystal mounted in an oven after passing through an optical isolator (OI), a half-wave plate (HWP), a Rochon polarizer (RP), and a dielectric mirror (M1 or M4). The exiting light reaches a pump block (PB) and a Schott RG665 infrared filter, and then mirror M2 deflects the idler light downward to a collimating lens (L4), a circular limiting aperture (AP), and a narrowband filter (NBF). Lens L5 then couples the light to a multimode fiber (OF) and detector (SPCM). The signal side is undeflected and has analogous components; the components after its collimating lens are mounted on a two-dimensional translation stage. Mirrors M2 and M3 reflect the light rejected from the polarizer to a lens (L3) and diffraction grating (DG), which casts a spectrum on a CCD. The M5 mirror is attached to a flip mount to select either pump laser system.

4.1.1 Pump laser systems

The laser system LS1 is a wavelength-stabilized laser diode (Ondax SureLock) which produced a nearly circular Gaussian beam of nominal wavelength $\lambda_p \approx 406.1$ nm with single-mode bandwidth of $\Delta\lambda_p \approx 7 \times 10^{-5}$ nm, and a maximum power at the entrance of the crystal of 22 mW. During operation, the temperature and current of the diode is controlled using a Stanford Research Systems laser diode controller (LDC501). The user-adjustable temperature control of the diode has been found to provide a flexible and reliable mechanism to tune the emission wavelength over a range of approximately 0.3 nm, and has also been used to us to produce observations where the laser

is simultaneously emitting in two-frequencies. By locking the laser system into a 'reference' emission line prior to each measurement using a CCD, specifically chosen for its observed stability, we have produced sets of self-consistent observations over a temporal span covering several weeks.

The LS2 laser is an actively stabilized laser diode (Toptica TopMode) which produced a circular Gaussian Beam of nominal wavelength $\lambda_p = 405 \text{ nm}$, a bandwidth of $\Delta\lambda_p < 1 \times 10^{-5} \text{ nm}$, and a maximum power at the entrance of the crystal of 100 mW . The active stabilization control unit of this laser system does not admit any significant level of user adjustment of the operation parameters and may lock into different laser lines on separate occasions, depending on laboratory conditions.

The beams from LS1 and LS2 are focused using lenses L1 and L2 to e^{-1} amplitude radii of $w_o = 95 \mu\text{m}$ and $w_o = 110 \mu\text{m}$, respectively, at the center of the nonlinear crystal. As the confocal parameters of the beams are 140 mm for LS1 and 183 mm for LS2, the transverse amplitude profile of either beam may be considered as constant along length of the crystal to a very good approximation.

Upon selection of the laser system to be used, the optical isolator (OI) and power control (PC) systems are fitted, and the flipping mirror M5 is configured as required. The power control system is composed of a Rochon polarizer RP and a zero-order half-wave plate (at $\lambda = 405 \text{ nm}$) HWP. The introduction of the optical isolator significantly improved the frequency stability of both of our laser systems.

4.1.2 Frequency stability monitoring system

Throughout experiments, the stability of the laser was monitored and logged using the pump light deflected by the Rochon polarizer. This light was reflected from the mirror M2 for LS1 and M3 for LS2, then passed through the lens L3 to a diffraction grating DG, whose second diffracted order was attenuated and focused onto a commercial CCD device with a USB interface. A real-time monitoring and data logging system was implemented; this extracted a line of pixels from the blue channel of the CCD camera, which provided 8 bits of resolution in the intensity scale at 15 Hz .

The spectral resolution of our monitoring system is 50 pm , which is orders of mag-

nitude larger than the laser line-width for either of our systems, but is adequate to resolve the separation between adjacent laser lines and allows us to detect any significant drift. This instrument has proved critical for obtaining self-consistent sets of data, as well as to produce observations with LS1 operating in two-frequency modes with varying wavelength separation. No mode hopping or drifting was observed during the measurements to be presented here.

4.1.3 PPKTP crystals and temperature control

The crystals used in this work were periodically-poled KTP of length 5 mm with a poling period $\Lambda = 3.425 \mu\text{m}$ for crystals of type A, and $\Lambda = 3.375 \mu\text{m}$ for crystal of type B, which provided quasi-phasematching to nearly axial, co-polarized, down-converted broadband light with central wavelength $2\lambda_p$. Specifically, the pump light propagates along the x' crystal axis, where the primed coordinates are understood to refer to the crystal axes which coincides with the table (laboratory) axis z , the crystal axis are such that the $x'z'$ crystal plane is parallel to the optical table, and all fields are linearly polarized with the electric field along the z' crystal axis.

In experiments, the crystal was temperature-controlled so as to adjust the quasi-phasematching conditions through its temperature-dependent refractive index; this is achieved by housing the crystal in an oven, with the resistive heating and feedback being controlled using a ThorLabs TC200 temperature controller. The temperature range of the crystal covers from 30°C up to 180°C . The oven is mounted in an optical mount that allows precise control of the transverse position of the crystal, as well as its orientation, and a dovetail mount is used for coarse adjustment of the longitudinal position.

The poling periodicity of each of our crystals has been designed to produce SPDC with one of our available laser systems within the available temperature range, which is necessary due to the sensitivity of the QPM tuning curves to changes in the pump wavelength. Crystals of type A are well suited to produce observations of SPDC using the laser system LS1 at crystal temperatures from approximately 50°C for the degenerate case and up to 100°C for the non-degenerate case; they may also be used with the LS2 system for degenerate and a limited range of non-degenerate observations at tem-

peratures of 150° and higher. Crystals of type B are used mainly with the LS2 system with temperature ranges from approximately 100°C for degenerate observations and with a broad range of non-degenerate interactions available at larger temperatures. The QPM temperature for collinear and degenerate SPDC, T_{QPM} , is approximately 67°C for crystals of type A, and 109°C for crystals of type B. All measurements shown using crystals of type A are performed with LS1 and, unless otherwise noted, measurements shown with crystals of type B are performed using LS2.

As will be discussed later in more detail, the output produced by crystals of type A was found to be significantly weaker, by approximately two orders of magnitude, than that produced by crystals of type B under comparable conditions. This increased output power observed with our samples of type B appears to be caused by a far better quality of the periodic poling micro-structure, which translates to a drastically improved spatially uniformity of the effective non-linearity compared with our samples of type, and produces a nearly ideal longitudinal QPM function, as we shall show. The comparatively poor quality of our samples of type A precludes quantitative analysis beyond a relative scale in the results obtained with those crystals.

We characterized empirically the correction term \tilde{k} for the longitudinal quasi-phase mismatch in our observation conditions as a function of crystal temperature, using observations from both single-photon detection experiments, and coincidence detection of the entangled photon pairs. These have allowed us to produce tuning curves that compare favorably with the observations.

4.1.4 Pair collection optical system

The nonlinear crystal is followed by a pump block PB and an infrared transmissive filter (RG665 in 2) which transmits the SPDC while preventing the pump from propagating into our pair collection system. Two collimating lenses are placed at 500 mm from the crystal at opposite locations of the down-converted cone; a silver mirror is used in one of the paths, from here on referred to as the idler side, due to limitations of space. The elements that appear on both the signal and idler side are only labeled on the idler side. The lenses are centered at angles of $\theta_{s,i} = 2.16^\circ$ from the optical axis and, for simplicity, we consider that $\phi_s = 0$, when the signal detector is configured

in the plane of the diagram, and $\phi_i = \pi$ for the fixed central detection angle of the idler detector. All of the optical components following the collimating lens in the signal arm are mounted on a two-dimensional translation stage that allows positioning along the transverse plane; the equivalent components on the idler side are mounted on the optical table, detecting a fixed angle of 2.16° .

On either detection arm, the collimated down-conversion is focused using an aspherical lens L5 of with a 5 mm clear aperture, which provides a maximal angular diameter of 0.573° for our observations. The collected light is then coupled into multi-mode optical fibers OF of $50\ \mu\text{m}$ core diameter, and is then allowed to propagate into a pair of single photon counting modules (SPCMs). Except for the observations concerning the temporal response time of the photo-detectors, all of the photon counting measurements shown here have been produced using two Perkin-Elmer SPCM-AQR-13-FC.

Additional components may be fitted into the signal and idler optical paths following the collimating lens. To limit the range of integration angle and optical frequencies incident at the detector, matching sets of limiting apertures AP and filters NBF were used. Angular diameters of $\Delta\theta = 0.086^\circ$ and $\Delta\theta = 0.132^\circ$ were available using our limiting apertures with which we explored, to a good approximation, the limit of negligible angular integration; as we shall see, our pump beam geometry produces correlation cells of angular diameter larger than these apertures in all cases. The characteristics bandpass filters used to produce narrowband observations are found in Table 1; the filters are arranged by pairs, as required by the energy conservation condition.

Table 1. Signal ($\epsilon = s$) and idler ($\epsilon = i$) filters used for detection of three narrowband SPDC interactions, where λ_ϵ is the central transmitted wavelength, $\Delta\lambda_\epsilon$ is the FWHM, and T_ϵ is the transmittance.

Filter pair label	λ_s/λ_i	λ_s [nm]	$\Delta\lambda_s$ [nm]	T_s	λ_i [nm]	$\Delta\lambda_s$ [nm]	T_i
A	1	812.5	19	75%	812.5	19	75%
B	1.07	842	20	79%	782	17	85%
C	1.28	927	10	62%	722	11	36%

4.1.5 Coincidence discrimination, real-time monitoring, and automated data collection

During the course of this work, two different systems were used to perform the coincidence discrimination of the electronic pulses generated by our photon counters. For our initial experiments, such as the determination of the angular and temperature dependence of the pair rate, the coincidence discrimination was performed in hardware using fast logic gates in NIM modules, these have been described elsewhere (see Ref. (Jiménez, 2014)) and operate with a coincidence window of 6 ns. Later experiments were performed using a time-to-digital converter (TDC, Roithner TDC8000) which records the arrival time of each photo-detection event with a resolution of 164 ps; these time-tags are sent via gigabit ethernet to a controlling computer, which performs coincidence discrimination in software using a coincidence window of approximately 1 ns that is adapted as required by detector characteristics.

A computer system was designed, constructed and programmed to perform our measurements. This system provided us with real-time monitoring capabilities for singles, coincidences and accidentals, as well as the logging of the data. The software for the data collection, coincidence processing, and uninterrupted data collection, was developed in the C programming language and runs under a real-time linux kernel. The system can also drive and monitor the TC200 temperature controller, and assist in manual stepping measurements through audio cues. The TDC system can produce up to 80 MB/s of time-tag data under load, which is limited by the gigabit ethernet connection and includes only the information of the singles; the computer system must then be capable of capturing all of the incoming packets as well as process, store, and display the relevant data. A fast solid state drive is used for data storage during the experiment, the data is subsequently transferred to hard disk drive for archival and future processing. Additionally, a usb software driver for the Ocean Optics USB2000 spectrometer was developed.

4.2 Crystal temperature dependence of the pair rate

In this section, we consider the pair rates obtained with the two detectors at fixed angles, while the crystal temperature was scanned using a crystal of type A. In particular, the idler detector was kept at $\theta_i = 2.16^\circ$ and the signal detector was set to the θ_s angle that produces transverse quasi-phasematching for the filter pair that is used. The observations may be more readily understood by considering a simplified version of Eq. 30 of form

$$R_\pi = \mathcal{K} \int_{\mathcal{D}_s} d\mathbf{k}_s \int_{\mathcal{D}_i} d\mathbf{k}_i \left| \sqrt{\omega_s \omega_i} \mathcal{A}(\omega_s + \omega_i) \mathcal{F}(\Delta \mathbf{k}_\perp) s(\Delta k_z) \right|^2, \quad (80)$$

where \mathcal{K} is a proportionality constant; the observations will be compared with pair rate calculations from this expression.

To introduce the discussion of our results, we first consider the geometrical conditions that are required to produce a high pair rate in a simple case, for which we assume that the detection domains \mathcal{D}_s and \mathcal{D}_i are of negligible extent in wave-vector domain, and implies both narrowband detection and small observation angles. Under these conditions, the pair rate is directly proportional to the integrand of Eq. 80, and the condition for maximizing the the pair rate corresponds to those which maximize this integrand. Assuming a narrowband pump, and if the detection bandwidths of the signal and idler detectors are selected in accordance to Eq. 20, $\omega_s + \omega_i = \omega_p$, the pair rate is directly proportional to the product $|\mathcal{F}(\Delta \mathbf{k}_\perp) s(\Delta k_z)|^2$, where the importance of the wave-vector mismatch $\Delta \mathbf{k}$ is immediately apparent. Under typical experimental conditions of a Gaussian beam pumping a bulk or periodically-poled crystal, both the $\mathcal{F}(\Delta \mathbf{k}_\perp)$ and $s(\Delta k_z)$ attain their respective maximum when their argument reaches zero, which correspond to the transverse and longitudinal QPM conditions $\Delta \mathbf{k}_\perp = 0$ and $\Delta k_z = 0$. When the detection occurs in a plane parallel to the optical table such that $\phi_s = 0$ and $\phi_i = \pi$, it follows from $\Delta \mathbf{k}_\perp = 0$ that

$$\frac{\lambda_s}{\lambda_i} = \frac{\sin \theta'_s}{\sin \theta'_i}, \quad (81)$$

where the external signal angle θ'_s is given by Snell's law, $\sin \theta'_s = n_s(\omega_s, T) \sin \theta_s$, with a symmetric condition for θ'_i .

Critically, under our conditions, Eq. 81 is independent of crystal temperature, which is a very useful property for experimental design, as it represents a geometrical condition written in terms of the experimentally available parameters, viz. the signal external angle of detection and the signal and idler detection frequencies. There are conditions, however, in which Eq. 81 does not hold, such as when the nonlinear crystal is tilted so that the poling wave-vector \mathbf{k}_g has a projection along the x table axis, or if \mathbf{k}_g is not normal to the faces of the crystal by design; in these cases, the observation angles that produce perfect transverse quasi-phasematching are temperature dependent, and thus one must numerically solve the vector QPM condition for experimental design.

4.2.1 Detection geometry and integration domain effects: Degenerate SPDC

The condition that follows from Eq. 81, which guarantees the transverse QPM condition in our experimental configuration for the frequency-degenerate case $\omega_s = \omega_i = \omega_p/2$, is $\theta'_s = \theta'_i = 2.16^\circ$. Figure 3(a) shows the experimental observation produced with our $\Delta\theta = 0.086^\circ$ and filter pair A, which is our best approximation to the case where the angle and frequency integration domains are negligible; a comparable theoretical calculation, produced with integration parameters matching our experimental conditions, is shown in Fig. 4(a). In this case, the theory clearly predicts that the pair rate detected using narrowband filters is proportional to $|s(\Delta k_z)|^2 = |\text{sinc}(\Delta k_z)|^2$ with negligible integration effects.

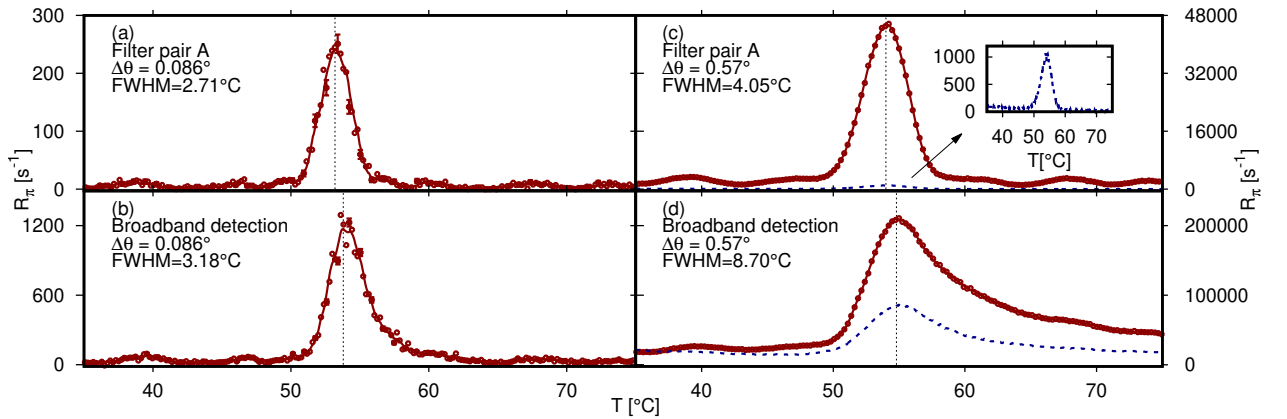


Figure 3. Measured rate of pair detection R_π as a function of crystal temperature T with central observation angles $\theta_s = \theta_i = 2.16^\circ$ using a crystal of type A. Accidentals are shown as dashed lines.

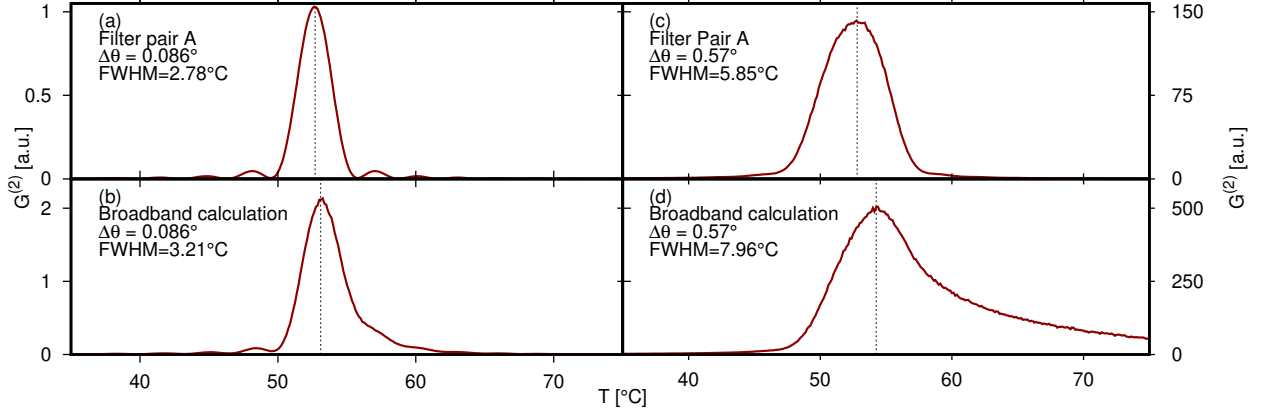


Figure 4. Calculated rate of pair detection R_{π} as a function of crystal temperature T with central observation angles $\theta_s = \theta_i = 2.16^\circ$.

As the dependence of Δk_z on crystal temperature variations is approximately linear the rate of pair detection as a function of crystal temperature may be used to study $|s(\Delta k_z)|$ (see Ref. (Jiménez, 2014)), which is expected to be a squared sinc in the case of an ideal poling micro-structure. The experimental result, however, produces an observation with a notably different functional form compared to the theoretical calculation. The main distinctive features of the observation include a narrower and sharper distribution around the principal maxima, along with secondary features that are significantly stronger than those expected in the ideal case. The photon pair rates produced by these irregular secondary features remain non-negligible within the detectable temperature range and produces deep minima in between the nodes. The effect of increasing the detected solid angles and bandwidths are shown in experiments in Fig. 3(b-d) and in Fig. 4(b-d) for the corresponding calculations; we see that the narrowband results remain symmetric, while increasing the detection bandwidth produces non-symmetric observations. Comparing the theoretical results with the observations we see a generally good agreement in all cases, beyond the differences we have noted.

4.2.2 Tuning curves and correction terms

To understand the origin of the features observed in the results shown in Figs. 3 and 4, it is instructive to consider the so-called temperature and angular tuning curves, which are defined as the loci for which $\Delta k_z = 0$, assuming $\Delta k_\perp = 0$ is met (so that $\sin \theta_s / \sin \theta_i = \lambda_s / \lambda_i$). As has been reported in studies using PPKTP, there is a large discrepancy in the calculated values of the tuning curves which may be compensated by use of an empirically-determined, temperature-dependent correction term (Emanuelli and Arie, 2003). The tuning curves for crystal type A are calculated using a correction term of form $\tilde{k} = 2\pi[790 - 12(T - 65)]\text{m}^{-1}$, derived from an extensive series of experiments using our SPCMs and narrowband filters; feature-extracted data from these measurements is shown along with the tuning curves in the figures below.

Figure 5 shows the tuning curve for the crystal temperature, T , as a function of the signal emission wavelength λ_s , for external observation angles of $\theta' = 2.16^\circ$ and $\theta' = 2.74^\circ$ in a crystal of type A.

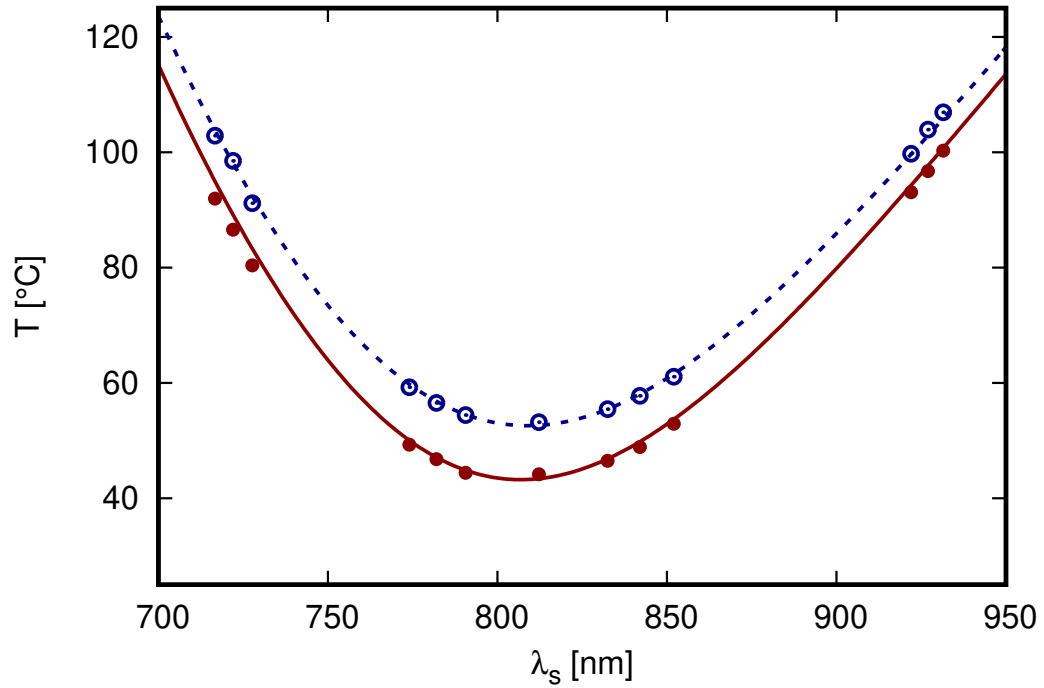


Figure 5. Tuning curve and experimental data for the crystal temperature T as a function of signal wavelength λ_s for the external observation angles $\theta'_s = 2.16^\circ$ (solid points and line in red) and $\theta'_s = 2.74^\circ$ (open points and dashed line in blue).

The temperature tuning curve of Fig. 5 presents a quasi-parabolic form, typical of type-0 QPM produced with periodically poled crystals, and attains its minimum in the vicinity of the degenerate wavelength $\lambda_p/2 = 812.2$ nm, while emission at non-degenerate wavelengths are quasi phase-matched at higher crystal temperature. More consequences of the form of this tuning curve may be seen in our results: for example, the observed increase in the temperature at which the maximal rate of pair detection appears in Figs. 3 and 4 as the integration parameters are made larger is a direct consequence of the concave shape and the location of the minima of the temperature tuning curves seen on Fig. 5.

For angular tuning curves, we fix the signal to idler ratio and subsequently plot the external signal emission angle θ'_s as a function of the crystal temperature for which $\Delta k_z(T) = 0$ holds. Figure 6 shows a set of tuning curves for the external emission angle θ'_s as a function of crystal temperature for crystal A.

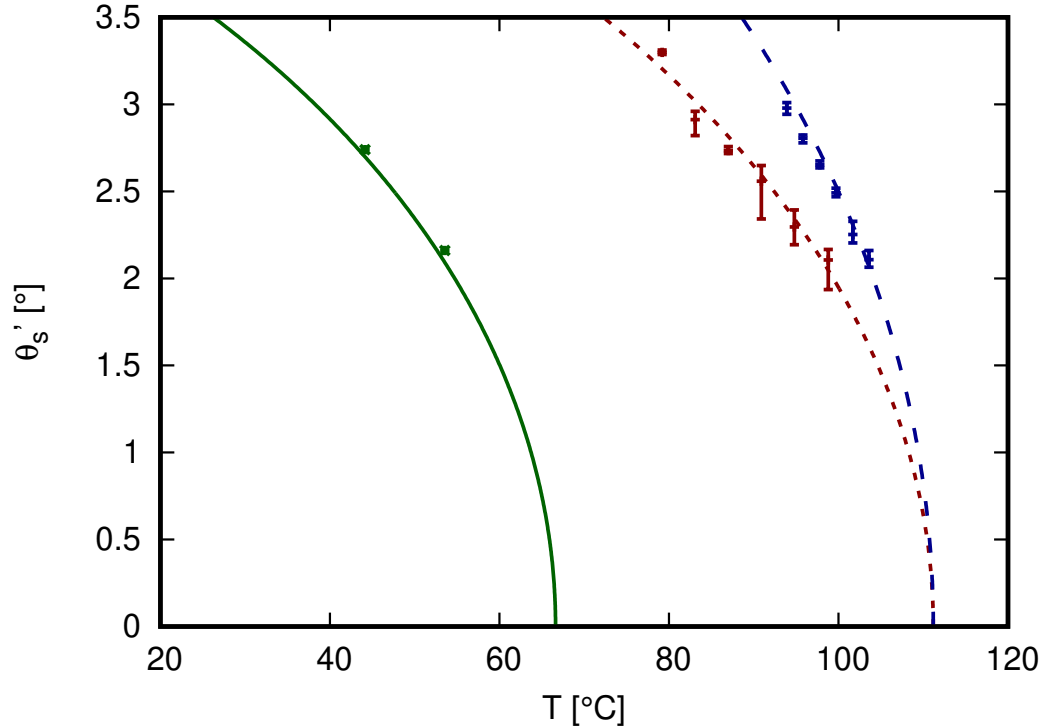


Figure 6. Tuning curve and experimental data for the external signal angle θ'_s as a function of crystal temperature T for degenerate emission with $\lambda_s = \lambda_i = 812$ nm (solid line and points in green), and the non-degenerate emission with $\lambda_s = 722$ nm (red dashed line and points) and $\lambda_i = 927$ nm (blue dashed line and points) for crystals of type A.

In all of the cases, as the temperature of the crystal is increased from room temperature the external emission angle θ'_s decreases tuning curves show a steep decrease in emission angle as the temperature reaches their respective collinear QPM temperature. The degenerate emission is described by a single curve, while non-degenerate pairs produce a pair of curves, describing the emission angle of the signal and idler wavelengths, and which coincide in the collinear case.

From Figs. 5 and 6 it is clear that the collinear QPM temperature for the non-degenerate emission is higher, for both the shorter and longer emission wavelengths, than that required for degenerate and near-degenerate pairs, and this remains the case for any other observation angle. This, along with the broad minima seen in Fig. 5 is reason that our observation for the temperature dependence of the photon pair rates in the degenerate case using filters, which may be considered of a relatively large bandpass width, produce essentially perfectly symmetric observations. As a consequence of this, the degenerate and near-degenerate emission is produced with essentially no broadening due to detection bandwidth and producing comparable results using non-degenerate pairs would require filters with significantly narrower bandpass widths.

In the broadband detection cases, the situation is significantly different, and detection aperture plays a much more important role. In contrast with the more simple and symmetric case of degenerate emission, the broadband detection observations are asymmetric and increasing the detection aperture greatly increases this asymmetry as it allows more significantly non-degenerate photon pairs to be coupled into both of the detectors at higher temperatures. In the detection geometry used for Figs. 4(d) and 3(d), for example, photon pairs with a signal-idler wavelength ratio of up to 1.33 may attain QPM at the opposite edges of the two detection apertures, which corresponds to wavelengths of approximately 711 nm and 945 nm.

The tuning curves of the type B crystals are of broadly similar form to those seen in crystals of type A. However, due to the large increase in down-converted power, we have been able to more accurately characterize the emission produced in the type B crystals. First, we have characterized the external signal emission angle θ'_s of the degenerate down-conversion in the plane parallel to the optical table as a function of crystal temperature, as shown in Fig. 6. This was done by implementing an ellipse-

fitting algorithm to a series of pictures of the narrowband-filtered degenerate down-conversion ring, taken at different crystal temperatures, which relies on the known separation between adjacent picture elements in the CCD sensor to be used. Then, we have measured the pair rate as a function of the crystal temperature using a crystal of type B, as shown in Fig. 7. From this observation, it is possible to infer the value of the longitudinal quasi phase mismatch Δk_z by identifying the location of the extrema with the values which are appropriate in the ideal case according to our theory. The result is shown on Fig. 8 where the observation is compared with three tuning curves: one calculated with no correction term, another calculated with the correction term produced using crystal type A, and one final curve representing a quadratic fit for the quasi-phase mismatch of form $\Delta k_z(T)L/2 = -34.09 + 0.2887T + 6.718 \times 10^{-4}T^2$, with the temperature in degrees Celsius. The description of the quasi-phase mismatch that been derived form this set of experimental data remains accurate throughout the available temperature and angular range for the degenerate emission in both of our crystals of type B.

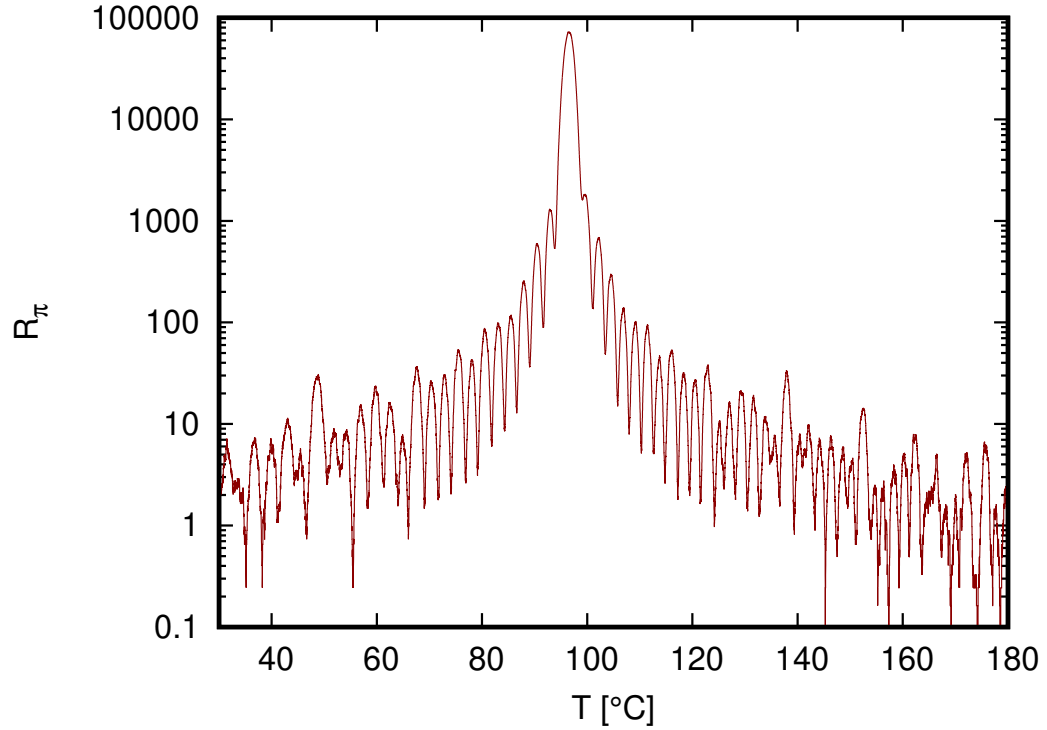


Figure 7. Measured rate of pair detection R_π as a function of crystal temperature T for $\theta_s = \theta_i = 2.165^\circ$ and filter pair A using a crystal of type B with signal and idler detection angles of $\Delta\theta = 0.086^\circ$.

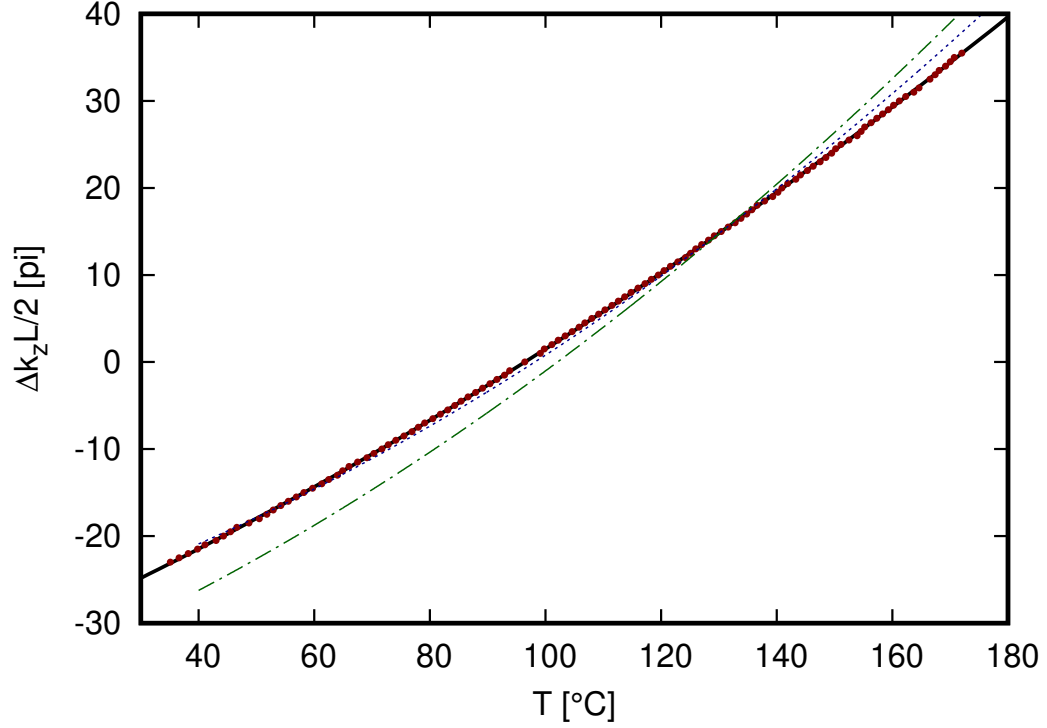


Figure 8. Measured reduced longitudinal quasi-phase mismatch $\Delta k_z L/2$ as a function of crystal temperature T for frequency degenerate down-conversion, $\omega_s = \omega_i = \omega_p/2$, with the detection geometry $\theta_s = \theta_i = 2.165^\circ$ (red circles). Also shown is a quadratic fit to the data (solid black line), along with the curves calculated using our correction term \hat{k} (blue dashed line) (Jimenez *et al.*, 2017) and theory calculated using no correction (dot-dashed green line).

4.2.3 Temperature dependence using two-frequency pump

We now consider the consequences of pumping the crystal with the laser running in two spectral lines of nearly equal power, with line separation much greater than either line-width. With care, the pump laser could be stabilized in this condition for certain laser operation temperatures, which were found to vary session-to-session, perhaps due to variations in room temperature. The individual line-widths were unresolved by the spectrometer, but they were presumably similar to the single-line bandwidth quoted earlier.

The measured dependence of the pair rate R_π and the signal and idler rates of single photon detection, R_s and R_i , as a function of crystal temperature, using a two-frequency pump is shown in Fig. 9. The measurement is performed under the same pump and detection geometry conditions as Figs. 4(a). The two emission wavelengths of the pump laser are approximately 0.082 nm apart, with the more intense line corre-

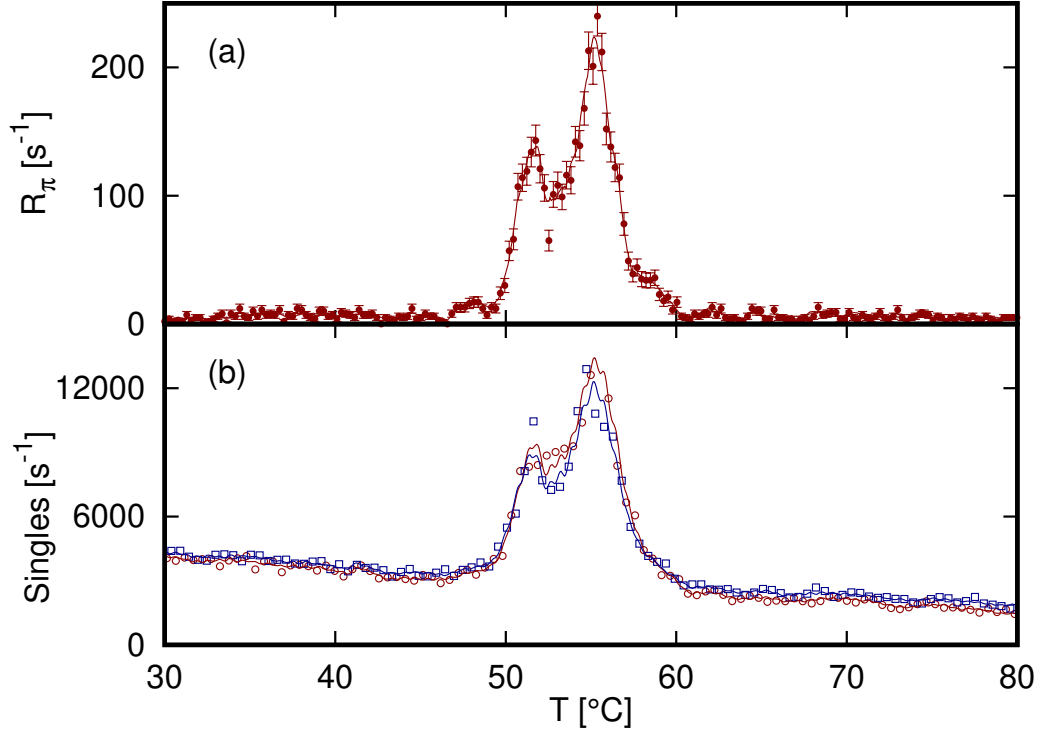


Figure 9. (a) Measured rate of pair detection R_π and (b) rates of single photon detection for the signal (red open circles and continuous line) and idler (blue open squares and continuous line) detectors, as a function of crystal temperature T for $\theta_s = \theta_i = 2.16^\circ$ and filter pair A with a two-frequency pump spectrum with a line separation of approximately 0.082 nm and $\Delta\theta = 0.086^\circ$ detection apertures.

sponding to the reference $\lambda_p \approx 406.118$ nm along with a weaker line at $\lambda_p \approx 406.036$ nm. Also shown in Fig. 9 is the measured rate of signal and idler photons R_s and R_i . That the signals observed in the two single-photon detectors are almost entirely identical is a consequence of the measurements having been performed in the degenerate QPM configuration such that, to a very high accuracy, $\theta'_s = \theta'_i = 2.165^\circ$. We note that, compared with the single-photon observations, the pair detection measurement shows significantly less integration effects with a more clearly defined minima between the two distinct structures; in addition to this, the pair detection observation is devoid of the uncorrelated, polarization dependent, background that is characteristic of KTP.

An additional set of measurements of the rate of pair detection R_π observed with two different two-frequency pump spectra is shown in Fig. 10 with $\theta_s = \theta_i = 2.165^\circ$. The measurements of this figure were performed with a pump beam with an e^{-1} amplitude radius of approximately 400 μm and a diverging radius of curvature of 760 mm at the crystal center, although these changes are of little consequence in the results presented. In addition, for comparison purposes, a measurement produced

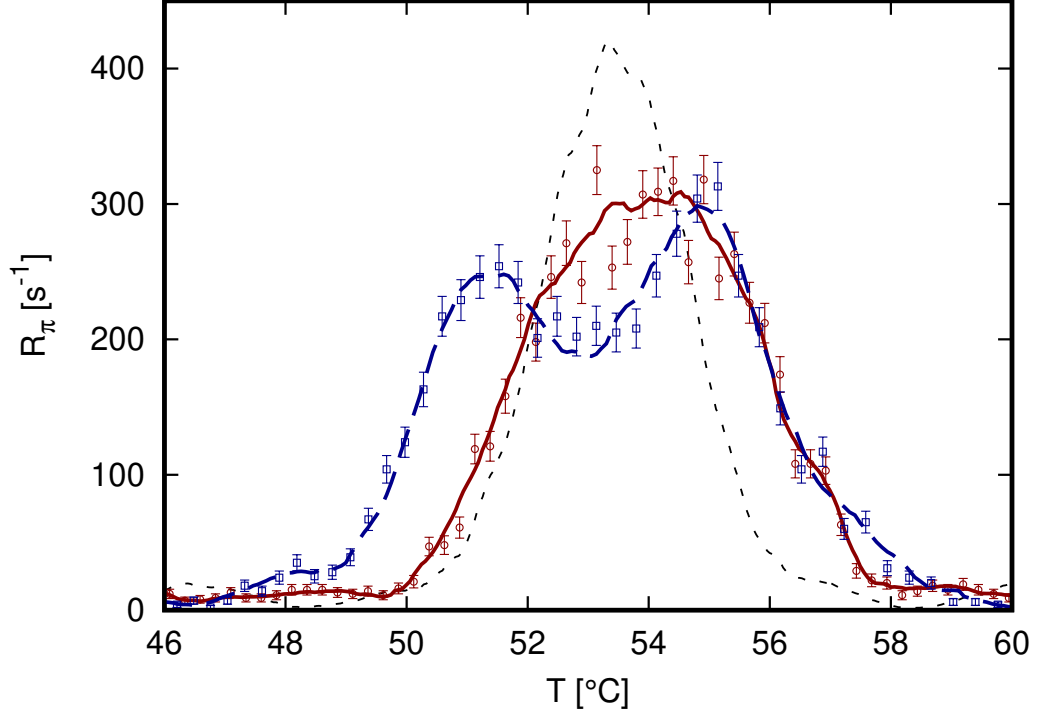


Figure 10. Measured rate of pair detection R_π as a function of crystal temperature T for $\theta_s = \theta_i = 2.165^\circ$ and filter pair A. Results are shown for a single frequency pump at 406.118 nm (black dashed line), for pump lines at 406.09 and 406.16 nm (red open circles and continuous line), and for pump lines at 406.07 and 406.16 nm (blue open squares and dashed line).

with the reference wavelength in single-frequency mode is also shown in the figure. The single frequency result shows a single peak at $T \approx 53^\circ\text{C}$, while the two-frequency result with two lines at 406.09 and 406.16 nm shows a considerably broadened pair rate distribution and, finally, the two-frequency result with two lines at 406.07 and 406.16 nm shows two distinct peaks separated by approximately 3.5°C . In this final result, theoretical calculations show that the peak in the left is produced the shorter pump wavelength, and the peak on the right is produced by the longer one. Further, the calculations imply that, as a function of pump wavelength, the peak position in a single-line temperature scan is displaced at a rate of $44^\circ\text{C}/\text{nm}$, which is consistent with the peak separation observed here.

The theoretical results corresponding to these two-frequency conditions are calculated as the sum of the pair rates produced by each laser line. More generally, the two-photon amplitude $\psi(\mathbf{k}_s, \mathbf{k}_i)$ in our pair rate expressions should be taken as the sum of that produced by each pump line. Upon substituting $\psi(\mathbf{k}_s)$ to calculate the pair rate, significant interference terms arise at the beat frequency in the region of overlap

between the two single-frequency distributions. However, this beat frequency is so high here (even with our closest available laser lines it is ≈ 100 GHz) that interference is washed out by detector temporal resolution, and it is then appropriate to sum the pair rates of each line.

4.2.4 Non-degenerate SPDC

For observation of non-degenerate photon pairs, we may use filter pair B with signal observation angles set to $\theta_s = 2.32^\circ$, or filter pair C with idler observation angle set to 2.76° , with the shorter wavelength reserved for the idler detector that is fixed at $\theta_s = 2.165^\circ$. The measured rate of pair detection R_π for the narrow-band filtered, non-degenerate photon pairs as a function of crystal temperature T is shown in Fig. 11 for a crystal of type A. The observation aperture used with filter pair C has increased to account for the reduced pair efficiency of the filters to a good approximation.

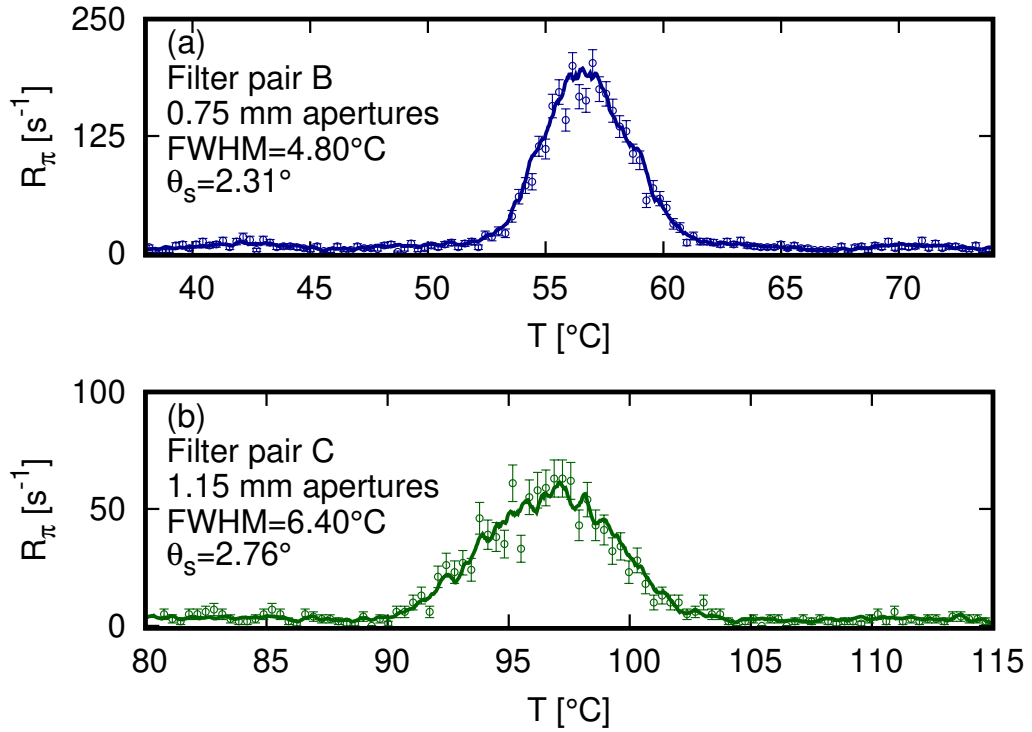


Figure 11. Measured rate of pair detection R_π as a function of crystal temperature T for a crystal of type A with (a) $\theta_s = 2.32^\circ$ using filter pair B with $\Delta\theta = 0.086^\circ$ detection apertures and (b) $\theta_s = 2.76^\circ$ using filter pair C with $\Delta\theta = 0.15^\circ$ detection apertures.

The cited increase in the integration angles for the observations with filter pair C produces negligible effects in the observations due to the comparatively larger significance of detection bandwidth in this highly non-degenerate regime.

Calculations produced with comparable conditions are shown in Fig. 12; here, the detection angle has been kept constant for the case corresponding to filter pair C without considering the reduced transmission, we have shown a similar comparison in (Jimenez *et al.*, 2017) where the transmission is modeled and the aperture effect is introduced. Good agreement is seen in these results upon comparing the general shape, and height of the curves; however, as observed in the degenerate case, the secondary structures which surround the principal mode of the distribution are significantly stronger in the experiment than what is shown in the calculations.

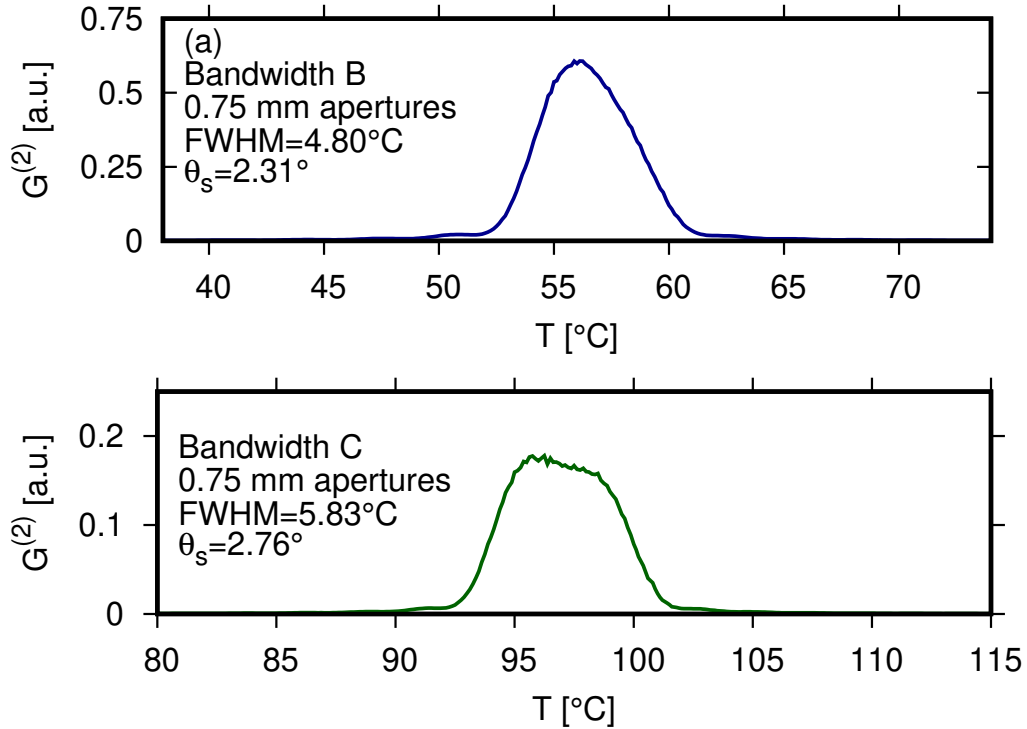


Figure 12. Normalized rate of pair detection R_π as a function of crystal temperature T as calculated for (b) $\theta_s = 2.32^\circ$ using the pair detection bandwidth of filter pair B and detection apertures of $\Delta\theta = 0.086^\circ$ and (c) $\theta_s = 2.76^\circ$ using the pair detection bandwidth of filter pair C and detection apertures of $\Delta\theta = 0.086^\circ$.

Another difference that can be noted is the increased width of the experimental result corresponding to filter pair C compared to the numerical result. This may be a consequence of the relatively soft edges which these bandpass filters present in their transmission spectrum; effectively, this can cause an increase in the detection band-

width of the experiment which translates to a larger temperature range over which the main peak of the signal is detected. Ultimately, it is also a manifestation of the more significant role of angular dispersion for the non-degenerate emission.

4.3 Angular dependence of the pair rate

In this section, we study the pair rate R_π as a function of the signal detection angles θ_s and ϕ_s . The effects of frequency and angle integration are explored, an interesting effect on the shape of the so-called coherence cell due to the longitudinal QPM function is highlighted, and a result with a two-frequency pump is also shown. For each measurement, the crystal temperature was carefully selected to tune the fixed idler detector to the desired detection modes, the temperature was then kept constant, and the spectrum of the pump was monitored for stability.

4.3.1 Narrowband detection

To maximize the efficiency of the detection of narrowband-filtered coincident photon pairs, under conditions of Gaussian pump beam with small detection angles, it is necessary to configure the experiment according to Eq. 81 and to set the crystal temperature to that at which the longitudinal QPM condition is attained. We can produce this temperature with the QPM relation and our correction terms only approximately, as this must be known to $\approx 0.1^\circ\text{C}$, and depends strongly on pump wavelength which may itself vary slightly with day-to-day room temperature variations. Variation of the observation angle from the prescription of Eq. 81 allows the characterization of the shape and size of the coherence cell.

Figures 13 and 14 show the pair rate R_π as a function of θ_s and ϕ_s , at the temperature that was observed to produce the longitudinal QPM condition in each case. For the series of filter pairs A, B, and C, the results show decreasing rates with approximately Gaussian distributions. The pair rate reaches nearly 350 s^{-1} for filter pair A while, for the lowest curve with filter pair C, with the detection apertures slightly larger to compensate for the reduced transmission of the filters, the peak is near 60 s^{-1} . In the

case of the θ_s dependence they are centered on increasing θ_s and they are approximately 0.2°C wide with increasing width. To observe the ϕ_s dependence, we first set the θ_s angle to the value for which the maximum of the distribution observed in Fig. 14 occurs, and then we proceed to vary the ϕ_s angle. The ϕ_s distributions are seen to present marginally decreasing widths in the non-degenerate observations compared to the degenerate case, with the case of filter pair C showing a somewhat narrower result than the previous two cases.

The theoretical results for the θ_s and ϕ_s dependence of the pair rate R_π are shown in Figs. 15 and 16, respectively. These are seen to compare favorably with the observations, showing the broadly Gaussian-like shapes that produce decreasing rates at the peak as they are made more non-degenerate along with the increased width of the results for the non-degenerate observations. The ϕ_s dependence also shows decreasing widths with the more non-degenerate cases, as was seen in the experiment, yet the widths seen here are generally broader by a small amount.

With this, we have explored the condition of maximal efficiency in the detection of the narrowband-filtered photon pairs. Now, we will show a result where the experiment is intentionally detuned from this condition to produce an effect that appears to be novel.

4.3.2 Effects of the longitudinal QPM function in the angular dependence of the degenerate photon pair emission

When the longitudinal QPM $s(\Delta k_z)$ is approximately constant, the angle scan of the pair rate is solely determined by the shape of the spatial mode of the pump beam, as can be seen in Eq. 80. However, near the temperatures for which $|s(\Delta k_z)|^2$ reaches zero, this zero order approximation is no longer appropriate, and the pair rate R_π may show significant consequences due to this.

In Fig. 17 we see the result of an angle scan of the narrowband-filtered pair rate R_π similar to the degenerate result of Fig. 13, performed using a crystal of type B and the laser system LS1 at $T = 132.2^\circ\text{C}$, which is the QPM temperature for this interaction with this laser system and which maximizes the pair rate. As expected from the lower

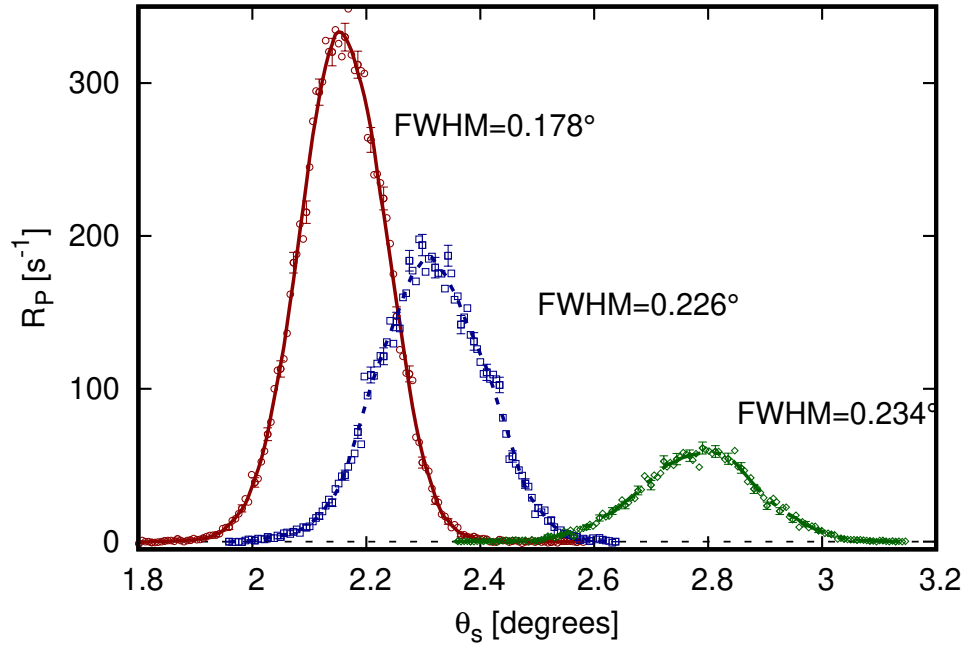


Figure 13. Measured rate of pair detection R_π as a function of the signal central detection angle θ_s using a crystal of type A (a) filter pair A (open red circles and continuous line) at $T = 53.2^\circ\text{C}$ with $\Delta\theta = 0.086^\circ$ detection angles, (b) filter pair B (open blue squares and dashed line) at $T = 56.0^\circ\text{C}$ with $\Delta\theta = 0.086^\circ$ detection angles, and (c) filter pair C (open green diamonds and dot-dashed line) at $T = 97^\circ\text{C}$ with $\Delta\theta = 0.15^\circ$ detection angles.

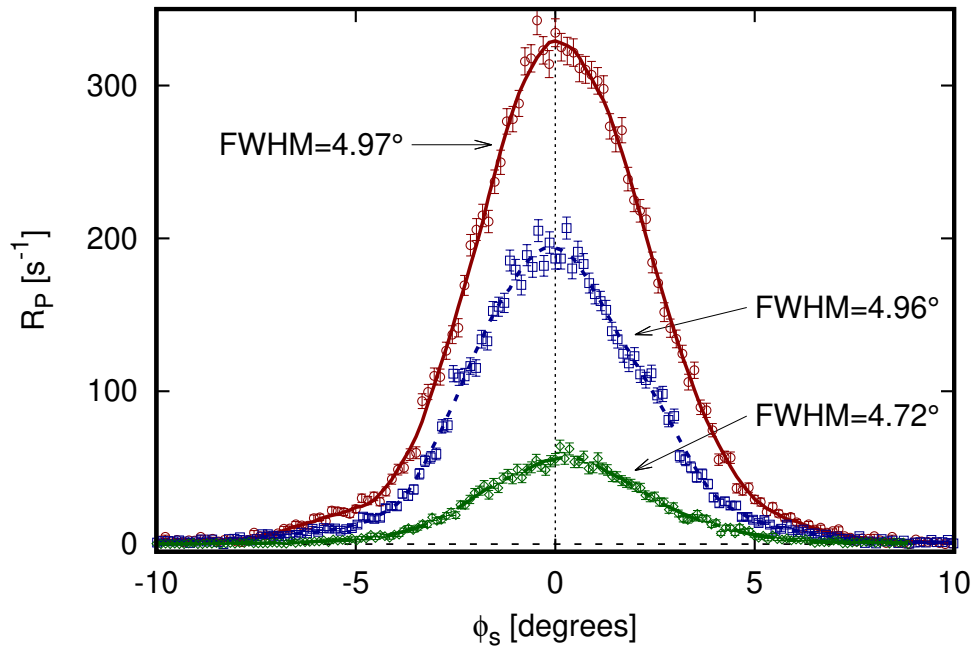


Figure 14. Measured rate of pair detection R_π as a function of the signal central detection angle ϕ_s using a crystal of type A with (a) filter pair A (open red circles and continuous line) at $T = 53.2^\circ\text{C}$ with $\Delta\theta = 0.086^\circ$ detection angles, (b) filter pair B (open blue squares and dashed line) at $T = 56.0^\circ\text{C}$ with $\Delta\theta = 0.086^\circ$ detection angles, and (c) filter pair C (open green diamonds and dot-dashed line) at $T = 97^\circ\text{C}$ with $\Delta\theta = 0.15^\circ$ detection angles.

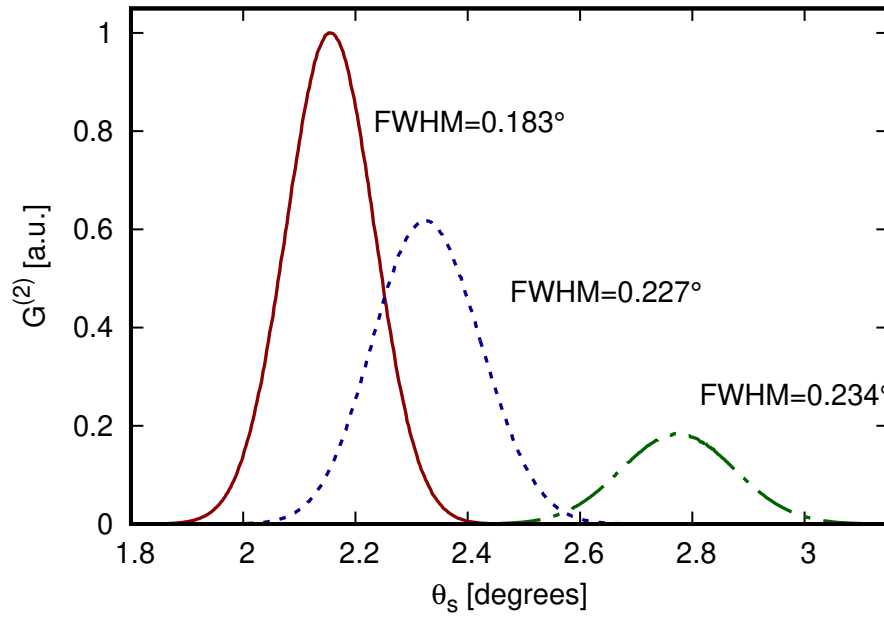


Figure 15. Calculated pair rate R_π as a function of the signal central detection angle θ_s using observation angles of $\Delta\theta_s = 0.086^\circ$ with the pair detection bandwidth of filter pairs (a) A at $T = 53.0^\circ\text{C}$, (b) B at $T = 56.2^\circ\text{C}$, and (c) C at $T = 97.0^\circ\text{C}$.

power of LS1 compared to the LS2 system that was used for the result of Fig. 7, the rates here are comparably smaller, yet far larger than observed with the crystals of

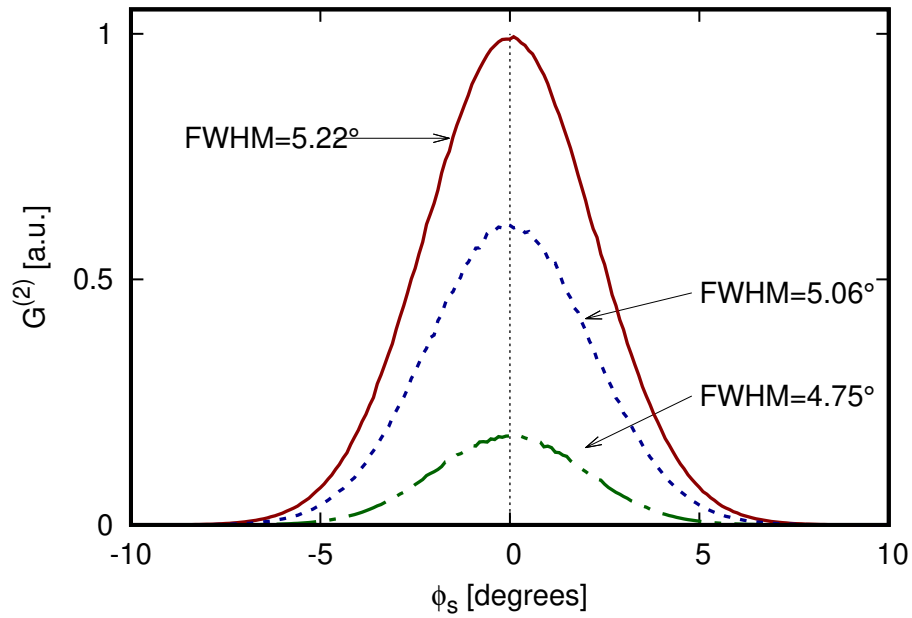


Figure 16. Calculated pair rate R_π as a function of the signal central detection angle ϕ_s using observation angles of $\Delta\theta_s = 0.086^\circ$ with the pair detection bandwidth of filter pairs (a) A at $T = 53.0^\circ\text{C}$, (b) B at $T = 56.2^\circ\text{C}$, and (c) C at $T = 97.0^\circ\text{C}$.

type A. The width of this result is $\Delta\theta_s = 0.19^\circ$ and remains approximately equal to that observed with the previous crystal, as expected.

Figure 18 shows the pair rate and the rate of single photon detection for an angle scan performed under conditions similar to Fig. 17 but with $T = 134.7^\circ\text{C}$. It is seen that, upon increasing the crystal temperature by just 2.5°C the pair rates detected by the system decreased sharply to under 900 s^{-1} . In addition, the distribution of the pair rate is now observed to be bimodal, with the left and right modes being produced by the primary and secondary rings of the degenerate SPDC emission, as observed by comparing the features with the single-photon detection rates which are also shown in the figure. The origin of the bimodal shape is clearly the monotonic behavior of the $s(\Delta k_z)$ function around the angle at which it attains a value of π .

Figure 19 shows a calculation of the pair rate under comparable conditions to those of Fig. 18 and the corresponding values of $\Delta k_z/2$, the normalized argument of the longitudinal QPM function. For this calculation, the crystal temperature has been increased by a similar 2.0°C from the longitudinal QPM temperature, and the bandwidth has been matched to that of filter pair A. It is clear that the bimodal structure is also represented in this result, and that the location of the minimum very nearly coincides with the point at which $\Delta k_z L/2 = \pi$. The depth of the minimum depends on integration angle and frequency to similar extents, and also on the actual complex longitudinal QPM function which the crystal presents as it may not produce a real zero crossing in crystals with low poling quality such as our samples of type A.

By carefully tuning the temperature of the crystal, it is possible to produce any desired ratio between the two lobes that are detected in this condition. The two lobes present a two-photon phase difference of approximately 180° , although this is not demonstrated here as the coincident detection arrangement we have constructed only detects the two photon intensity and not the phase. An experimental characterization of this phase difference may yield an interesting picture of the longitudinal homogeneity of the crystal, as well as serve as a method to characterize the complex two-photon amplitude itself. This structured coherence cell that we have presented here appears to be, in the case where the two lobes have the same amplitude, indistinguishable from that generated by a first-order Hermite Gaussian pump beam in the phasematched configuration.

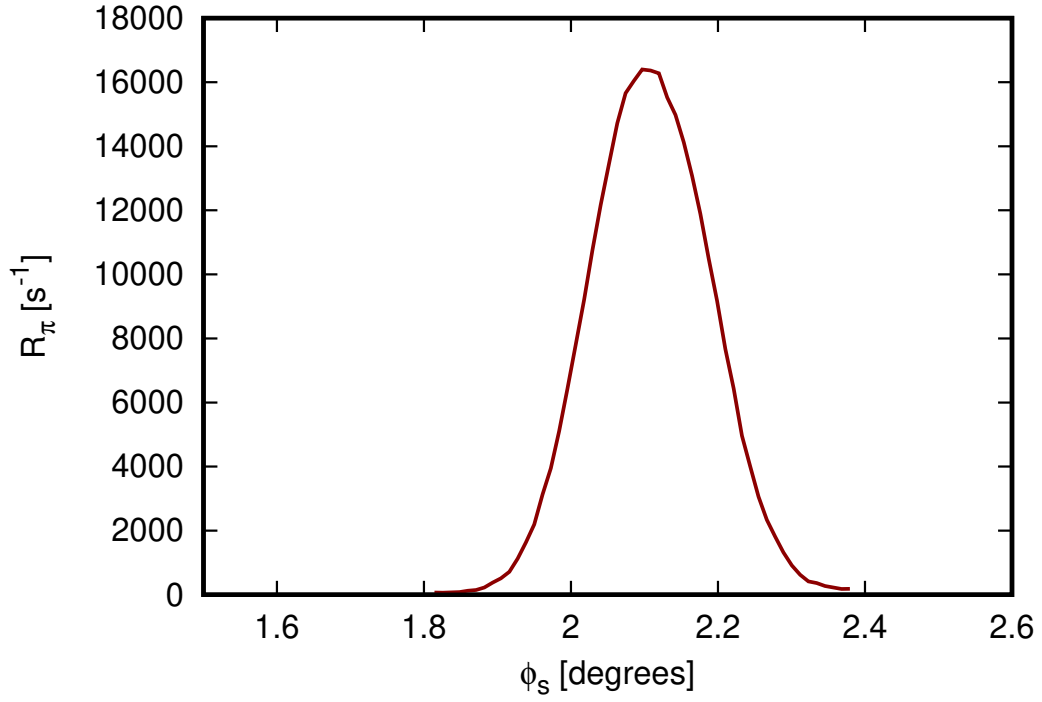


Figure 17. Measured rate of pair detection R_π as a function of the signal central detection angle θ_s using a crystal of type B at $T = 132.2^\circ\text{C}$ with $\Delta\theta = 0.086^\circ$ detection angles using laser system LS1.

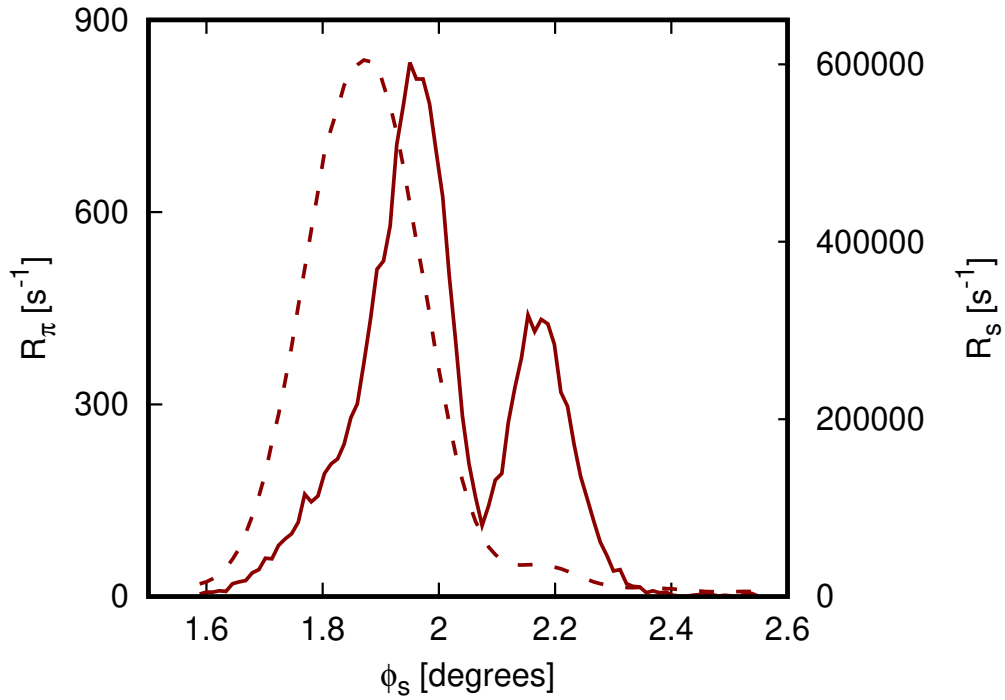


Figure 18. Measured rate of pair detection R_π (continuous red curve) and rate of signal photon detection R_s (dashed red curve) as a function of the signal central detection angle θ_s using a crystal of type B at $T = 134.7^\circ\text{C}$ with $\Delta\theta = 0.086^\circ$ detection angles using laser system LS1.

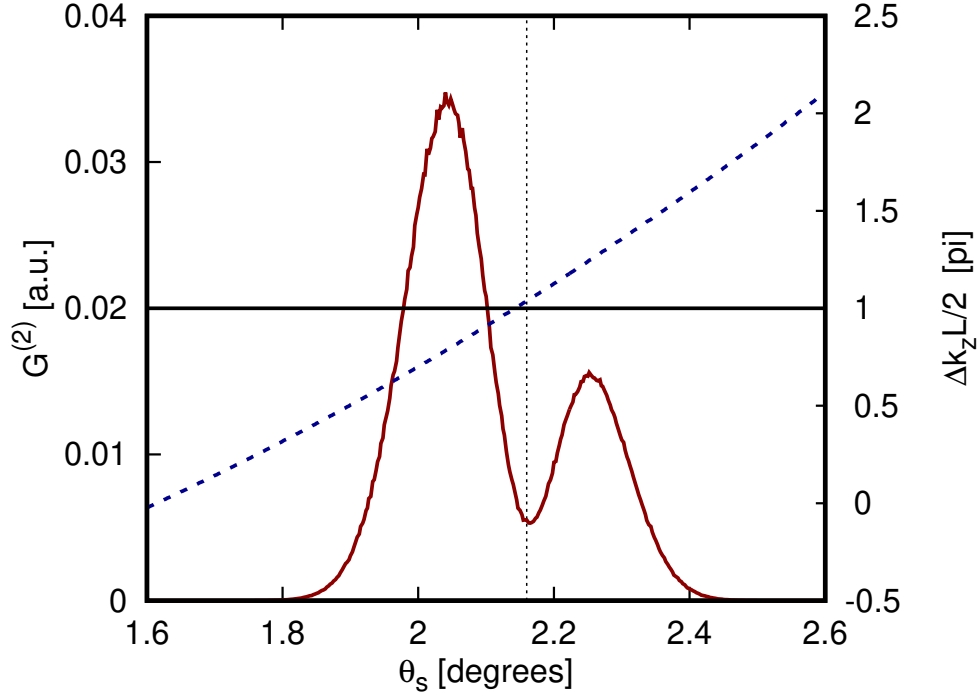


Figure 19. Calculation of the pair rate R_π (solid line, left axis) with conditions comparable to Fig. 18. The value of the normalized longitudinal QPM is shown (blue dashed line, right axis) along with reference horizontal line (black, right axis). The idler detector is located at $\theta_i = 2.165^\circ$, and $T = 133.5^\circ\text{C}$.

4.3.3 Observations of the angular dependence of the pair rate with a two-frequency pump

The observation of angular effects in the coincident pair rate produced by the introduction of a two-frequency pump into the down-conversion crystal require a significantly more meticulous approach to preparation of the experimental conditions, compared to the observation of similar effects in the temperature dependence. This may be understood by considering that the emission produced by each of the two frequencies present in the pump occurs with a difference in the emission angle which is significantly larger than the angular width of each of the degenerate cones. Thus, for the observations performed with negligible integration angles for narrowband-filtered degenerate SPDC, only one of the emission cones can be coupled into the fixed idler detector. In this case, the presence of the second down-conversion ring does not produce significant coincidences in the detection.

To observe the desired effects, we have increased the integration angle in the fixed idler detector to $\Delta\theta_i = 0.57^\circ$, so that a large range of angles can be coupled. The integration angle of the signal detector is kept at a $\Delta\theta_s = 0.086^\circ$, and the position of the detector is varied while the crystal is kept constant. Figure 20 shows the result of two such measurements, performed at $T = 53.2^\circ\text{C}$ and $T = 55.0^\circ\text{C}$ with identical pump spectra composed of two lines at 406.09 nm and 406.30 nm. The corresponding theoretical results are shown in Fig. 21.

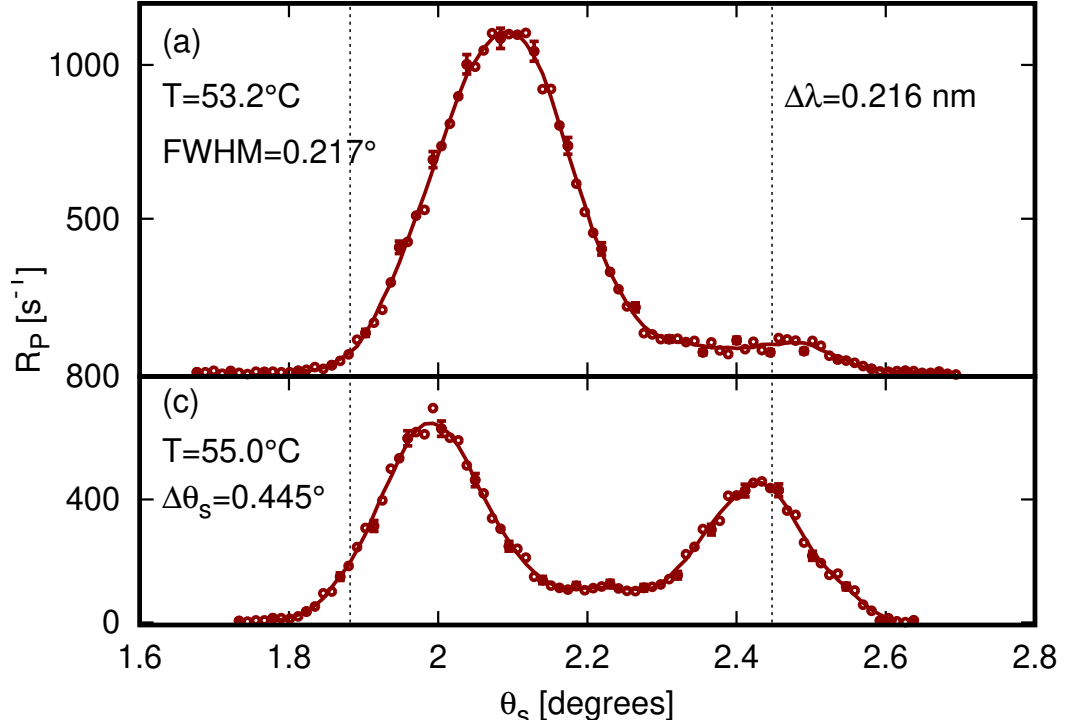


Figure 20. Measured rate of pair detection R_π as a function of the signal detection angle θ_s with two simultaneous pump lines at 406.09 and 406.30 nm, with $\theta_i = 2.16^\circ$ and detector aperture diameters $\Delta\theta_s = 0.086^\circ$ and $\Delta\theta_i = 0.57^\circ$. Filter pair A is installed. The vertical dashed lines indicate the angular limits of the coupling for the idler detection angle θ_i .

With the crystal at 53.2°C in Fig. 20(a), a distinct peak appears in the pair rates at $\theta_s \approx 2.1^\circ$. This high peak arises because a QPM condition occurs near the center of the idler aperture, due to the 406.09 nm pump line. The peak is somewhat analogous to the similar degenerate case of Fig. 13, but the larger idler aperture now relaxes the pair detection condition and the peak is slightly wider in Fig. 20(a). Good agreement is apparent in the calculation shown in Fig. 21(a); here we have found the high peak is produced solely by the 406.09 nm pump line, while both lines contribute equally to the low levels seen for $\theta_s > 2.3^\circ$.

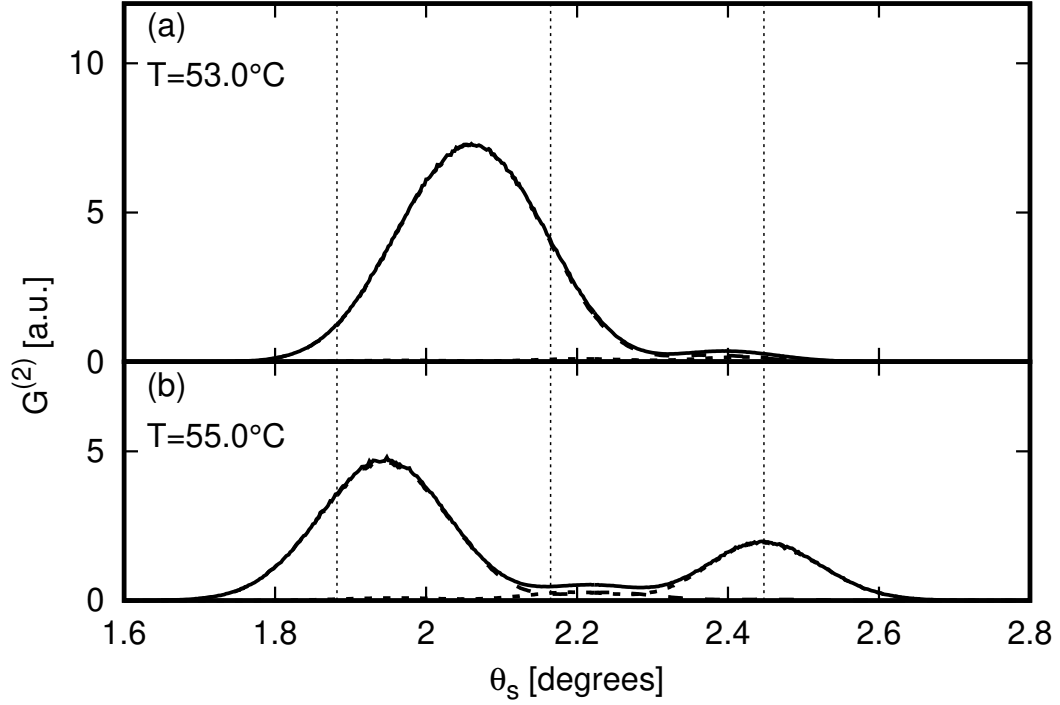


Figure 21. Calculation of the pair rate R_π as a function of the signal detection angle θ_s with conditions as in Fig. 20 for (a) $T = 53.0^\circ\text{C}$ and (b) $T = 55.0^\circ\text{C}$.

By increasing T to 55.0°C , the experimental peak of Fig. 20(a) moves to the left and appears at $\theta_s \approx 2.0^\circ$ in Fig. 20(b), and a second peak is now seen near $\theta_s \approx 2.4^\circ$. The second peak arises from a QPM condition produced with the other 406.30 nm pump line, which had fallen just outside the idler aperture in Fig. 20(a). In particular, in Fig. 20(b) the 406.30 nm line produces a QPM condition near the edge of the idler aperture at $\theta_i + \Delta\theta_i/2$, while the other pump line has its own QPM condition near $\theta_i - \Delta\theta_i/2$. Thus, idler photons produced by both pump lines are obviously detected throughout the scan of Fig. 20(b), but the peaks of Fig 20(b) only appear for θ_s where the signal detector encounters the pair members produced by one of the pump lines. This interpretation is supported by the theoretical result of Fig. 21(b) under similar conditions, and we find that the peak on the right is produced by the 406.30 nm pump line, the peak on the left is produced by the 406.09 nm pump line, and the low region halfway between these peaks has roughly equal contributions from both lines. It is a delicate issue to create this condition, and consequently the theoretical conditions differ just slightly in the temperature from those of the experiment, but the theoretical curve closely resembles the experimental result. Thus, it has been demonstrated here that a two-line pump can split the measured angular pair rate distribution between two corresponding peaks.

Further, our exact calculations that take proper account of angular integration effects have been essential in drawing this conclusion.

4.3.4 Broadband detection

Figure 22(a) shows pair data taken with open detector filters at $T = 53^\circ\text{C}$, which is approximately the QPM temperature for the degenerate emission with $\theta_s = \theta_i = 2.16^\circ$. Unlike the observations made with the narrowband filters of Fig. 13, which are symmetric, the distribution of the pair rate observed here is observed to be skewed towards the larger angles. It is clear that this skew is caused by the non-degenerate emission, which is coupled with reduced efficiency compared to the degenerate pairs due to the collection geometry and the small observation angles.

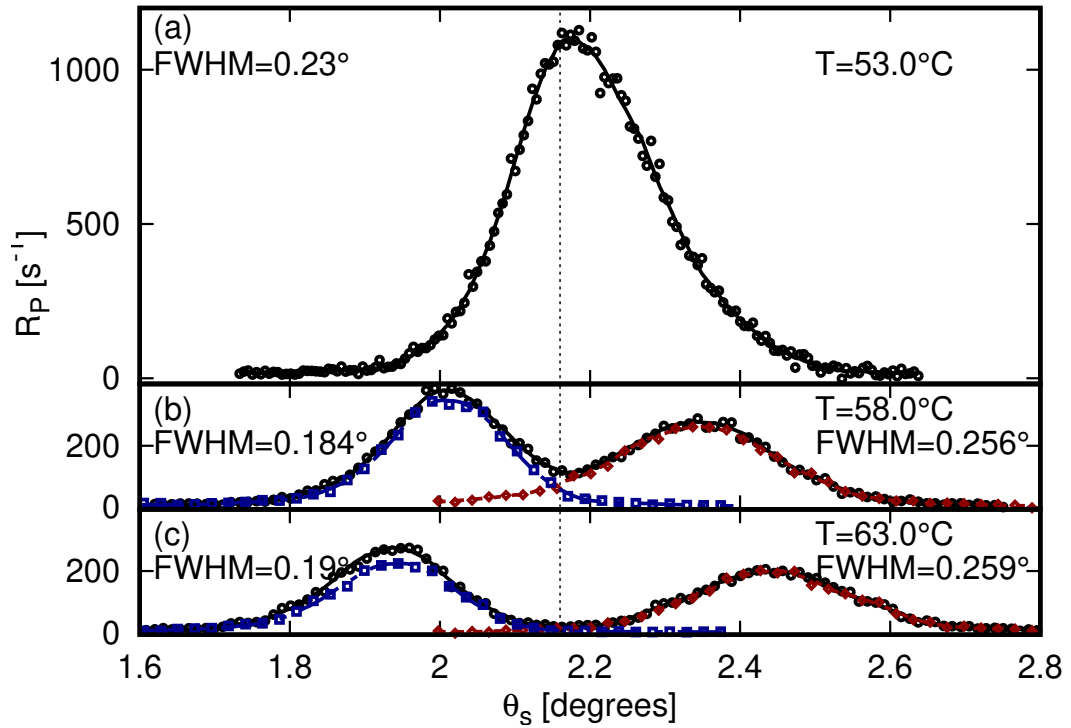


Figure 22. Measured pair rate R_p as a function of the signal detection angle θ_s with crystal temperatures T of (a) 53.0°C , (b) 58.0°C , and (c) 63.0°C with signal and idler integration angles of $\Delta\theta = 0.086^\circ$. See the text for further details.

Figure 22(b) and (c) shows the observations made at $T = 58^\circ\text{C}$ and $T = 63^\circ\text{C}$, where two peaks are clearly observed which lie at opposite sides of the idler observation angle $\theta_i = 2.16^\circ$; this indicates that the two lobes are composed of photon pairs with different spectrum, one for which the idler detector collects the shorter wavelength, with the signal detector at $\theta_s > \theta_i$, and vice-versa. The increasing separation of the two lobes as the temperature is increased indicates that the photon pairs coupled into the fixed idler detector become increasingly non-degenerate at these higher temperatures. To demonstrate this, we performed a measurement under identical conditions, but using an edge filter over the signal detector which steeply rises from negligible to nearly perfect transmission at 800 nm. Having removed the shorter wavelengths, we then measured the pair distribution in θ_s . Then, this same filter was instead placed over the idler detector, and a θ_s scan was again done. As far as the pair rate is concerned, the second case is equivalent to removing the longer wavelengths from the signal detector. The small shift of 800 nm from the degenerate wavelength 812.24 nm has little effects on the results, since few photons fall near degeneracy in the cases presented. The black open circles show the results of the measurements without any filters in front of the detectors, while blue open squares and red open rhombs are measured with an long-pass filter in front of the idler and signal detectors, respectively.

The calculations corresponding to the observations of Fig. 22 are shown in Fig. 23. In general, we see that the features of the observation are well represented, including the width and separation of the lobes.

We have presented here both experimental and theoretical results for the photon pair rates of the SPDC produced by a periodically poled crystal. In particular, the pair rates have been studied as a function of emission angle and of crystal temperature through a comparison of the results of experiments with exact numerical calculations using two different laser systems and crystals with different design of the periodic poling structure. Further results have been presented using a pump laser having two distinct emission lines. Our experimental conditions have allowed us to perform measurements with negligible integration effects at detected pair rates well above 10^5 s^{-1} . These statements may be put into perspective by comparing with previous experiments (Joobeur *et al.*, 1996; Malygin *et al.*, 1985; Grayson and Barbosa, 1994; Monken *et al.*, 1998; Walborn *et al.*, 2004; da Costa Moura *et al.*, 2010; Molina-Terriza *et al.*,

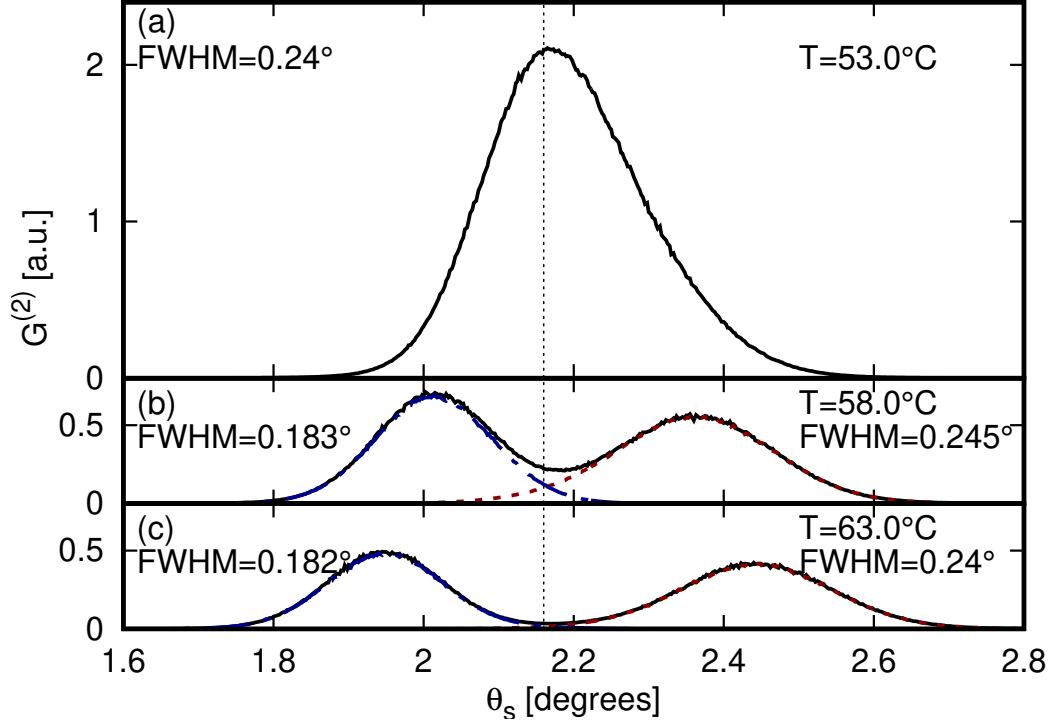


Figure 23. Calculation of the pair rate R_π as a function of the signal detection angle θ_s for detection conditions as in Fig. 22 at (a) $T = 53.0^\circ\text{C}$ and (b) $T = 55.0^\circ\text{C}$.

2005), where pair rates were of the order of 10^{-1} - 10^1 s^{-1} . The importance of our high pair rates and well-controlled experimental conditions is that they have allowed us to measure low-noise, reproducible data under a wide range of conditions and signal levels, thus allowing a more complete study of effects. We observed the down-converted power produced by our crystal samples varies by a significant amount spanning more than two orders of magnitude.

The theoretical methods developed here have played a similarly important role, since previous theoretical techniques do not generally produce accurate results under our experimental conditions. Our numerically exact results have been essential in obtaining general agreement with the experimental observations, as well as in understanding the physical origins of features seen in the data.

One possible application of our work is in the characterization of periodically poled crystals. The process of SPDC produces photon pairs through all possible second-order interactions of vacuum fluctuations with the pump beam, so that it can provide a means to study the possible QPM processes supported by a given crystal. For example, for the crystals of type A employed here, we have been able to conclude that its

longitudinal QPM function deviates significantly from the ideal form consistent with perfect poling, while our crystals of type B appear much closer to the ideal. On the other hand, our work also points towards a means of optimizing the photon pair rate under whatever conditions are desired, or toward further basic studies of the fourth-order coherence function of SPDC, while exactly quantifying the integration effects that inevitably occur.

Chapter 5. Calculations of the recombination of the entangled photon pairs

In this chapter, we evaluate the theoretical expressions obtained in Chapter 3 related to the recombination of entangled photon pairs. Numerical results are presented under a variety of conditions, which include results for an ideal optical system, as well as for realistic optical systems in which temporal dispersion of the photon pairs produces observable effects. Significantly, some of the results presented here have been published elsewhere (Jimenez *et al.*, 2019), where agreement with experimental results was generally reported. Other numerical results shown in this chapter, when possible, are compared with other experimental results as described below.

In order to make the experimental comparisons, the parameters assumed here are different from those of Chapter 4. Throughout this chapter, we assume the pump wavelength to be $\lambda_p = 532$ nm. We also assume that the nonlinear crystals are periodically-poled, MgO-doped lithium niobate of length 5 mm. The extraordinary refractive index used here follows from a Sellmeier equation Jundt (1997), while its temperature dependence is a quadratic fit to data that have been reported elsewhere Shen *et al.* (1992). To be close to the experimental situation, we assume that $\Delta \mathbf{k} = 0$ for axial, degenerate SPDC at crystal temperature $T_o = 50^\circ\text{C}$, and calculate the poling wave vector \mathbf{k}_g that satisfies this condition. This is done since \mathbf{k}_g is not known in the experimental works; the procedure described determines the poling period to be $2\pi/k_g = 6.951 \mu\text{m}$. In the calculations, we generally assume a circular limiting aperture of free-space radius $\tilde{\theta}_c = 1.5^\circ$, 2.3° , or 4.0° , with the middle case corresponding to the experimental results. As will be noted in many results presented here, the crystal temperature will be dropped to a lower temperature $T_o - \Delta T$ that depends on $\tilde{\theta}_c$; we use $\Delta T = 1^\circ\text{C}$ for $\tilde{\theta}_c = 1.5^\circ$, $\Delta T = 1.5^\circ\text{C}$ for $\tilde{\theta}_c = 2.3^\circ$, and $\Delta T = 2^\circ\text{C}$ for $\tilde{\theta}_c = 4^\circ$. This reduced temperature slightly opens the SPDC cone, thus improving the pair rate within the particular aperture radius. Finally, we take d_{eff} as $1.5 \times 10^{-11} \text{m/V}$.

5.1 Ideal optical systems

5.1.1 Linear transfer functions

An ideal optical system is taken as one for which dispersion compensation is perfect so that $\varphi_s(\omega) = \varphi_i(\omega) = 0$. We start with evaluations of the linear transfer function of Eq. 74 that describes the effect of pair recombination on the spatial mode of the up-converted light. For our case of a circular aperture the results are independent of ϕ_p , and we take the transfer function here as simply $\mathcal{E}_{\omega_p}^o(\theta_p)$.

Figure 24 shows $\mathcal{E}_{\omega_p}^o(\theta_p)$ for several aperture radii $\tilde{\theta}_c$. The curves there are purely real and are scaled to unit height; actual heights are 3.5×10^{-8} for $\tilde{\theta}_c = 1.5^\circ$, to 5.9×10^{-8} for $\tilde{\theta}_c = 2.3^\circ$, and 1.1×10^{-7} for $\tilde{\theta}_c = 4.0^\circ$. It is seen that all curves monotonically decrease in θ_p , and reach zero when the external pump angle $\tilde{\theta}_p$ is essentially $\tilde{\theta}_c$. This cut-off angle may be understood as follows. As the angle of a plane wave pump in the crystal is increased, the SPDC cone increases similarly in angle. Up-conversion requires intact photon pairs, which fall on opposing points with respect to the SPDC cone center; thus intact pairs no longer pass through the aperture when the *center* of the SPDC cone reaches the edge of the limiting aperture. This condition occurs for $\tilde{\theta}_p = \tilde{\theta}_c$, and up-conversion ceases.

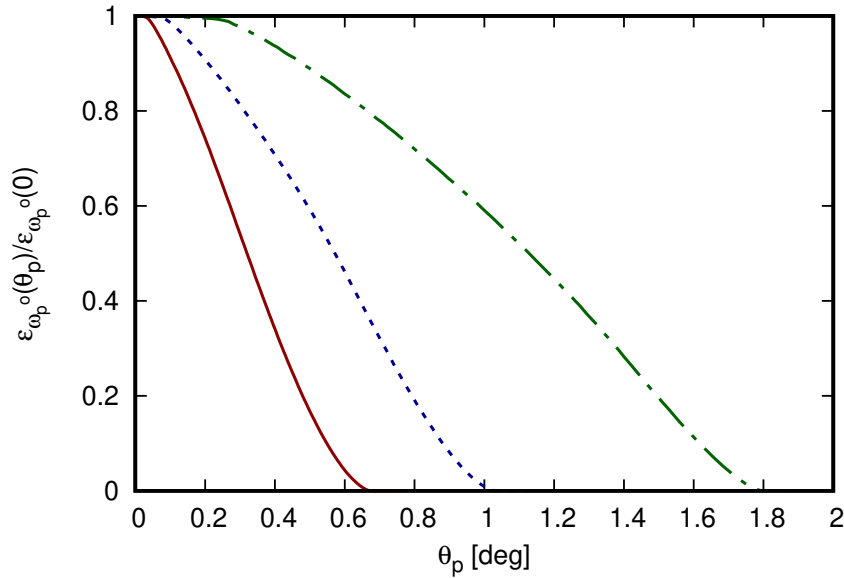


Figure 24. Normalized angular transfer function as a function of external angle θ_p for idealized photon pair recombination assuming 5mm lithium niobate crystals and an external cutoff angle $\tilde{\theta}_c$ of 1.5° (continuous red line), 2.3° (dashed blue line), and 4.0° (dot-dashed green line), with ΔT as specified in the text.

The transfer function $\mathcal{E}_{\omega_p^o}(\theta_p)$ may be considered an angular amplitude spectrum; it follows that its corresponding transverse spatial distribution in the up-conversion crystal may be found from its two-dimensional inverse Fourier transform (Ref. Goodman (2005), Sect. 3.10.1). With $\mathcal{E}_{\omega_p^o}(\theta_p)$ being ϕ_p -invariant, the inverse transform simplifies to the Fourier-Bessel integral (Goodman (2005), Sect. 2.1.5) which, in unitary form, may be written here as

$$h(r) = \frac{1}{k_p} \int_0^\infty dk_\perp k_\perp \mathcal{E}_{\omega_p^o}(k_\perp/k_p) J_0(k_\perp r), \quad (82)$$

where $k_\perp = k_p \theta_p$ in a paraxial approximation, and r is the radial coordinate in the waist plane. It is notable that $h(r)$ represents the point spread function of the up-conversion system; i.e., multiplying the pump angular spectrum $\mathcal{F}(\theta_p, \phi_p | \omega_p^o)$ by the transfer function $\mathcal{E}_{\omega_p^o}(\theta_p)$ is equivalent to convolving the original transverse pump amplitude with $h(r)$ in the waist plane in the up-conversion crystal (Goodman (2005), Sect. 2.3.2). Figure 25 shows $h(r)$ for the same 3 cases of Fig. 24, with Eq. (82) being integrated numerically. The case for $\tilde{\theta}_c = 1.5^\circ$ exhibits a Gaussian-like distribution of width (e^{-1} radius) $12.5 \mu\text{m}$, with faint secondary rings. The case for $\tilde{\theta}_c = 4.0^\circ$ presents a distribution of width only $4.2 \mu\text{m}$, with secondary rings having higher contrast, while the case for $\tilde{\theta}_c = 2.3^\circ$ (width $7.7 \mu\text{m}$) shows intermediate behavior.

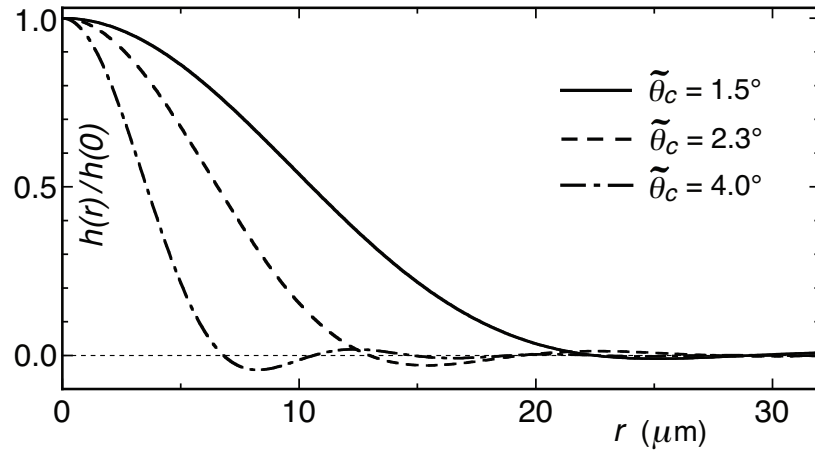


Figure 25. Normalized point-spread functions $h(r)$ as a function of radial coordinate, obtained from Fourier-Bessel transform of the results of Fig. 24.

5.1.2 Delayed recombination

We now provide ideal-case calculations for the time-delayed up-conversion rate from Eqs. 77-78, in which the signal photons are delayed by τ . These calculations are shown in Fig. 26 for the three cases of $\tilde{\theta}_c$ described in Section 5.1.1. It is seen that the curves are symmetric and have clear secondary maxima, accompanied by faint higher-order maxima. The widths (full width at half maximum) of the principal peaks at $\tau = 0$ are 33 fs for $\tilde{\theta}_c = 1.5^\circ$, 22 fs for $\tilde{\theta}_c = 2.3^\circ$, and 13 fs for $\tilde{\theta}_c = 4.0^\circ$. It is thus clear that the pairs must be quite closely synchronized in order to obtain recombination, and that the synchronization requirement becomes more strict as the limiting aperture is opened. This effect is a consequence of the form of Eq. 78 which, in the absence of frequency-dependent phase, is the Fourier transform of $S(\omega)$. As the system aperture size is increased, the bandwidth of $S(\omega)$ may be shown to increase in a nearly linear fashion, while the width of the curves of Fig. 26 decrease as the inverse of the bandwidth.

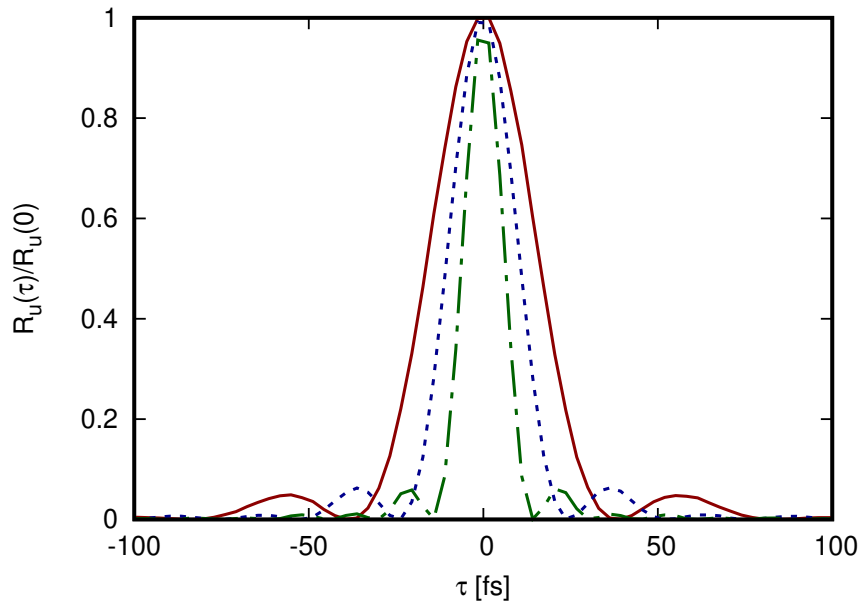


Figure 26. Normalized recombination rate as a function of time delay τ in the ideal case assuming 5 mm long lithium niobate crystals and an external cutoff angle $\tilde{\theta}_c$ of 1.5° (continuous red line), 2.3° (dashed blue line), and 4.0° (dot-dashed green line), with ΔT as specified in the text.

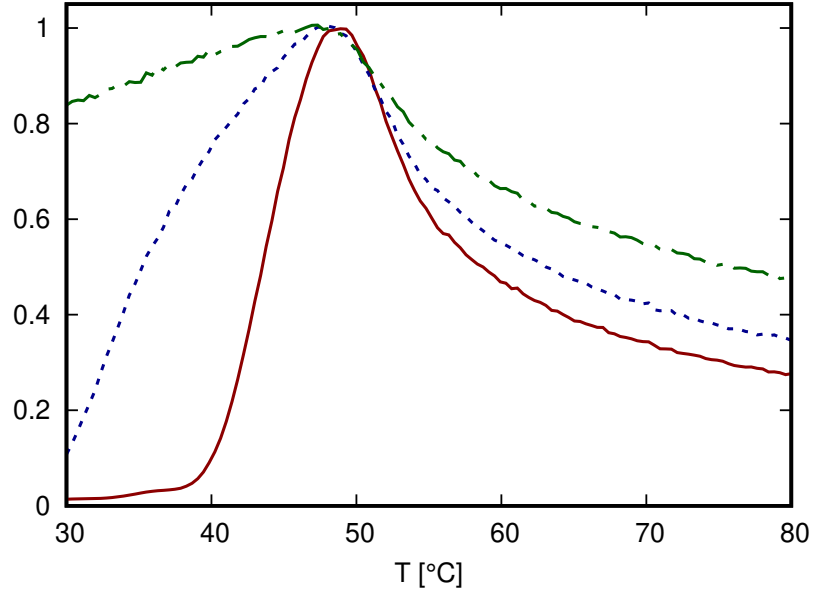


Figure 27. Normalized recombination rate as a function of the temperature of the down-conversion and up-conversion crystals T in the ideal case assuming 5 mm long lithium niobate crystals and an external cutoff angle $\tilde{\theta}_c$ of 1.5° (continuous red line), 2.3° (dashed blue line), and 4.0° (dot-dashed green line).

5.1.3 Recombination rate dependence on temperature and pump wavelength

In the narrowband and wide pump beam limit, Eq. 75 allows evaluation of the recombination rate as a function of any parameter of interest. One such parameter is the crystal temperature, for which results are shown in Fig. 27 for aperture radii $\tilde{\theta}_c = 1.5^\circ$, 2.3° , and 4.0° . For the case $\tilde{\theta}_c = 1.5^\circ$, the curve remains at low levels for small T . This occurs since for $T < 40^\circ$ there is quasi-phasematching to light only for angles greater than the aperture radius. As T is increased, the phasematched angles decrease and reach the aperture edge for $T \approx 40^\circ$ C as the curve of Fig. 27 rises rapidly while the degenerate ring of SPDC approaches the collinear condition. The curve reaches a maximum for T just under the axial degenerate phasematching temperature of 50° C. Phasematching of collinear degenerate down-conversion vanishes for $T > 50^\circ$, and the curve decays with temperature, with the non-degenerate emission now attaining the collinear phasematching condition. The cases for wider apertures shown in Fig. 27 exhibit analogous shapes but have broader features, as is reasonable for their larger angular integration effects which increases the number of modes through which the non-degenerate pairs may up-convert beyond the near-collinear contribution. Further, the peak of curves fall slightly farther to the left as $\tilde{\theta}_c$ increases. Another useful result may be obtained from Eq. 75 by holding crystal temperature at $T_o = 50^\circ$ C, and instead

considering the recombination rate as a function of pump wavelength. Such curves are shown in Fig. 28 for the same values of $\tilde{\theta}_c$ as in Fig. 28, where the shape roughly appears as the reverse of Fig. 28. The reasons for the shapes obtained are much as in Fig. 28; for λ_p somewhat greater than 532 nm, the phasematching occurs for large angles that can lie outside of the aperture domain, while $\lambda_p < 532$ nm, phase matching no longer occurs and the curve decays as phase mismatch increases. It is also seen that the peak of each curve lies slightly to the right of 532 nm.

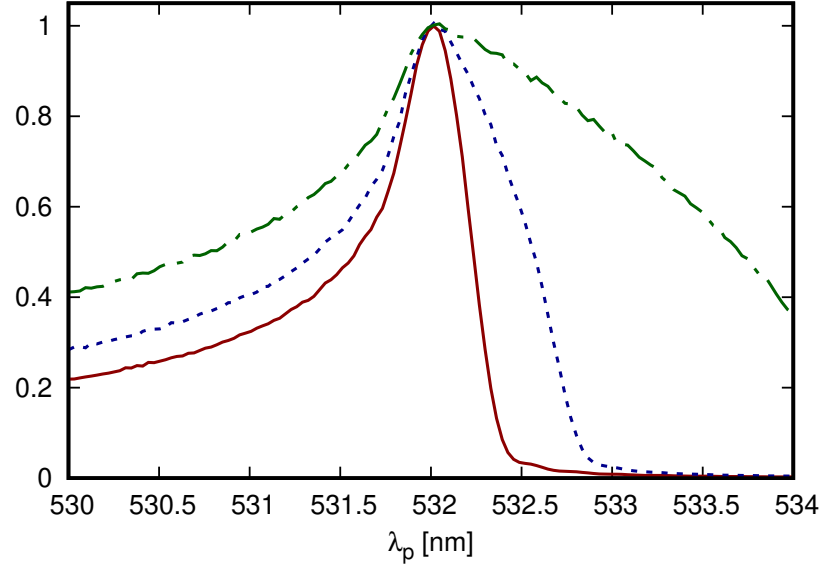


Figure 28. Normalized recombination rate as a function of the pump wavelength λ_p in the ideal case assuming 5 mm long lithium niobate crystals and an external cutoff angle $\tilde{\theta}_c$ of 1.5° (continuous red line), 2.3° (dashed blue line), and 4.0° (dot-dashed green line), with ΔT as specified in the text.

5.2 Realistic optical systems

We now consider numerical results for the case of a nonideal optical system producing frequency-dependent phase in the pair state. With experimental care, these effects are often reduced to a small but still clearly observable level. Including these effects will often lead to a good degree of agreement between theory and experiment, as will become apparent in the results that follow.

The modal phase $\varphi_\epsilon(\omega)$ is here taken as the series expansion about degenerate

frequency $\omega_d = \omega_p/2$ as

$$\varphi_\epsilon(\omega) = \sum_{n=2}^{\infty} \frac{\varphi_\epsilon^{(n)} \Delta\omega^n}{n!}, \quad (83)$$

where $\varphi_\epsilon^{(n)}$ denotes $\frac{\partial^n \varphi_\epsilon(\omega)}{\partial \omega^n} \Big|_{\omega_d}$, $\Delta\omega = \omega - \omega_d$, and the series begins in the second order so as to include only broadening effects; the second-order term represents group delay dispersion. In cases presented here, we take only the first three terms of Eq. 83, which provide an adequate approximation of $\varphi_\epsilon(\omega)$ over the SPDC bandwidth. Further, the total phase of the pair state has the form $\Phi(\Delta\omega) = \varphi_s(\omega_d + \Delta\omega) + \varphi_i(\omega_d - \Delta\omega)$, which has a series like that of Eq. (83), but with term coefficients $\Phi^{(n)}$ given by

$$\Phi^{(n)} = \varphi_s^{(n)} + (-1)^n \varphi_i^{(n)}. \quad (84)$$

To compare with experimental data, one must determine $\varphi_\epsilon(\omega)$ for the particular experimental system by computing the frequency-dependence of the phase accumulated along the optical path between the center of the first crystal and the center of the second crystal. This relies on the frequency-dependence of paths through prism compressors, and of the refractive indices of all media encountered. It may be computed by numerically tracing rays through the system to obtain $\varphi_\epsilon(\omega)$, and then obtaining the coefficients $\varphi_\epsilon^{(n)}$ of Eq. 83 numerically. Such a task is beyond the scope of this thesis, although these calculations have been performed elsewhere Jimenez *et al.* (2019) for the experimental comparisons to be made here.

5.2.1 Linear transfer functions

We now consider an experimental case described elsewhere O'Donnell (2011), with a sequence of four prisms providing dispersion compensation, with both signal and idler photons following this single path. It then follows that the signal and idler phases must be identical. In Ref. Jimenez *et al.* (2019) it was found that, with $\epsilon \in \{s, i\}$, $\varphi_\epsilon^{(2)} = 33.0 \text{ fs}^2$ and $\varphi_\epsilon^{(4)} = 2.54 \times 10^4 \text{ fs}^4$, with $\varphi_\epsilon^{(3)}$ being immaterial since the terms cancel in the total phase term $\Phi^{(3)}$ from Eq. 84. The transfer function $\mathcal{E}_{\omega_p^\circ}(\theta_p)$ of Eq. 74 is then computed using a Monte Carlo integration approach, producing the results for $\tilde{\theta}_c = 1.5^\circ$ and 2.3° shown in Fig. 29. It is seen that, unlike in Fig. 24, $\mathcal{E}_{\omega_p^\circ}(\theta_p)$ is now complex and has a small imaginary part. It is notable that temporal dispersion thus manifests itself

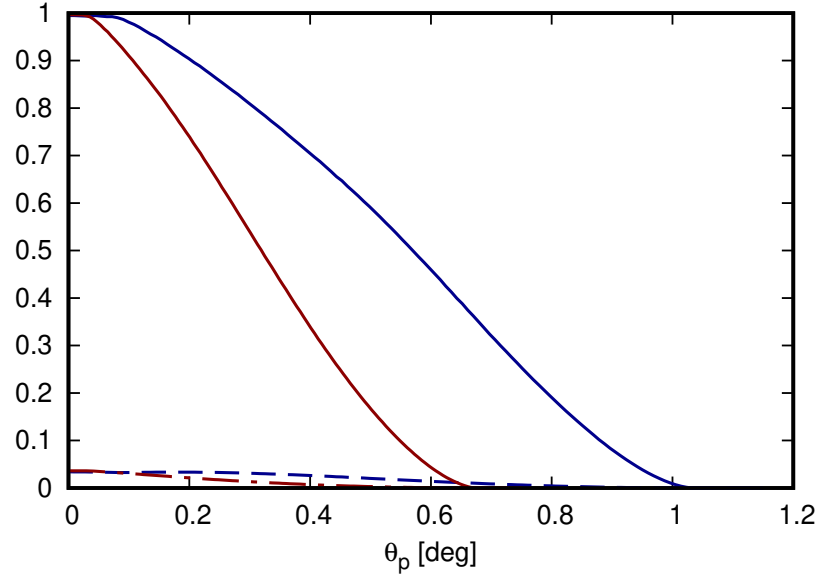


Figure 29. Real (continuous lines) and imaginary (dashed lines) parts of the angular transfer function calculated assuming 5 mm lithium niobate crystals with realistic dispersion parameters (for a single-path recombination experiment) and an external cutoff angle $\tilde{\theta}_c$ of 1.5° (red lines), and 2.3° (blue lines) with ΔT as specified in the text.

here as spatial phase in the up-converted state. Both cases have $|\mathcal{E}_{\omega_p^\circ}(\theta_p)|$ within 1% of the phase-free cases of Fig. 24, so that the effects of dispersion are fairly weak. The value of $\varphi_\epsilon^{(2)}$ can be readily adjusted in the experiments, and it here provides a good balancing of the quartic dispersion due to $\varphi_\epsilon^{(4)}$. Taking the Fourier-Bessel transform of $\mathcal{E}_{\omega_p^\circ}(\theta_p)$, we similarly find that $h(r)$ has a small imaginary part, although the width and modulus of $h(r)$ are within 1% of the analogous dispersion-free case from Fig. 25; thus we do not show this result here.

However, we emphasize that the dispersion compensation is essential in providing clear and observable signals, since stronger dispersive effects rapidly lead to much more attenuation, accompanied by changes to the shape of $\mathcal{E}_{\omega_p^\circ}(\theta_p)$. An example of a case having some attenuation may be obtained simply increasing $\tilde{\theta}_c$, even with the dispersion constants used in Fig. 29. The wider aperture increases the bandwidth in a proportional manner, and these same dispersion coefficients now produce stronger phase within the broader bandwidth. The case of $\tilde{\theta}_c = 4.0^\circ$ is shown in Fig. 30, where it is seen that $\mathcal{E}_{\omega_p^\circ}(\theta_p)$ now has a significant negative imaginary part, and that $|\mathcal{E}_{\omega_p^\circ}(0)|$ has fallen by 15% in comparison to the phase-free case. Figures 31-32 show the phase of $\mathcal{E}_{\omega_p^\circ}(\theta_p)$ for the cases of Figs. 29-30, where it is seen that this phase takes on a variety of shapes that are subtly related to the parameters of the calculations. For

$\tilde{\theta}_c = 1.5^\circ$ and 2.3° (Fig. 31), this phase is weak and is at most around 2° , while $\tilde{\theta}_c = 4^\circ$ (Fig. 32), the phase ranges from -14° to 2° .

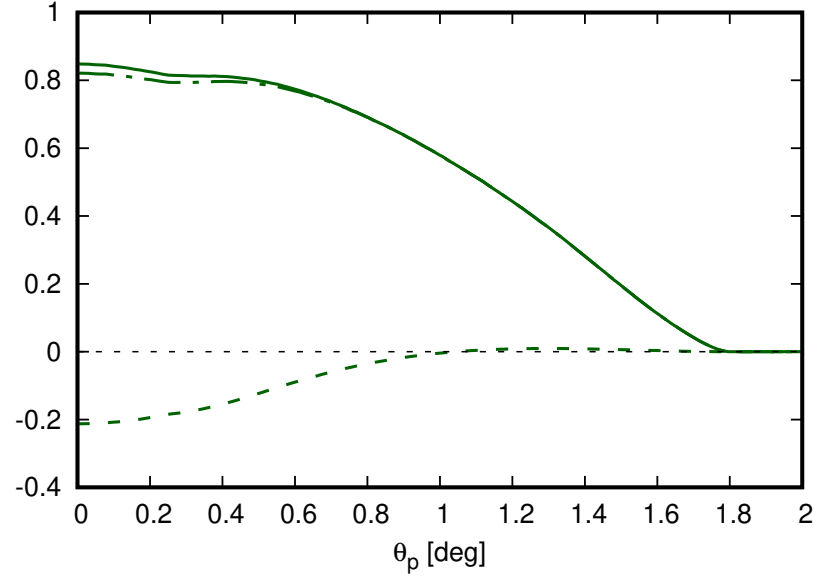


Figure 30. Real part (green dot-dashed line), imaginary part (green dashed line) and modulus (green solid curve) of the angular transfer function calculated assuming 5 mm lithium niobate crystals with realistic dispersion parameters (for a single-path compensated recombination experiment) and an external cutoff angle $\tilde{\theta}_c$ of 4.0° , with ΔT as specified in the text.

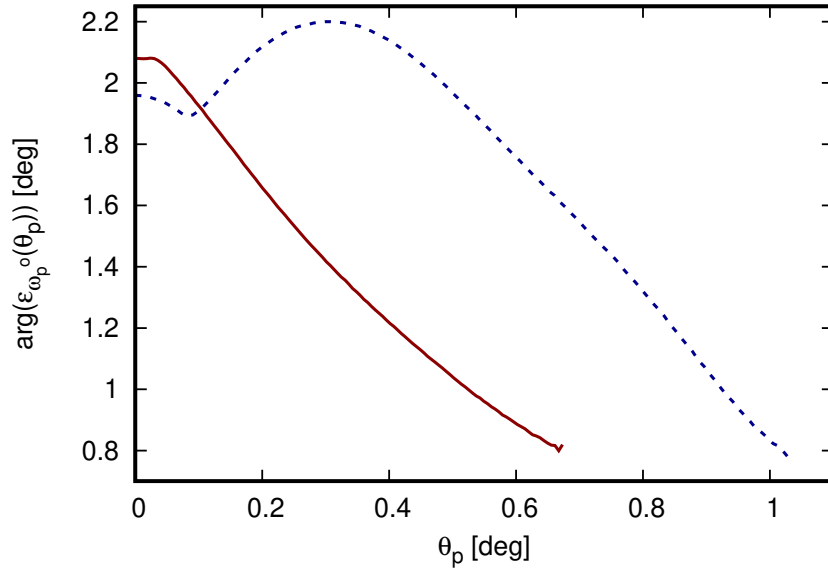


Figure 31. Phase of the angular transfer function calculated for the amplitudes of Fig. 29 with external cutoff angles of $\tilde{\theta}_c$ of 1.5° (continuous red line), and 2.3° (dashed blue line).

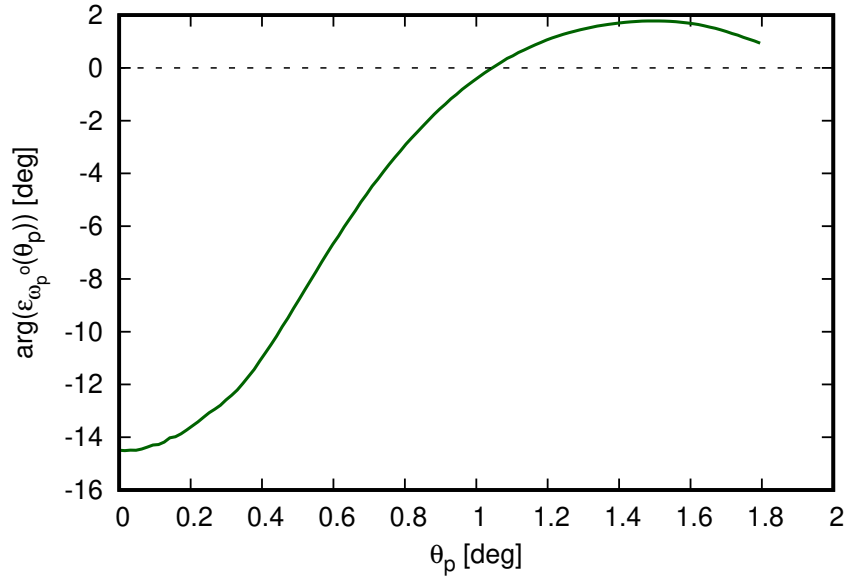


Figure 32. Phase of the angular transfer function calculated for the amplitude of Fig. 30 with external cutoff angle of $\hat{\theta}_c$ of 4.0° .

Depending on the width of the pump mode, it is thus clear that temporal dispersion of the pair state can affect the amplitude and phase of the reconstructed light, making it significantly different from the original pump mode.

5.2.2 Delayed recombination: comparison with experiments

Here we present comparison with a prior experimental work O'Donnell (2011) on Franson dispersion cancellation. The main point of this reference is that, since the pair state phase is the sum of the signal and idler phases, from Eq. 84 its series coefficient $\Phi^{(2)} = \varphi_s^{(2)} + \varphi_i^{(2)}$ obviously vanishes if $\varphi_s^{(2)} = -\varphi_i^{(2)}$. The effect is known as Franson dispersion cancellation. Since $\Phi^{(2)}$ often dominates the dispersive effects in practice, this cancellation effect is found to be quite clear in the observations of Ref. O'Donnell (2011). In particular, it is shown there that the time-delayed recombination rate has the same temporal width for a wide range of $\varphi_s^{(2)}$ and $\varphi_i^{(2)}$, as long as $\Phi^{(2)}$ is held constant at a small value. In addition, it is experimentally demonstrated that violating this Franson cancellation condition with large $|\Phi^{(2)}|$ greatly broadens the time-delayed recombination rate.

Thus, for the first time, we here provide comparisons of fully rigorous calculations

with these experimental results, both for dispersion cases having Franson cancellation, and for cases that do not. To achieve this, we need only apply the theory for the time-delayed up-conversion rate with dispersion parameters consistent with the experimental conditions. Before recombination, the signal and idler modes are separated and propagate through two different 4-prism compressors. The experiment changes the modal dispersion by varying the amount of insertion of the prisms in the compressors; more insertion increases modal propagation length within dispersive prism glass.

Estimates of the dispersion parameters are available from the ray-tracing methods described earlier Jimenez *et al.* (2019). The base modal dispersions are thus found to be

$$\vec{\varphi}_s = \{\varphi_s^{(2)}, \varphi_s^{(3)}, \varphi_s^{(4)}\} = \{31.4 \text{ fs}^2, -4430 \text{ fs}^3, -23800 \text{ fs}^4\} \quad (85)$$

and

$$\vec{\varphi}_i = \{\varphi_i^{(2)}, \varphi_i^{(3)}, \varphi_i^{(4)}\} = \{14.7 \text{ fs}^2, -3090 \text{ fs}^3, -16900 \text{ fs}^4\}, \quad (86)$$

which is the experimental case shown in Figs 2 or 3 of Ref. O'Donnell (2011) having minimal signal and idler dispersion. The other dispersion cases of Ref. O'Donnell (2011) are done by changing prism insertion so as to change prism glass path by multiples of 3.5 mm. Increasing glass path by 3.5 mm is found to change compressor dispersion by

$$\vec{\Delta} = \{\Delta^{(2)}, \Delta^{(3)}, \Delta^{(4)}\} = \{367 \text{ fs}^2, 363 \text{ fs}^3, -60 \text{ fs}^4\}. \quad (87)$$

To observe Franson cancellation, the experiment removes glass path from the signal mode while inserting equal glass path in the idler mode, in multiples of 3.5 mm. The dispersion parameters then follow as $\vec{\varphi}_s - n\vec{\Delta}$ and $\vec{\varphi}_i + n\vec{\Delta}$ with $n = 0, 1, 2$, and 3 for the four cases shown in Fig. 3 of Ref O'Donnell (2011). Of course, under such a procedure, Eq. 84 implies that $\Phi^{(2)}$ remains fixed at a nominal value (46.1 fs^2) which allows Franson cancellation to be observed, although $\Phi^{(3)}$ and $\Phi^{(4)}$ change slightly in the four cases.

Figure 33 shows these four cases, all of which present a constant width of 22 fs and thus clearly demonstrate Franson dispersion cancellation. As n increases, however, the resulting cubic dispersion parameter $\Phi^{(3)}$ becomes more negative; this series of results consequently exhibit increasing right-skewness and increasing shift from the

origin, and also have slightly decreasing height. These are modest but clear effects, and the constant temporal width, the increasing right-skewness, and the decrease in height are all consistent with the experimental data in Fig. 3 of Ref. O'Donnell (2011).

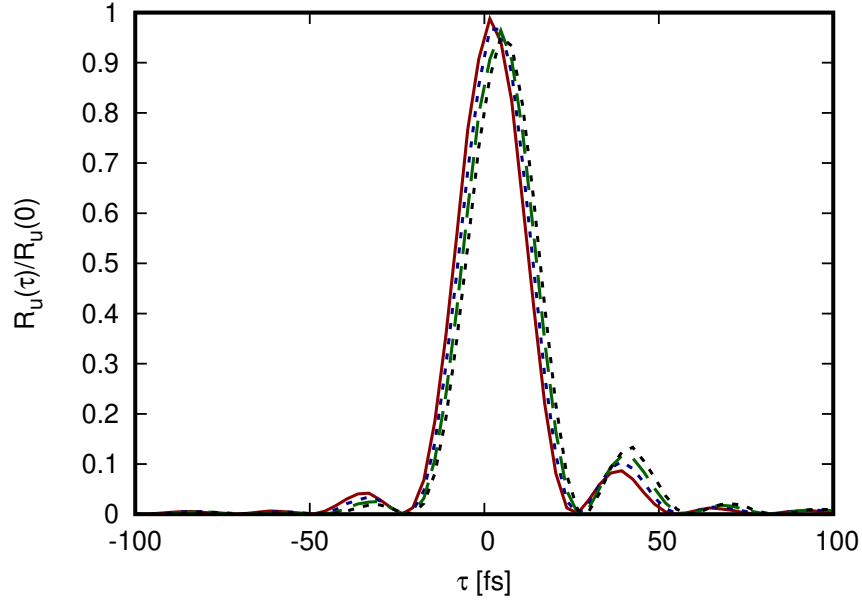


Figure 33. Normalized recombination rate as a function of time delay τ with realistic dispersion parameters of four-prism compensated, two-path configurations assuming 5 mm long lithium niobate crystals and an external cutoff angle $\tilde{\theta}_c$ of 2.3° . The curves are calculated in conditions comparable to the experimental results of Fig. 3 of Ref. O'Donnell (2011), with excess signal/idler second-order dispersions at $\{0, 0\}$ shown in red (continuous), $\{-\Delta, \Delta\}$ in blue (dashed), $\{-2\Delta, 2\Delta\}$ in green (long-dashed), and $\{3\Delta, 3\Delta\}$ in black (dashed), where $\Delta = 367 \text{ fs}^2$. Curves are normalized with respect to the height of the undispersed case.

Figure 34 shows the phase of the up-converted amplitude of the four cases of Fig. 33, which are of interest but are not available in the existing experimental data.

It is seen there that the phase is near zero throughout the central lobe of the distribution of Fig. 33, and that the secondary lobes are nearly 180° out of phase. The four cases show some mild variation in phase for the four dispersion cases. In Fig. 35 another result shows the time-delayed recombination rate for the $n = 0$ dispersion case, but with the limiting aperture opened to $\tilde{\theta}_c = 4.0^\circ$. The larger aperture increases the bandwidth, with the consequence that the cubic term plays a far more important role. It is seen that the curve is strongly right-skewed, and that its height has decreased significantly from the dispersion-free case. Still, the temporal width is quite narrow (16 fs) and is only slightly wider than the corresponding dispersion-free case of Fig. 26 (13 fs). There is no experimental data available for $\tilde{\theta}_c = 4.0^\circ$ due to aperture limitations in Ref. O'Donnell (2011), although future experiments could thus conceivably provide

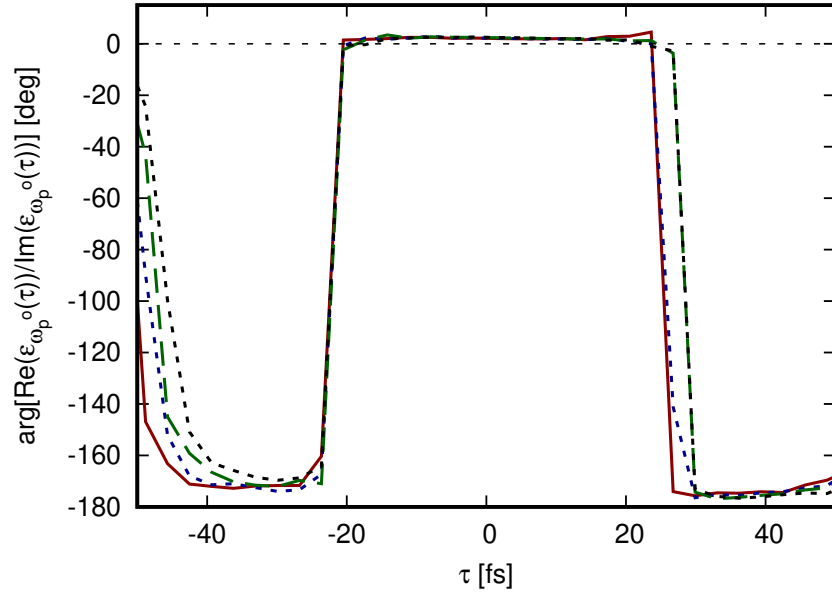


Figure 34. Phase of the delayed transfer efficiency as a function of the time delay τ corresponding to the cases shown in Fig 33.

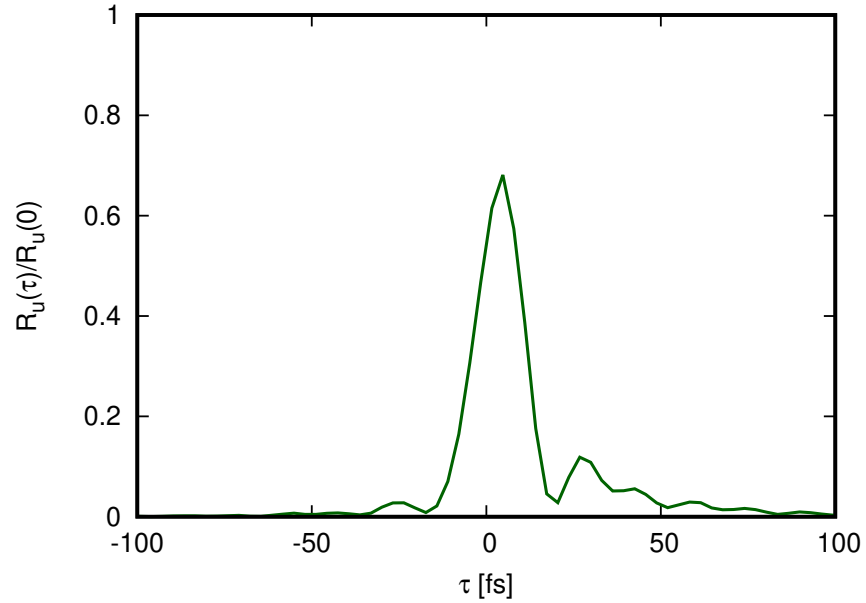


Figure 35. Normalized recombination rate as a function of the time delay τ with dispersion parameters as in Fig. 3(a) in Ref. O'Donnell (2011) and an external cutoff angle $\tilde{\theta}_c$ of 4.0° . Normalization is to unit height in the phase-free case.

significantly narrower temporal widths. Further, Fig. 36 shows the phase of the amplitude associated with Fig. 35. It is seen that the curve bears little resemblance to the essentially constant-phase regions that were present in Fig. 34, and that the curve continuously drifts apart from the phase jumps associated with the principal value range that is plotted. This unusual form of the phase is largely due to $\Phi^{(3)}$, although $\Phi^{(2)}$ and $\Phi^{(4)}$ also play lesser roles here.

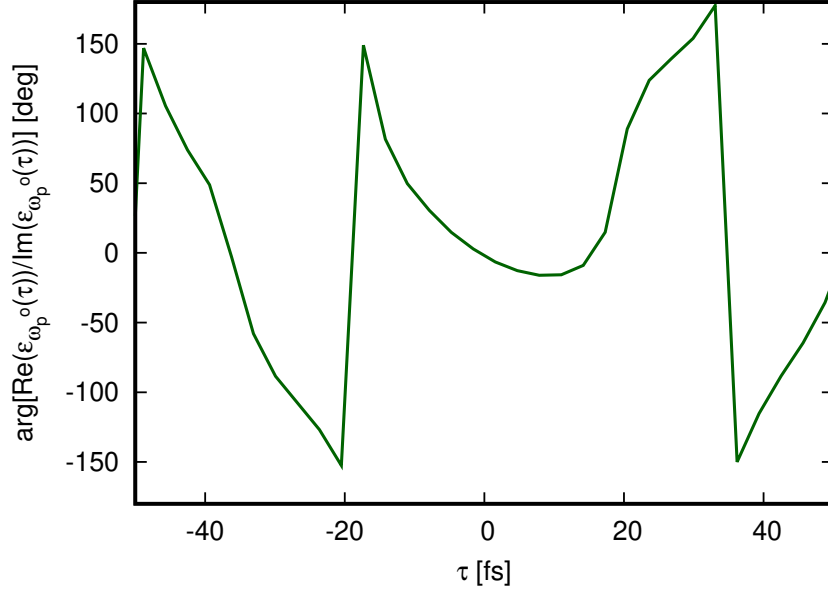


Figure 36. Phase of the delayed transfer efficiency as a function of the time delay τ corresponding to the case shown in Fig 35.

We now consider cases without Franson cancellation, for which large $|\Phi^{(2)}|$ produce broadening effects that have been experimentally observed in Ref. O'Donnell (2011). Numerical results for such cases are shown in Fig. 37 with dispersion parameters $\bar{\varphi}_s - n\bar{\Delta}$ and $\bar{\varphi}_i$, and in Fig. 38 with dispersion parameters $\bar{\varphi}_s$ and $\bar{\varphi}_i + n\bar{\Delta}$, which correspond to, respectively, removing glass path from only the signal mode, or adding glass path to only the idler mode. Such a procedure will introduce strong effects in the resulting cases, which have highly nonzero $\Phi^{(2)}$ in the pair state. The cases for $n = 1$ in Figs. 37-38 are significantly reduced to just under half the height of the undispersed case, with cases for $n = 2$ and 3 becoming increasingly broader and lower. The three cases shown appear almost identical when comparing Figs. 37 and 38. This is a consequence of $\Phi^{(2)}$ dominating the appearance of the curves, although close examination reveals that the figures have small differences. However, this is to be somewhat contrasted with the experiments of Ref. O'Donnell (2011), for

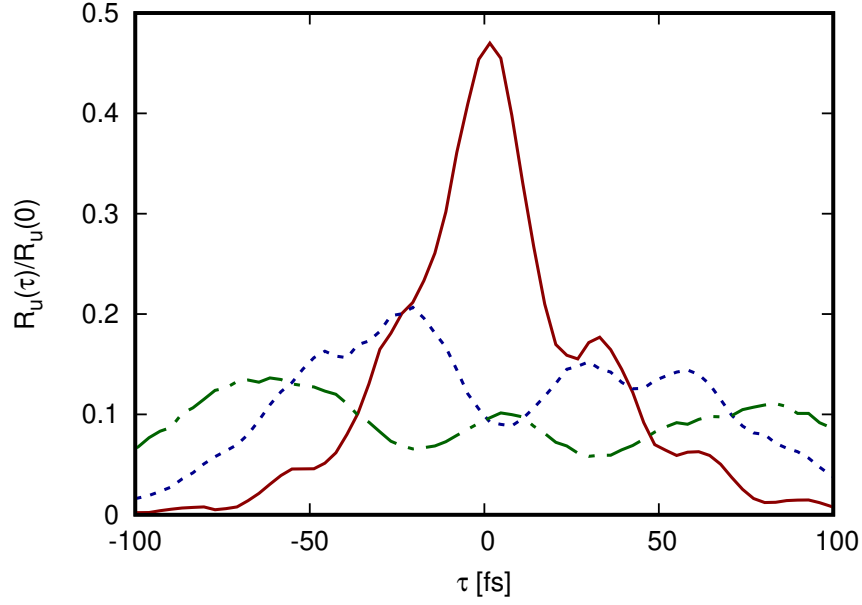


Figure 37. Normalized recombination rate as a function of the time delay τ with realistic dispersion parameters of three non-compensated, two-path configurations assuming 5 mm lithium niobate crystals and an external cutoff angle of $\tilde{\theta}_c$ of 2.3° . The curves are calculated in conditions comparable to the experimental results of Fig. 2(b-d) in Ref. O'Donnell (2011), with $\{-\Delta, 0\}$ shown in red (continuous), $\{-2\Delta, 0\}$ in blue (dashed), and $\{-3\Delta, 0\}$ in green (dot-dashed), where $\Delta = 367 \text{ fs}^2$. Normalization is to unit height in the phase-free case.

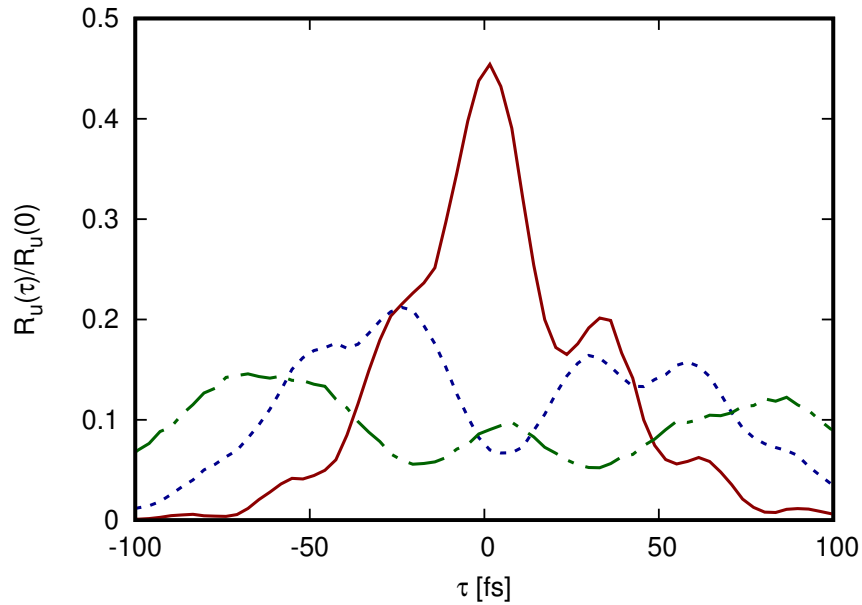


Figure 38. Normalized recombination rate as a function of the time delay τ with realistic dispersion parameters of three non-compensated, two-path configurations assuming 5 mm lithium niobate crystals and an external cutoff angle of $\tilde{\theta}_c$ of 2.3° . The curves are calculated in conditions comparable to the experimental results of Fig. 2(e-g) in Ref. O'Donnell (2011), with $\{0, \Delta\}$ shown in red (continuous), $\{0, 2\Delta\}$ in blue (dashed), and $\{0, 3\Delta\}$ in green (dot-dashed), where $\Delta = 367 \text{ fs}^2$. Normalization is to unit height in the phase-free case.

which the analogous plots (see its Fig. 2) show more significant differences comparing similar cases having positive and negative $\Phi^{(2)}$. The probable conclusion is that the experimental data have contributions from effects not included in the theory as it is evaluated here. One possibility is that other frequency-dependent phase effects are occurring over the wide experimental bandwidth; for example, the SPDC collimating lenses employed are plano-convex singlets that would have some variation in focal length due to the frequency-dependent refractive index of their glass. While the general formulation developed in this thesis is capable of fully accounting for such effects, their numerical evaluation is beyond the scope of the comparisons presented in this chapter.

In summary, the results presented here show that recombination of entangled photon pairs can, under suitably prepared conditions, reproduce all features of pump beam in the up-converted field coherently. The interference between the attenuated pump and up-converted amplitude at the single-photon level, then, can be used to study the amplitude and phase of the two-photon state, for example by selectively allowing only a certain portion of the two-photon field to couple into the recombination crystal. Should the important and difficult task of dispersion compensation be surmounted for adequately broad bandwidths, the recombination of photon pairs through the mechanisms described here should be possible near the single-cycle biphoton condition with a correspondingly higher efficiency. Additionally, preselection of the wave-vector domain of the photon pairs which are allowed to recombine allows other up-converted fields to be similarly prepared; for example, allowing only the portion of the down-conversion that produces the bimodal coherence cell in Fig. 18 would produce an up-converted state that closely resembles a first order Hermite Gaussian beam.

Chapter 6. Conclusions

We have presented a theoretical and experimental study of the generation and recombination of time-frequency entangled photon pairs. This work is intended to provide a foundation over which more elaborate experiments may be designed and performed, while establishing a means to compare with rigorous theoretical calculations. It is our expectation that, by addressing these foundational topics, other researchers in the field will be enabled to advance further in both the theory and the experiments with a clearer understanding on the correspondence between the two.

Despite the apparent success of the simplified theoretical methods that are often employed in the study and teaching of quantum optics, it is expected that, as the field continues to progress, the more elaborate theoretical methods such as provided here will prove valuable. Our theoretical results concerning the two-photon amplitude produced in SPDC and the up-converted amplitude produced by photon pair recombination have been employed to produce calculations that accurately represent our experimental conditions in the case of SPDC as well as previously published work in the case of recombination. In particular, we believe the metrological applications of this work can be significant and may be used to verify the correspondence between the nonlinear susceptibilities used in classical non-linear optics and that which is present in the interaction Hamiltonian within our quantum optical theory.

Two research papers were published as a result of the development of this project:

- *Angular and temperature dependence of photon pair rates in spontaneous parametric down-conversion from a periodically poled crystal*, Physical Review A, 96, 023828 (2017). G. Daniel Jimenez, Veneranda G. Garces, and Kevin A. O'Donnell.
- *Coherent reconstruction of pump beams through recombination of entangled photon pairs*, Physical Review A, 99, 023853 (2019). G. Daniel Jimenez, Veneranda G. Garces, and Kevin A. O'Donnell.

Additionally, the following presentations were made:

- *How to time a photon*. Poster presented at CICESE's regional congress of optics (CReO, 2016). G. Daniel Jimenez, Veneranda G. Garces, and Kevin A. O'Donnell.

- *Single-Photon Detectors: Their Characterization and Use with Entangled Photon Pairs*. Poster presented at the mexican national congress of physics (2018). Trabajo M1G016. G. Daniel Jimenez, Veneranda G. Garces, and Kevin A. O'Donnell.
- *A simple model of a one dimensional, randomly rough, non-Gaussian Surface*, Proc. SPIE 9961, Reflection, Scattering, and Diffraction from Surfaces V, 99610D (September 26, 2016). E. R. Méndez, G. D. Jiménez, A. A. Maradudin.

Bibliography

- Blow, K., Loudon, R., Phoenix, S. J., and Shepherd, T. (1990). Continuum fields in quantum optics. *Physical Review A*, **42**(7): 4102.
- Burlakov, A., Chekhova, M., Klyshko, D., Kulik, S., Penin, A., Shih, Y., and Strekalov, D. (1997). Interference effects in spontaneous two-photon parametric scattering from two macroscopic regions. *Physical Review A*, **56**(4): 3214.
- Burnham, D. C. and Weinberg, D. L. (1970). Observation of simultaneity in parametric production of optical photon pairs. *Physical Review Letters*, **25**(2): 84.
- Byer, R. and Harris, S. (1968). Power and bandwidth of spontaneous parametric emission. *Physical Review*, **168**(3): 1064.
- da Costa Moura, A., Nogueira, W., and Monken, C. (2010). Fourth-order image formation by spontaneous parametric down-conversion: The effect of anisotropy. *Optics Communications*, **283**(14): 2866 – 2871.
- Dayan, B., Peer, A., Friesem, A. A., and Silberberg, Y. (2005). Nonlinear interactions with an ultrahigh flux of broadband entangled photons. *Physical review letters*, **94**(4): 043602.
- Dield, J. and Rudolph, W. (2006). *Ultrashort laser pulse phenomena*. Elsevier.
- Emanuelli, S. and Arie, A. (2003). Temperature-dependent dispersion equations for KTiOPO₄ and KTiOAsO₄. *Applied optics*, **42**(33): 6661–6665.
- Ghosh, R. and Mandel, L. (1987). Observation of nonclassical effects in the interference of two photons. *Physical Review Letters*, **59**(17): 1903.
- Glauber, R. J. (1963a). Coherent and incoherent states of the radiation field. *Physical Review*, **131**(6): 2766.
- Glauber, R. J. (1963b). The quantum theory of optical coherence. *Physical Review*, **130**(6): 2529.
- Goodman, J. (2005). *Introduction to Fourier Optics*. McGraw-Hill physical and quantum electronics series. W. H. Freeman.
- Grayson, T. P. and Barbosa, G. A. (1994). Spatial properties of spontaneous parametric down-conversion and their effect on induced coherence without induced emission. *Phys. Rev. A*, **49**: 2948–2961.
- Gunther, Aimee Kirsten (2018). PPLN-based photon pair sources toward biphoton quantum frequency conversion.
- Hamar, M., Peřina Jr, J., Haderka, O., and Michálek, V. (2010). Transverse coherence of photon pairs generated in spontaneous parametric down-conversion. *Physical Review A*, **81**(4): 043827.
- Harris, S., Oshman, M., and Byer, R. (1967). Observation of tunable optical parametric fluorescence. *Physical Review Letters*, **18**(18): 732.
- Harris, S. E. and Sensarn, S. (2007). Toward single-cycle biphotons. In: *Conference on Coherence and Quantum Optics*. Optical Society of America, page CMD1.

- Helt, L. G. and Steel, M. J. (2015). Effect of scattering loss on connections between classical and quantum processes in second-order nonlinear waveguides. *Opt. Lett.*, **40**(7): 1460–1463.
- Helt, L. G., Steel, M. J., and Sipe, J. E. (2015). Spontaneous parametric downconversion in waveguides: what's loss got to do with it? *New Journal of Physics*, **17**(1): 013055.
- Holstein, B. R. and Ashkin, J. (1992). Topics in advanced quantum mechanics. addison-wesley.
- Hong, C. and Mandel, L. (1985). Theory of parametric frequency down conversion of light. *Physical Review A*, **31**(4): 2409.
- Hong, C.-K., Ou, Z.-Y., and Mandel, L. (1987). Measurement of subpicosecond time intervals between two photons by interference. *Physical review letters*, **59**(18): 2044.
- Huttner, B. and Barnett, S. M. (1992). Quantization of the electromagnetic field in dielectrics. *Physical Review A*, **46**(7): 4306.
- Jimenez, G. D., Garces, V. G., and O'Donnell, K. A. (2017). Angular and temperature dependence of photon pair rates in spontaneous parametric down-conversion from a periodically poled crystal. *Physical Review A*, **96**(2): 023828.
- Jimenez, G. D., Garces, V. G., and O'Donnell, K. A. (2019). Coherent reconstruction of pump beams through recombination of entangled photon pairs. *Physical Review A*, **99**(2): 023853.
- Jiménez, G. D. (2014). Fundamentals and applications in the detection of coincident entangled photon pairs. centro de investigación científica y de educación superior de ensenada, baja california. masters thesis.
- Joobeur, A., Saleh, B. E., and Teich, M. C. (1994). Spatiotemporal coherence properties of entangled light beams generated by parametric down-conversion. *Physical Review A*, **50**(4): 3349.
- Joobeur, A., Saleh, B. E., Larchuk, T. S., and Teich, M. C. (1996). Coherence properties of entangled light beams generated by parametric down-conversion: Theory and experiment. *Physical Review A*, **53**(6): 4360.
- Jundt, D. H. (1997). Temperature-dependent sellmeier equation for the index of refraction, n_e , in congruent lithium niobate. *Opt. Lett.*, **22**(20): 1553–1555.
- Klyshko, D. N. (1988). *Photons and nonlinear optics*. OPA (Amsterdam).
- Louisell, W., Yariv, A., and Siegman, A. (1961). Quantum fluctuations and noise in parametric processes. i. *Physical Review*, **124**(6): 1646.
- Lukens, J. M., Dezfooliyan, A., Langrock, C., Fejer, M. M., Leaird, D. E., and Weiner, A. M. (2013). Demonstration of high-order dispersion cancellation with an ultrahigh-efficiency sum-frequency correlator. *Physical review letters*, **111**(19): 193603.
- Lukens, J. M., Dezfooliyan, A., Langrock, C., Fejer, M. M., Leaird, D. E., and Weiner, A. M. (2014). Orthogonal spectral coding of entangled photons. *Physical review letters*, **112**(13): 133602.
- Luks, A. and Perinová, V. (2009). *Quantum aspects of light propagation*. Springer.

- Malygin, A., Penin, A., and Sergienko, A. (1985). Spatiotemporal grouping of photons in spontaneous parametric scattering of light. *Sov. Phys. Dokl*, **30**: 227–229.
- Mandel, L. and Wolf, E. (1995). *Optical coherence and quantum optics*. Cambridge university press.
- Molina-Terriza, G., Minardi, S., Deyanova, Y., Osorio, C. I., Hendrych, M., and Torres, J. P. (2005). Control of the shape of the spatial mode function of photons generated in noncollinear spontaneous parametric down-conversion. *Phys. Rev. A*, **72**: 065802.
- Monken, C. H., Ribeiro, P. H. S., and Pádua, S. (1998). Transfer of angular spectrum and image formation in spontaneous parametric down-conversion. *Phys. Rev. A*, **57**: 3123–3126.
- Odele, O. D., Lukens, J. M., Jaramillo-Villegas, J. A., Langrock, C., Fejer, M. M., Leaird, D. E., and Weiner, A. M. (2015). Tunable delay control of entangled photons based on dispersion cancellation. *Optics express*, **23**(17): 21857–21866.
- O'Donnell, K. A. (2011). Observations of dispersion cancellation of entangled photon pairs. *Physical review letters*, **106**(6): 063601.
- O'Donnell, K. A. and Garces, V. G. (2015). Interference in the recombination of frequency-entangled photon pairs. *Journal of Modern Optics*, **62**(19): 1616–1622.
- O'Donnell, K. A. and U'Ren, A. B. (2009). Time-resolved up-conversion of entangled photon pairs. *Physical review letters*, **103**(12): 123602.
- Ou, Z., Wang, L., and Mandel, L. (1989). Vacuum effects on interference in two-photon down conversion. *Physical Review A*, **40**(3): 1428.
- Ou, Z., Zou, X., Wang, L., and Mandel, L. (1990). Observation of nonlocal interference in separated photon channels. *Physical review letters*, **65**(3): 321.
- Peer, A., Dayan, B., Friesem, A. A., and Silberberg, Y. (2005). Temporal shaping of entangled photons. *Physical review letters*, **94**(7): 073601.
- Rubin, M. H., Klyshko, D. N., Shih, Y., and Sergienko, A. (1994). Theory of two-photon entanglement in type-ii optical parametric down-conversion. *Physical Review A*, **50**(6): 5122.
- Shen, H. Y., Xu, H., Zeng, Z. D., Lin, W. X., Wu, R. F., and Xu, G. F. (1992). Measurement of refractive indices and thermal refractive-index coefficients of linbo3 crystal doped with 5 mol. % mgo. *Appl. Opt.*, **31**(31): 6695–6697.
- Shih, Y. (2016). *An introduction to quantum optics: Photon and biphoton physics*. pages 1–448.
- Shoji, I., Kondo, T., Kitamoto, A., Shirane, M., and Ito, R. (1997). Absolute scale of second-order nonlinear-optical coefficients. *JOSA B*, **14**(9): 2268–2294.
- Strekalov, D., Sergienko, A., Klyshko, D., and Shih, Y. (1995). Observation of two-photon “ghost” interference and diffraction. *Physical review letters*, **74**(18): 3600.
- U'Ren, A. B., Banaszek, K., and Walmsley, I. A. (2003). Photon engineering for quantum information processing. *quantum information and computation* 3, 480 (2003).

- Walborn, S. P., de Oliveira, A. N., Thebaldi, R. S., and Monken, C. H. (2004). Entanglement and conservation of orbital angular momentum in spontaneous parametric down-conversion. *Phys. Rev. A*, **69**: 023811.
- Wang, L., Zou, X., and Mandel, L. (1991). Induced coherence without induced emission. *Physical Review A*, **44**(7): 4614.
- Zel'Dovich, B. Y. and Klyshko, D. (1969). Field statistics in parametric luminescence. *ZhETF Pisma Redaktsiiu*, **9**: 69.
- Zou, X., Wang, L. J., and Mandel, L. (1991). Induced coherence and indistinguishability in optical interference. *Physical review letters*, **67**(3): 318.

Appendix: Invariance of the down-converted rates under exchange of the signal and idler variables

The photon pair rate R_π and signal photon rate R_s from Eqs. 38 and 39, respectively, can be used to produce a set of *dual* expressions which are identical in form, but for which the signal and idler variables are exactly interchanged. This is a necessary condition for a correct theoretical description of the photon pair generation process, and responds to the natural symmetry that exists between the signal and idler portions of the down-converted state. We start from the pair rate of Eq. 38, and consider for simplicity the case of a circular aperture

$$R_\pi = \beta R_p \frac{\hbar \omega_p^0}{n_p} \int d\omega_s T_s(\omega_s) T_i(\omega_i) S_\pi(\omega_s) \quad (88)$$

where we have dropped the assumption of non-overlapping wave-vector domains, which causes the factor of two to no longer appear in the coefficients on the right-hand side, and

$$S(\omega_s) = \omega_s^3 \omega_i \int_0^{\Theta_s} d\theta_s \int_0^{2\pi} d\phi_s \frac{n_s \sin \theta_s}{n_i \cos \theta_i} |s(\Delta k_z)|^2 D_i(\theta_i) \quad (89)$$

where $\sin \Theta_s = \sin \tilde{\theta}_c / n_s$ is the (temperature and frequency dependent) angular limit within the crystal, and the limits of the ϕ_s integration are consistent with the assumption that $\mathcal{D}_s = \mathcal{D}_i$. The ϕ_s integration is trivial since the integrand is circularly symmetric; the case of an arbitrary aperture may be demonstrated using similar methods similarly, but requires a more careful treatment using the general two-variable discrimination function $D(\theta_i, \phi_i)$ and will not be considered here. It is clear that Eq. 88 is invariant with respect to signal-idler variable exchange if and only if Eq. 89 is invariant as well.

Thus, we use the QPM conditions, which are derived from Eqs. 22 and 23 and in the axial wide pump limit read

$$\sin \theta_s = \frac{n_i \omega_i}{n_s \omega_s} \sin \theta_i \quad (90)$$

$$\phi_i = \phi_s - \pi \quad (91)$$

from which we can derive the differential relationship $d\phi_s = d\phi_i$ and, through implicit

differentiation,

$$\frac{d\theta_s}{d\theta_i} = \frac{n_i \omega_i \cos \theta_i}{n_s \omega_s \cos \theta_s}. \quad (92)$$

These two expressions may then be used to exchange the θ_s and ϕ_s integration variables for θ_i and ϕ_i , yielding

$$S(\omega_s) = \omega_s^2 \omega_i^2 \int_0^{\Theta_i} d\theta_i \int_{-\pi}^{\pi} d\phi_i \frac{\sin \theta_s}{\cos \theta_s} |s(\Delta k_z)|^2 D_i(\theta_i) \quad (93)$$

where $\sin \Theta_i = \frac{n_s \omega_s}{n_i \omega_i} \sin \Theta_s$. We may then use Eq. 90 to substitute the $\sin \theta_s$ term in the integrand of Eq. 93 to produce

$$S(\omega_s) = \omega_i^3 \omega_s \int_0^{\Theta_i} d\theta_i \int_0^{2\pi} d\phi_i \frac{n_i \sin \theta_i}{n_s \cos \theta_s} |s(\Delta k_z)|^2 D_i(\theta_i) \quad (94)$$

where we have changed the integration domain of the ϕ_i angle to cover the positive angles without affecting the integral. Equation 94 has nearly the desired form and now requires consideration of the $D_i(\theta_i)$ discriminator function. We have that $D_i(\theta_i) = 1$ if $\theta_i \leq \Theta_i$, and is zero in any other case; within the monotonic domain of the sine function, this implies that $\sin \theta_i \leq \sin \Theta_i = \frac{\omega_s \sin \tilde{\theta}_c}{n_i \omega_i}$, so that the condition $\sin \theta_s \leq \sin \theta_c / n_s = \sin \Theta_s$ holds when $D_i(\theta_i) = 1$, and we can write

$$S(\omega_s) = \omega_i^3 \omega_s \int_0^{\Theta_i} d\theta_i \int_0^{2\pi} d\phi_i \frac{n_i \sin \theta_i}{n_s \cos \theta_s} |s(\Delta k_z)|^2 D_s(\theta_s) \quad (95)$$

where $D_s(\theta_s) = 1$ if $\theta_s \leq \Theta_s$ and zero in any other case, and we can finally determine that $S(\omega_s) = S(\omega_i)$, with $\omega_i + \omega_s = \omega_p$. This concludes the proof.

We note that the signal-idler symmetry here demonstrated in the down-converted rates also appears the up-conversion rate, as it is described by the same down-conversion spectrum $S(\omega_s)$ (cf. Eq. 74). While we have assume in this appendix to consider overlapping signal-idler domains, the only consequences of this choice in the case here considered are the limits of the ϕ_s and ϕ_i integrations in $S(\omega_s)$ and $S(\omega_i)$, which are taken along the complete 2π range of the circular aperture, and the presence or absence of the factor of 2 in the expression for the rate, and thus the conclusions are valid under both assumptions. Additionally, it is possible to exploit this result by separating Eq. 88 as two integrations from 0 to $\omega_d \equiv \omega_p/2$, and another from ω_d to ω_p ,

which are trivially shown to be identical, which allows us to write

$$R_{\pi} = 2\beta R_p \frac{\hbar\omega_p^o}{n_p} \int_0^{\omega_d} d\omega_s T_s(\omega_s) T_i(\omega_i) S(\omega_s) \quad (96)$$

which is useful in computations as the integration only has to be performed over only one half of the total bandwidth of the photon pairs and it avoids evaluation of the discrimination function $D_i(\theta_i)$, for it is simple to prove that $\omega_s \leq \omega_d$ is a sufficient condition for $\theta_s \geq \theta_i$, and there are no rejected idler photons to account for in this case.